Copyright
by
Richard David Lenhart
2014

The Thesis Committee for Richard David Lenhart
certifies that this is the approved version of the following thesis:

Development of a Standing-Wave Apparatus for Calibrating Acoustic Vector Sensors

APPROVED BY

SUPERVISING COMMITTEE:

Preston S. Wilson, Co-Supervisor

Jason D. Sagers, Co-Supervisor

Development of a Standing-Wave Apparatus for Calibrating Acoustic Vector Sensors

by

Richard David Lenhart, B.S.M.E.

THESIS

Presented to the Faculty of the Graduate School of

The University of Texas at Austin

in Partial Fulfillment

of the Requirements

for the Degree of

MASTER OF SCIENCE IN ENGINEERING

The University of Texas at Austin

August 2014

To Jessica.

Acknowledgments

I would like to begin by thanking my co-supervisors, Preston Wilson and Jason Sagers. Preston, I am grateful for your guidance throughout my time in graduate school and with this project and am indebted to your support prior to starting graduate school. Jason, I cannot thank you enough for the countless hours you have spent guiding me throughout my research. Your mentorship has been instrumental to the success of this project and your friendship has been invaluable to me.

Also deserving thanks are Bini Rajan, Tom Wise, Geno Gargas, and the entire ESL engineering team for the many hours of support throughout the development of the standing-wave apparatus. Your expertise in each of your fields has aided significantly. Additionally, I would like to thank Gary Wilson and Marti Barlett for providing me with the opportunity to build the apparatus.

Significant appreciation is due to Clark Penrod, Rich Gramann, Karl Fisher, and Mike Pestorius for providing financial support for this project through the Applied Research Laboratories Internal Research and Development program.

Lastly, I would like to thank Jessica Kirma for her devoted support throughout my time in graduate school and with this project. You have been there for me through thick and thin, every step of the way and for this I am eternally grateful.

Development of a Standing-Wave Apparatus for Calibrating Acoustic Vector Sensors

Richard David Lenhart, M.S.E.
The University of Texas at Austin, 2014

Supervisors: Preston S. Wilson
Jason D. Sagers

Underwater acoustic pressure transducers measure pressure fluctuations, a scalar parameter of the acoustic field. Acoustic vector sensors contain an omni-directional pressure transducer (omni) and also bi- or tri-axial sensing elements that respond to either the particle velocity or pressure gradient of the acoustic field; which are vector quantities. The amplitude of the signal output of each directional channel of a vector sensor is proportional to the orientation relative to the direction of acoustic pressure propagation. The ratio of the signal amplitudes between two directional channels and the cross-spectra between the vector sensor omni and directional channels enable one to estimate the bearing to the source from a single point measurement. In order to accurately estimate the bearing across the usable frequency band of the vector sensor, the complex sensitivities of the omni and directional channels must be known. Since there is no standard directional reference transducer for a comparative calibration, the calibration must be performed in an acoustic field with a known relationship between the acoustic pressure and the acoustic particle velocity. Free-field calibrations are advantageous because this relationship is known for both planar and spherical wave fronts. However,

reflections from waveguide boundaries present a practical limitation for free-field calibrations, especially at low frequencies. An alternative approach is to perform calibration measurements in a standing-wave field, where the relationship between pressure and particle velocity is also known. The calibration facility described in this thesis is composed of a laboratory-based, vertically-oriented, water-filled, elastic-walled waveguide with a piston velocity source at the bottom end and a pressure release boundary condition at the air/water interface at the top end. Some of the challenges of calibrating vector sensors in such an apparatus are discussed, including designing the waveguide to mitigate dispersion, mechanically isolating the apparatus from floor vibrations, understanding the impact of waveguide structural resonances on the acoustic field, and developing the calibration algorithms. Data from waveguide characterization experiments and calibration measurements are presented along with engineering drawings and calibration software.

Table of Contents

Acknowledgments **v**

Abstract **vi**

List of Tables **xi**

List of Figures **xii**

Chapter 1. Introduction **1**

1.1 Underwater Electroacoustic Receivers 1

1.2 Calibration of Underwater Electroacoustic Receivers 2

1.3 Thesis Objectives 6

Chapter 2. Theory and Design of Apparatus **9**

2.1 Discussion of Theory 9

2.1.1 Standing-Wave Theory 10

2.1.2 Waveguide Theory 14

2.1.2.1 Physics of a Rigid-Walled, Cylindrical Waveguide . 15

2.1.2.2 Elastic-Walled, Cylindrical Waveguide 17

2.2 Design of Apparatus 21

2.2.1 Design of Waveguide 22

2.2.1.1 Phase Velocity Estimation 23

2.2.1.2 Acoustic Pressure Field Estimation 25

2.2.2 Source Design 30

2.2.2.1 Piston Design 32

2.2.2.2 Compliance from O-ring 34

2.2.2.3 Shaker Selection 35

2.2.3 Isolation Systems 36

2.2.3.1 Waveguide Isolation System 37

2.2.3.2 Sensor Isolation System 38

2.2.4 Three-Dimensional Finite Element Analysis of Waveguide . 40

2.2.4.1 Results of Eigenfrequency Analysis 42
2.2.4.2 Results of Frequency-Dependent Acoustic Pressure Analysis 42
2.2.5 Reference Hydrophone, Sensor Positioning, and Data Collection Systems 46
2.2.5.1 Reference Hydrophone 48
2.2.5.2 Sensor Positioning System 48
2.2.5.3 Data Collection System 49

Chapter 3. Apparatus Characterization 51
3.1 Determination of Apparatus Stimulus Signal 51
3.2 Methodology for Obtaining a Repeatable Acoustic Field 53
3.3 Phase Velocity Measurements 55
3.4 Acoustic Pressure Field Measurements 56
3.5 Planar Wave Front Measurement 60
3.6 Vibration Isolation Testing 64
3.6.1 Waveguide Isolation System Measurements 64
3.6.2 Sensor Isolation System Measurements 68
3.7 Measured Piston Modes 69
3.8 Measured Three-Dimensional Structural Modes of the Waveguide . 72

Chapter 4. Calibration of Underwater Electroacoustic Receivers in a Standing-Wave Apparatus 77
4.1 Calibration Measurement Procedure 77
4.2 Calibration Measurement Post-Processing Algorithm 78
4.3 Sources of Calibration Error 82
4.4 Measurement Validation 85
4.4.1 Pressure Hydrophones 86
4.4.2 Pressure-Gradient Vector Sensors 87
4.4.3 Accelerometer-Based Vector Sensors 93
4.4.4 Commentary on Calibration Measurements 94

Chapter 5. Conclusion and Future Work 96

Appendices 100

Appendix A. Design Computations **101**
A.1 Lafleur and Shields Algorithm 101
A.2 Algorithm to Predict Acoustic Field within 16 inch Schedule 120 Steel Waveguide 105
A.3 Three-Dimensional Mode Shapes of 16 inch Schedule 120 Steel Waveguide Predicted by COMSOL 106

Appendix B. Standing-Wave Apparatus Calibration Measurement Procedure **110**

Appendix C. Standing-Wave Apparatus Calibration Measurement Post-Processing Algorithm **117**

Appendix D. Engineering Drawings **125**
D.1 Standing-Wave Apparatus Assembly 125
D.2 Waveguide Assembly 131
D.3 Waveguide Frame Assembly 137
D.4 Waveguide Support Frame Assembly 141
D.5 Sensor Isolation System 146
D.6 Linear Actuator Frame Assembly 154
D.7 Schematic of Degassing Hardware 156

Bibliography **158**

Vita **165**

List of Tables

2.1 Zeros of Bessel functions: roots α'_{mn} of $J'_m(x)$. 17

2.2 Input parameters to the Lafleur and Shields algorithm. Material parameters are the densities of steel and water ρ_p [28] and ρ_w, respectively, compressional and shear speed of sound in steel c_c and c_s, respectively, and speed of sound of pure water at 24° C c_w. Pipe dimensions are inner radius a and outer radius b from Ref. [26]. . 24

2.3 Candidate piston material properties 33

2.4 Eigenfrequencies and mode shapes of the waveguide as predicted by the COMSOL eigenfrequency model. Acoustic field disruptions were predicted by the COMSOL frequency-dependent acoustic pressure model. 43

List of Figures

1.1 Illustration of the receive voltage sensitivity (RVS) of a Teledyne RESON TC4013 hydrophone [14]. 3

1.2 Illustration of a directivity pattern of a typical USRL pressure-gradient vector sensor at 4 kHz from [13]. 4

2.1 Transfer function between acoustic pressure and piston velocity of a standing wave field with velocity and pressure release terminations at a depth of 1.5 m. 14

2.2 Comparison of modal phase velocities for a steel, water-filled waveguide with 0.344 m inside diameter and 0.406 m outside diameter when modeled as a rigid- and elastic-walled waveguide. Model input parameters are shown in Table 2.2. 20

2.3 Illustration of waveguide, source, and isolation systems. 21

2.4 Comparison of the modal phase velocities in 12 inch Schedule 120, 14 inch Schedule 120, and 16 inch Schedule 120 steel pipes. 25

2.5 Transfer function as determined by the analytical model between acoustic pressure and piston velocity as a function of frequency and depth below the air/water interface in the waveguide. 27

2.6 Axial derivative of the transfer function as determined by the analytical model between acoustic pressure and piston velocity (pressure gradient field) as a function of frequency and depth below the air/water interface in the waveguide. 28

2.7 Cross-sectional view of the waveguide, piston, base and bore o-rings, annular plate, diaphragm, and shaker. 31

2.8 First non-rigid mode of the source piston as computed from ANSYS eigenfrequency analysis. 34

2.9 Predicted transfer function between shaker output acceleration and input voltage for a Labworks Inc. FG-142 inertial shaker. 37

2.10 Waveguide isolation system: (a) mechanical model, (b) equivalent circuit model. 38

2.11 Predicted transmissibility curves of waveguide isolation system for a range of suspension mechanical resistances $R_{\mathrm{m,sus}}$. 39

2.12 Predicted transmissibility curve for the sensor isolation system. . . 41

2.13 Illustration of four of the mode shapes of the water-filled waveguide as computed by the COMSOL eigenfrequency model. 44

2.14 Predicted transfer function between acoustic pressure and piston velocity along the axis of revolution of the waveguide as determined from the COMSOL frequency-dependent acoustic pressure model. The arrows at the top of the figure highlight the predicted disruptions to the acoustic field at 555, 1080, and 1785 Hz. 45

2.15 Ratio of axial pressure gradient to radial pressure gradient computed from COMSOL frequency-dependent acoustic pressure model. (a) Frequency at which calibrations will likely produce valid results. (b)-(e) Frequencies at which calibrations may not produce valid results. 47

2.16 Schematic diagram of the data collection system. 49

3.1 Comparison of the spectral levels measured in the waveguide using swept-sine and periodic chirp stimuli. 53

3.2 Comparison of measured phase velocity to that predicted by the Lafleur and Shields algorithm. 57

3.3 Transfer function between the measured SPL along the waveguide axis of revolution and piston velocity. The arrows at the top of the figure highlight the disruptions to the acoustic field in a frequency band from 536 to 580 Hz, 1208, and 1733 Hz. 58

3.4 Comparison of measured and predicted transfer function between acoustic pressure and piston velocity along the waveguide axis of revolution 0.500 m below the air/water interface. The arrows in the figure highlight the disruptions to the acoustic field in a frequency band from 536 to 580 Hz, 1208, and 1733 Hz. 59

3.5 (a) Measured sound pressure level along the axis of revolution as a function of depth and frequency. (b) Axial pressure gradient computed from measured sound pressure level as a function of depth and frequency. The region where calibration measurements are performed is shown between the dotted lines 61

3.6 Acoustic pressure as a function of radial position and depth normalized by mean acoustic pressure across the inner diameter of the waveguide, p_{norm}. The various lines in each subplot represent a single depth in the waveguide. 63

3.7 Normalized acoustic pressure as a function of radius averaged across depths spanning 0.025 to 0.125 m. 64

3.8 Time series of waveguide velocity used to compute the damping ratio of the air springs using the log decrement method. 67

3.9 Simplified image of the sensor isolation system highlighting the locations of the shaker and velocimeters. Positions 1 to 4 show the measurement locations of the frame velocity. 69

3.10 Measured transmissibility of sensor isolation system. (a) Coherence of the measurement at each velocimeter position on the frame. (b) Transmissibility determined at each velocimeter position on the frame. (c) Coherent average of transmissibility at each velocimeter position on the frame. 70

3.11 (a) Schematic of the LDV setup for the piston velocity measurement. (b) Illustration of measurement points on the bottom of the piston. 71

3.12 Measured modes of apparatus source piston. 72

3.13 (a) Mode indicator function (black curve) of average waveguide wall acceleration and average acoustic pressure (red curve) as a function of frequency. (b) Waveguide wall acceleration averaged over the waveguide outside circumference as a function of axial position and frequency. The two arrows at the top of the figure highlight two modes with multiple nodes and anti-nodes along the waveguide axis of revolution. 75

3.14 Measured mode shapes of waveguide wall acceleration. The mode numbers of each shape illustrated correspond to the mode numbers on the MIF of Fig. 3.13(a). 76

4.1 Estimated error in calibration measurement $\varepsilon_{d,\text{mismatch}}$ for two pressure hydrophones placed at different depths and vector sensor directional channel post-processing error ε_d from incorrect depth for $d =$ 0.075 m. 83

4.2 Comparison of predicted phase velocities for three equilibrium temperatures in the standing-wave apparatus. 85

4.3 Illustration of calibration measurement setup of the Teledyne RESON TC4013 hydrophone calibration of LTTS. 88

4.4 Comparison of RVS for a Teledyne RESON TC 4013 in the standing-wave apparatus and at LTTS. 89

4.5 (a) Spherical to plane wave correction factor $\Xi_{\text{ff,sph}}$ for vector sensor directional channel calibrations performed in the geometric near-field of the source for a range of distances and frequencies for a 1491 m/s speed of sound. (b) $\Xi_{\text{ff,sph}}$ for 1.9 m source/receiver distance and 1491 m/s speed of sound and 0.8 m source/receiver distance and 1499 m/s speed of sound. 91

4.6 Comparison of the results of a pressure-gradient vector sensor calibration measurement between the standing-wave apparatus and at LTTS. 92

4.7 Comparison of the results of an accelerometer-based vector calibration measurement between the standing-wave apparatus and in a large tank. 95

A.1 Mode shapes 1 to 8 of waveguide as predicted by the COMSOL eigenfrequency model. 107

A.2 Mode shapes 9 to 16 of waveguide as predicted by the COMSOL eigenfrequency model. 108
A.3 Mode shapes 17 to 21 of waveguide as predicted by the COMSOL eigenfrequency model. 109

B.1 LabVIEW data collection system control GUI. 114
B.2 LabVIEW position control GUI. 115
B.3 LabVIEW ADC voltage range GUI. 116

Chapter 1

Introduction

1.1 Underwater Electroacoustic Receivers

Modern underwater electroacoustic receivers are ubiquitous and utilize various transduction methods to convert acoustic pressure into electrical signals. Pressure transducers are one of the most common types of underwater electroacoustic receivers. Piezoelectric materials are typically utilized to transduct acoustical waves into electrical signals where the amplitude of these signals is proportional to the acoustic pressure field to which the sensor is subjected [1]. Pressure tranducers are designed to measure the scalar pressure field, and therefore a single pressure transducer cannot reveal the direction to the source. However, source direction can be discerned by using signal processing techniques such as beamforming on the signals generated by multiple pressure transducers combined into a linear or planar array [2]. Linear arrays enable one to determine the bearing to a source but with ambiguity between which side of the array the signal is coming from in addition to depression and elevation angle ambiguities [3]. Moreover, planar arrays can require significant signal processing to find the direction to a source [4]. Another type of electroacoustic receiver is known as a vector sensor whose electrical signal amplitude is dependent on the relative orientation between its directional response axis and the acoustic source. This type of sensor allows directional information to be determined at a single point in space [5].

Acoustic vector sensors are often comprised of two or three spatially co-located, orthogonally-oriented, identical (ideally) velocity hydrophones where each hydrophone responds to either pressure gradient or directly to particle velocity, both of which are vector quantities, in one Cartesian component of the acoustic intensity field. Additionally, a single pressure hydrophone is typically co-located with the directional channels [6]. Directional channel transduction methods include inertial magnets, piezoelectric unimorphs, and accelerometers [7, 8]. The omni provides a phase reference for each directional channel where the user computes the cross-spectra between the directional channels and the omni channel in order to determine the bearing to a source [9]. The directional channels can be beamformed in order to achieve processing gain while multiple vector sensors can be combined on an array in order to achieve additional processing gain. Common applications of underwater acoustic vector sensors are anti-submarine warfare, harbor security, marine mammal research, and other underwater tracking applications [10–12].

1.2 Calibration of Underwater Electroacoustic Receivers

In order to quantify how the sensor's electrical output signal correlates with the acoustic pressure input, an electroacoustic receiver must be calibrated. This correlation is called a sensitivity function and the units are typically stated in V/μPa for pressure hydrophones and either V/μPa or V/m/s for vector sensors. Two calibrations are typically performed for acoustic receivers: on-axis receive voltage sensitivity (RVS), or simply receive sensitivity, and directivity measurements [13]. The receive sensitivity calibration is a measure of the device under test's (DUT) complex voltage response to the acoustic pressure field as a function of frequency where the DUT, source, and any reference sensor is held stationary

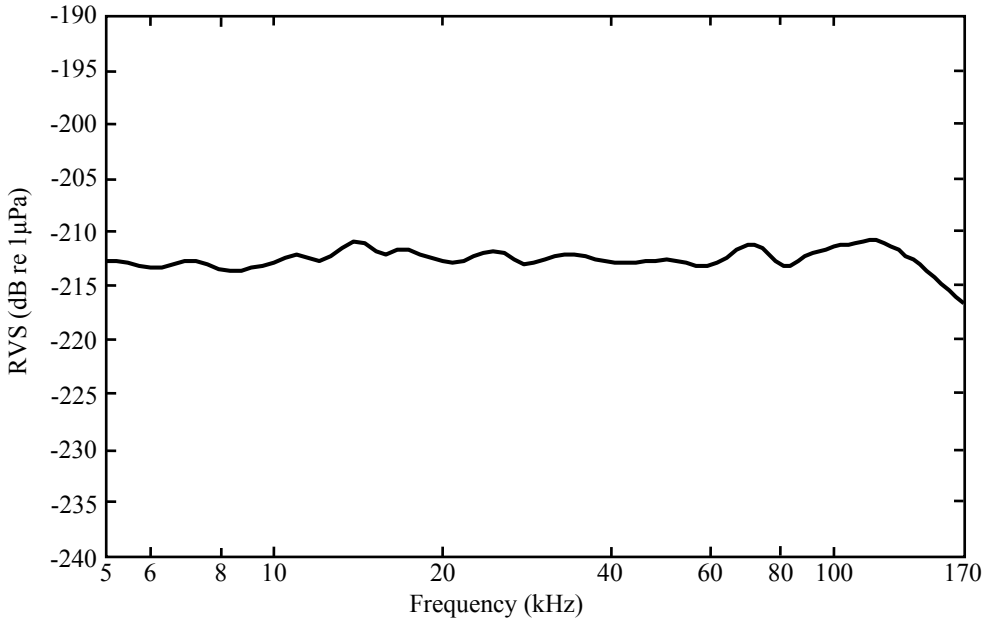

Figure 1.1: Illustration of the receive voltage sensitivity (RVS) of a Teledyne RESON TC4013 hydrophone [14].

and at a known position. The relative orientation between the DUT and the source will typically be such that the maximum signal level will be achieved from both the DUT and the source. An example of a receive sensitivity calibration provided by Teledyne RESON for a TC4013 hydrophone can be seen in Fig. 1.1. Receive sensitivity calibrations are generally produced in a field that is free of reflecting bodies and in the acoustic far-field of the source.

Directivity measurements are made in order to quantify the angular dependence of the DUT to the acoustic field. Depending on the intended use, one may desire the receiver to be highly directional or omnidirectional. In the case of vector sensors, one desires the sensitivity of the directional channels to be dependent on arrival angle in order to determine the bearing to the source. Directivity patterns

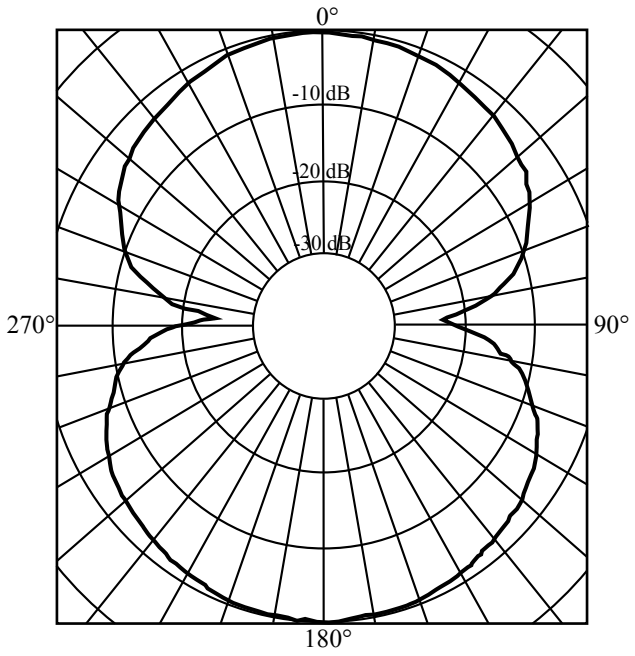

Figure 1.2: Illustration of a directivity pattern of a typical USRL pressure-gradient vector sensor at 4 kHz from [13].

are typically presented at a single frequency where the RVS as a function of angle is normalized by the on-axis receive sensitivity at that frequency. Hence for a plot stated in decibels, the off-axis response will be some "dB down" from the on-axis sensitivity [13]. Fig. 1.2 shows a directivity pattern for a typical Underwater Sound Reference Laboratory (USRL) pressure-gradient vector sensor at 4 kHz. From the figure, it is clear that the sensitivity of this sensor is highly directional at this frequency where the off-axis response is approximately 24 dB down from the on-axis response.

Acoustic receivers can be calibrated using a variety of techniques including comparison, reciprocity, two-projector null, and impedance methods [13]. For the sake of brevity and relevance to the vector sensor calibrations, only comparison

calibration techniques will be detailed in this thesis.

A common comparison calibration method is called the substitution method. This calibration technique is performed by first placing a calibrated transducer into a low-noise environment, subjecting it to acoustic pressure, and recording the open-circuit voltage response. Next, the calibrated transducer is replaced by the DUT, the DUT is subjected to the same acoustic pressure as for the calibrated transducer, and the recorded open-circuit voltage response is compared to the calibrated transducer. This method produces accurate results as long as the acoustic pressure field can be controlled and the transducers can be positioned precisely in order to minimize differences between measurements. A variation of the comparison method is to simultaneously subject both the standard transducer and DUT to the acoustic pressure field and record the transfer function between the two transducers. One advantage of this method includes the ability to ensure accurate positioning of the acoustic centers of the two transducers next to each other. Additionally, both transducers will be subjected to the same transient fluctuations in the acoustic pressure field that can introduce errors when using the true substitution method. On the other hand, this method can introduce errors when the presence of one transducer affects the pressure field that the other transducer is subjected to and vice-versa, or when the distance between the acoustic centers of the two transducers is no longer small compared to an acoustic wavelength. The comparison method is typically used to calibrate acoustic vector sensors to a reference pressure transducer and will be the case for all calibrations presented in this thesis.

The process of calibrating an acoustic vector sensor begins with performing

a comparison calibration between its omni hydrophone and an omnidirectional reference transducer. The subsequent directional channel calibrations are then determined by making a comparison calibration between each directional channel and the omni channel of the vector sensor [15]. This makes the use of simultaneous comparison calibration methods particularly useful since both the reference, omni, and directional channels will inherently be subjected to the same acoustic pressure field. Free-field vector sensor calibrations often require a very low noise field that is also free of reflecting surfaces. This requirement is difficult to achieve in practice, especially at low frequencies where the wavelengths can be on the order of tens of meters.

An alternative to a free-field, progressive-wave calibration is one performed in a standing-wave pressure field. A standing-wave field is created when two progressive waves at the same frequency and amplitude propagate in antiparallel directions. The two progressive waves interfere with each other constructively and destructively as a function of frequency and position along the propagation direction. Standing-wave fields can be used for vector sensor calibrations since they are easily created in a waveguide where the boundary conditions are well understood, the apparatus can be housed in a laboratory where the environment can be closely controlled, and the waveguide can be isolated from spurious noise sources.

1.3 Thesis Objectives

As a research component for this thesis, a vertically-oriented, water-filled, steel waveguide was designed and constructed. The waveguide is positioned within

a support frame and the system resides in a climate-controlled laboratory. The waveguide is decoupled from the floor by the use of air springs and is isolated from the frame by compliant straps. The waveguide is terminated at the lower end with a piston velocity source and on the upper end by a pressure release surface created by the air/water interface. The reference hydrophone and DUT are positioned by a computer-controlled linear actuator and all transducers are isolated from the frame and linear actuator motion by a mass-spring-damper system. Calibration data is collected and processed by a dynamic signal analyzer and is then downloaded and recorded on a personal computer (PC) where it is post-processed using MATLAB [16].

The organization of this thesis follows chronologically with the development of the calibration apparatus. It begins in Ch. 2 with a discussion of standing waves and waveguide theory along with the methodology used to design the calibration system, including theory used to predict phase velocity in an elastic waveguide. Chapter 3 describes the measurements conducted in order to characterize the apparatus. Measurements include determination of appropriate source signal types, phase velocity measurements, acoustic pressure measurements and computation of pressure gradients, planar acoustic pressure measurements taken in order to determine the degree of planarity of the wavefront, vibration isolation testing, two-dimensional structural mode measurements of the piston, and structural mode measurements used to visualize the three-dimensional modes of the waveguide. Chapter 4 describes the measurement procedures for calibrating pressure hydrophones and vector sensors, the post-processing algorithm used to relate the raw standing-wave measurement data to plane wave results, and validation of calibrations performed in the waveguide by comparing them to calibrations performed

in a free-field. Chapter 5 summarizes the research and provides a conclusion to this thesis and suggests future development. Finally, the appendices include design computations, instructions on how to perform comparison calibrations for pressure hydrophones and vector sensors in the apparatus, the post-processing algorithm used to correct the standing-wave field calibrations to free-field calibrations and generation of plots, and engineering drawings to construct an identical system.

Chapter 2

Theory and Design of Apparatus

The design of a standing-wave calibration apparatus required the knowledge of the physics of standing-wave fields, general waveguide theory and elastic waveguide theory, and equivalent circuit modeling of mechanical systems. Additionally, the complicated nature of the sound-structure interaction between the waveguide walls and the acoustic pressure field within the waveguide required finite element analysis (FEA) to predict three-dimensional modes of the waveguide. This chapter is divided into two main sections where Sec. 2.1 contains a discussion of standing-wave theory and rigid- and elastic-walled waveguide theory. Section 2.2 describes how the theory delineated in Sec. 2.1 guided the waveguide design and details the design of the subassemblies of the calibration apparatus.

2.1 Discussion of Theory

This section describes the theory used to develop the standing-wave apparatus. It begins in Sec. 2.1.1 with a derivation of the expressions for the acoustic pressure of a standing-wave field with a velocity boundary condition at one end and a pressure release boundary condition at the opposite end. Section 2.1.2 introduces waveguide theory for both rigid- and elastic-walled, cylindrical waveguides.

2.1.1 Standing-Wave Theory

Standing plane waves are created by the superposition of two antiparallel progressive plane waves. Such a wave field is created in the presence of reflecting boundaries and the details of the pressure fields are prescribed by the boundary conditions. For the purpose of this thesis, consider a pressure field in a rigid-walled pipe where one end is prescribed by a velocity boundary condition and the other end is a pressure release boundary. Such a system can be conceptualized by placing a rigid piston at the end of a vertically-oriented, water-filled pipe of length l in meters. The following derivation follows closely with that presented in Ch. 4 of Ref. [17] and makes use of the same nomenclature where the time harmonic velocity boundary condition can be described by

$$u(0, \omega, t) = u_0 e^{j\omega t}, \tag{2.1}$$

where u_0 is the velocity amplitude in meters per second, $j = \sqrt{-1}$, ω is the frequency in rad/s, and t represents time in units of seconds. The depth below the air-water interface, d, is described by

$$d = l - x, \tag{2.2}$$

where x is the distance from the point of interest to the velocity source in meters. Next, the pressure and particle velocities are described by

$$p(x, \omega, t) = P(x) e^{j\omega t}, \tag{2.3}$$

and

$$u(x, \omega, t) = U(x) e^{j\omega t}, \tag{2.4}$$

respectively, where P and U are typically complex-valued functions. In order to determine the expressions for P and U, one must first substitute Eq. (2.3) into the linearized wave equation for pressure,

$$c_0^2 \frac{\partial^2 p}{\partial x^2} - \frac{\partial^2 p}{\partial t^2} = 0, \tag{2.5}$$

where c_0 is the speed of sound of the fluid. The result is the Helmholtz equation whose solution is

$$P = Ae^{-jkx} + Be^{jkx}, \tag{2.6}$$

where A and B are coefficients whose values are determined by the boundary conditions and $k = \omega/c_0$ is the acoustical wave number. From this, the expression for U can be determined as

$$U = \frac{A}{Z_0} e^{-jkx} - \frac{B}{Z_0} e^{jkx}, \tag{2.7}$$

where

$$Z_0 = \frac{P}{U}, \tag{2.8}$$

and is the characteristic impedance of the fluid inside the pipe. Now, substitute Eq. (2.2) into Eqs. (2.6) and (2.7) to express P and U relative to the distance from the air/water interface. Eqs. (2.6) and (2.7) then become

$$P = Ae^{-jkl}e^{jkd} + Be^{jkl}e^{-jkd}, \tag{2.9}$$

and

$$U = \frac{A}{Z_0} e^{-jkl}e^{jkd} - \frac{B}{Z_0} e^{jkl}e^{-jkd}. \tag{2.10}$$

Next, the incident and reflected wave amplitudes can be expressed as $P^+ = Ae^{-jkl}$ and $P^- = Be^{jkl}$, respectively. Substitution of these expressions into Eq. (2.10) and using Eq. (2.8) can recast Eq. (2.10) as

$$U = U^+ e^{jkd} + U^- e^{-jkd}, \tag{2.11}$$

The amplitudes of P^+ and P^- can be used to determine the reflection coefficient by

$$R = \frac{P^-}{P^+}, \tag{2.12}$$

where an approximate value of R for an air/water interface from the perspective of the water is -1. Since $P^- = RP^+$, Eq. (2.9) can be recast as

$$P = P^+(e^{jkd} + Re^{-jkd}). \tag{2.13}$$

Substitution of R into Eq. (2.13) and rearranging results in

$$P/P^+ = e^{jkd} - e^{-jkd}, \tag{2.14}$$

and a similar rearrangement of Eq. (2.11) results in

$$U/U^+ = e^{jkd} + e^{-jkd}. \tag{2.15}$$

Now, substitute $d = l - x$ back into Eq. (2.15) and use Euler's formula to express U in a trigonometric form as

$$U = 2U^+ \cos(k(l - x)), \tag{2.16}$$

and substitute Eq. (2.16) into Eq. (2.4) to get

$$u(x, \omega, t) = 2U^+ \cos(k(l - x))e^{j\omega t}. \tag{2.17}$$

Now, implement the boundary condition $u(0, \omega, t) = u_0 e^{j\omega t}$ and rearrange to solve for U^+ as

$$U^+ = \frac{u_0}{2\cos(kl)}, \tag{2.18}$$

and, finally, substitute the expression for U^+ into Eq. (2.17) to recover an expression for the particle velocity at any point in the field as

$$u(x, \omega, t) = u_0 \frac{\cos(k(l-x))}{\cos(kl)} e^{j\omega t}. \tag{2.19}$$

Euler's equation states that for an unknown impedance, the relation between the acoustic pressure and particle velocity of a one-dimensional plane wave is

$$u(x, \omega, t) = \frac{-1}{j\omega\rho_0} \frac{\partial p(x, \omega, t)}{\partial x}, \tag{2.20}$$

where ρ_0 is the density of the fluid. Using this expression, it can be found that the equation for the acoustic pressure at any point in the field is

$$p(x, \omega, t) = j\rho_0 c_0 u_0 \frac{\sin(k(l-x))}{\cos(kl)} e^{j\omega t}. \tag{2.21}$$

The impedance of the standing-wave field can be determined by substituting Eqs. (2.19) and (2.21) into Eq. (2.8) and is

$$Z(x, \omega)_{\text{sw}} = j\rho_0 c_0 \tan(k(l-x)). \tag{2.22}$$

An obvious feature of standing waves is the existence of local maxima and minima in the acoustic pressure and particle velocity fields due to the constructive and destructive interference of the antiparallel progressive waves. The resultant pressure field can be cast as the transfer function between the acoustic pressure and the source velocity as

$$H_{\text{pvel}}(x, \omega) = \frac{p(x, \omega, t)}{u(0, \omega, t)} = j\rho_0 c_0 \frac{\sin(k(l-x))}{\cos(kl)}. \tag{2.23}$$

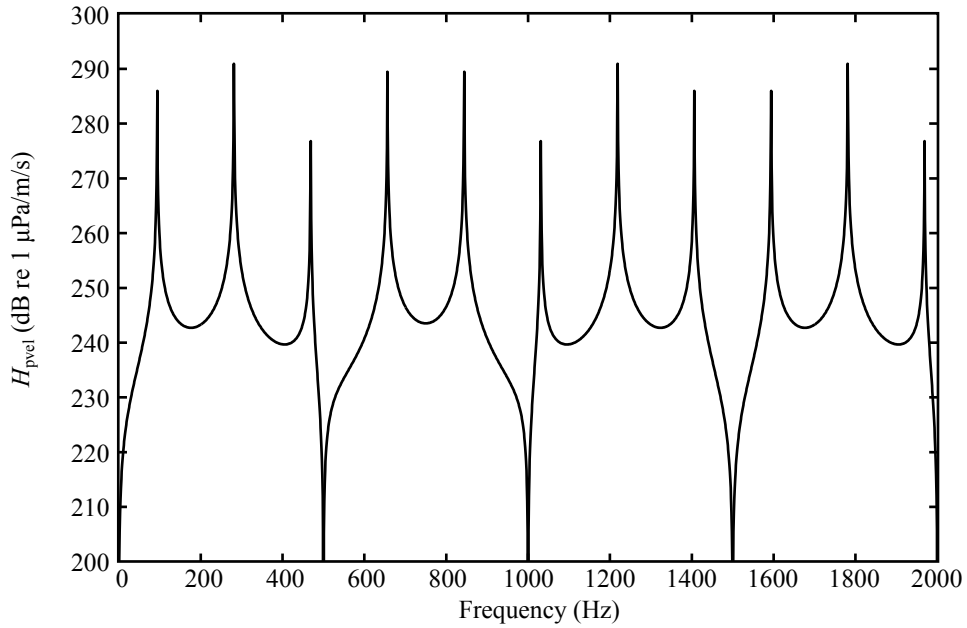

Figure 2.1: Transfer function between acoustic pressure and piston velocity of a standing wave field with velocity and pressure release terminations at a depth of 1.5 m.

Figure 2.1 shows the magnitude of $H_{\text{pvel}}(x, \omega)$ at a depth of 1.5 m below the air/water interface as a function of frequency where both the dynamic range and the harmonic relation of the peaks and nulls of the acoustic pressure are apparent.

2.1.2 Waveguide Theory

An acoustic standing-wave field can be created in a waveguide, which is an environment where both progressive and standing-waves can coexist. As an example, consider a semi-infinite, rigid-walled pipe with a piston velocity source at one end. If the velocity source excites the system in an orientation other than one

that is parallel with the axis of revolution of the waveguide, both progressive and standing waves can exist in the pipe. Section 2.1.2.1 will introduce the reader to the physics of semi-infinite, rigid-walled, cylindrical waveguides where the author closely follows the content and uses the same nomenclature as found in Ch. 6-D and Ch. 12 of Ref. [17]. Section 2.1.2.2 provides a qualitative discussion of the effects of an elastic-walled, cylindrical waveguide on the acoustic field.

2.1.2.1 Physics of a Rigid-Walled, Cylindrical Waveguide

For a fluid-filled, rigid-walled, cylindrical waveguide the general expression for acoustic pressure in the fluid within the waveguide is

$$p(r,\theta,z,\omega,t) = \begin{Bmatrix} J_m(k_r r) \\ N_m(k_r r) \end{Bmatrix} \begin{Bmatrix} \cos(m\theta) \\ \sin(m\theta) \end{Bmatrix} \begin{Bmatrix} e^{j\beta z} \\ e^{-j\beta z} \end{Bmatrix} \begin{Bmatrix} e^{j\omega t} \\ e^{-j\omega t} \end{Bmatrix}, \tag{2.24}$$

where $J_m(k_r r)$ is the Bessel function of the first kind and $N_m(k_r r)$ is the Neumann function and are dependent on the radial wave number k_r and radial position r. Further, β is the frequency-dependent wave number inside the waveguide, and z is the position along the axis of revolution of the waveguide. The trigonometric functions found in the second bracket describe the angular dependence of a given mode m which can have an integer value of 0 to ∞. The dispersion relation describes the frequency dependence of the wave number and is defined as

$$\beta^2 = (w/c_0)^2 - {k_r}^2, \tag{2.25}$$

for a cylindrical waveguide. In order to describe the example system, one simplifies the general solution found in Eq. (2.24) by eliminating terms as prescribed by the boundary conditions. This is accomplished by elimination of $N_m(k_r r)$ due to the inclusion of the origin, $e^{j\beta z}$ to describe wave propagation in the positive

z direction only, and $e^{-j\omega t}$ to match the source condition. Furthermore, for a rigid-walled pipe, the boundary condition at the fluid-wall interface of the pipe, $r = a$, is $u^{(r)}(k_r a) = 0$ and is satisfied by choosing

$$k_r = \alpha'_{mn}/a, \tag{2.26}$$

where α'_{mn} is the nth zero of J'_m which is tabulated in Table 2.1. The full solution for the acoustic pressure for the given boundary conditions becomes

$$p = \sum_{m=0}^{\infty}\sum_{n=1}^{\infty} J_m\left(\frac{\alpha'_{mn}r}{a}\right)[A_{mn}\cos(m\theta) + B_{mn}\sin(m\theta)]e^{j(\omega t-\beta_{mn}z)}, \tag{2.27}$$

where the terms A_{mn} and B_{mn} are modal coefficients and are determined by the source. Substitution of Eq. (2.26) into Eq. (2.25) produces the dispersion relationship

$$\beta_{mn} = \sqrt{(\omega/c_0)^2 - (\alpha'_{mn}/a)^2}, \tag{2.28}$$

and the phase velocity is

$$c^{\text{ph}}_{mn} = \frac{\omega}{\beta_{mn}}. \tag{2.29}$$

Substitution of Eq. (2.28) into Eq. (2.29) and rearranging results in

$$c^{\text{ph}}_{mn} = \frac{c_0}{\sqrt{1 - (\alpha'_{mn}c_0/2\pi f a)^2}}, \tag{2.30}$$

where f is the frequency in Hz. From inspection of Eq. (2.30), it can be seen that at very high frequencies the phase velocity in the waveguide will approach that of the intrinsic speed of sound of the fluid inside the waveguide. However, as the frequency is decreased, the phase velocity increases until it reaches a singularity at

$$f^{\text{c}}_{mn} = \frac{\alpha'_{mn}c_0}{2\pi a}, \tag{2.31}$$

Table 2.1: Zeros of Bessel functions: roots α'_{mn} of $J'_m(x)$.

n	$m=0$	$m=1$	$m=2$	$m=3$	$m=4$
1	0	1.841	3.054	4.201	5.318
2	3.832	5.331	6.706	8.015	9.282
3	7.016	8.236	9.969	11.346	12.682
4	10.173	11.706	13.170	14.586	153964
5	13.324	14.864	16.348	17.789	19.196

where f^{c}_{mn} is the mode-dependent cutoff frequency. At frequencies below cutoff for a given mode, the wave number is imaginary and no progressive waves are able to propagate along the waveguide. Instead, only evanescent waves exist.

In the case of a standing-wave calibration apparatus, the only desired mode is the plane wave mode, or the mode associated with $m = 0$. This ensures that only waves propagating along the axis of revolution of the waveguide are excited. Additionally, the plane wave mode can exist to zero frequency as determined from Eq. (2.31) when $\alpha'_{mn} = 0$ and allows the low frequency limit within the waveguide to be determined by the source since, when $m = 0$ and $n = 1$ from Table 2.1, and, from Eq. (2.31), $f^{c}_{mn} = 0$ Hz. In the case of a rigid-walled waveguide, the phase velocity of the plane wave mode will be that of the intrinsic speed of sound in the free fluid as seen in Eq. (2.30).

2.1.2.2 Elastic-Walled, Cylindrical Waveguide

For a real waveguide filled with water, the acoustic impedances of water and that of most elastic solids are similar enough that the walls cannot be approximated as rigid and the motion of the waveguide walls must be considered [18–20]. Signifi-

cant research into axisymmetric wave propagation in liquid-filled, elastic-walled cylinders has been performed and, for this thesis, the disperion relation developed by Del Grosso [21] and later simplified by Lafleur and Shields [22] has been used for the basis of the waveguide design. The expressions derived by Lafleur and Shields are not repeated in this thesis but the MATLAB code that solves these expressions is contained in Appendix A.1 and is referred to as the Lafleur and Shields algorithm for the remainder of this thesis. A qualitative description of the theory is contained in the remainder of this section and establishes a design methodology when using the Lafleur and Shields algorithm to design a cylindrical, water-filled waveguide.

As described in Sec. 2.1.2.1, the phase velocity for the plane wave mode in a rigid-walled waveguide is that of the free-field speed of sound of the medium within the waveguide. For a fluid-filled, elastic-walled waveguide the phase velocity for the plane wave mode (designated the ET0 mode by Del Grosso, where E denotes an elastic wall and T denotes that the wall is of finite thickness) will be reduced from that of the free-fluid. This is due to the motion of the elastic waveguide wall under the influence of the acoustic pressure where the compliance of the wall is higher than that of the fluid. Additionally, the waveguide wall motion induces radial particle motion within the fluid of the waveguide which causes the axial wavefront to become non-planar. The degree of non-planarity can be assessed by the relative deviation of the phase velocity from the intrinsic speed of sound of the fluid. Therefore, as a design metric, it is desirable to achieve phase velocities in the waveguide as close as possible to that of the intrinsic speed of sound of the fluid in order to minimize the amplitude of the radial particle motion for the ET0 mode. The next higher-order mode of an elastic-walled waveguide

(designated the ET1 by Del Grosso) also exists to zero frequency and is caused by the coupling between the waveguide walls and the included fluid. While exciting this mode is unavoidable, it is possible to minimize its amplitude by using a planar, longitudinally-vibrating piston, by ensuring that the acoustic source is isolated from the waveguide walls, and by choosing a waveguide length that places the lowest longitudinal standing-wave mode present for ET1 above the frequency range of interest when using ET0 [23].

Figure 2.2 compares the differences in the first four modes of an elastic-walled waveguide computed from the Lafleur and Shield algorithm to the first two longitudinal modes of a rigid-walled waveguide computed from Eq. (2.30) using the parameters described in Table 2.2 for a 16 inch Schedule 120 pipe. Figure 2.2 shows that the first two modes of the elastic-walled waveguide, ET0 and ET1, exist to zero frequency and that the phase velocity of the plane wave mode of the rigid-walled waveguide, (0,1), equals the intrinsic speed of sound of the fluid. Also, Fig. 2.2 illustrates the cutoff phenomena exhibited by the higher-order modes of both the rigid- and elastic-walled waveguides.

The following trends in the prediction of the phase velocity of the ET0 mode were observed and are listed to provide "rules of thumb" for designing a cylindrical, water-filled, elastic-walled waveguide:

- for a given diameter and wall thickness, the phase velocity is proportional to the speed of sound in the pipe material
- for a given diameter and material, the phase velocity is proportional to the wall thickness

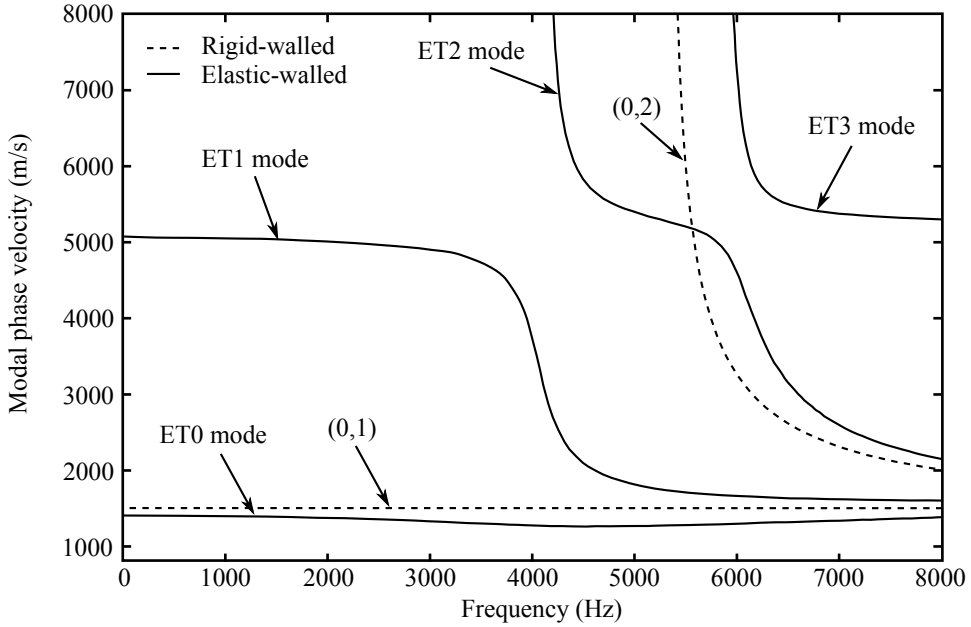

Figure 2.2: Comparison of modal phase velocities for a steel, water-filled waveguide with 0.344 m inside diameter and 0.406 m outside diameter when modeled as a rigid- and elastic-walled waveguide. Model input parameters are shown in Table 2.2.

- for a given wall thickness and material, the phase velocity is indirectly proportional to the waveguide diameter.

From the observed trends, the phase velocity inside the waveguide will approach the intrinsic speed of sound in the fluid when the inside diameter is minimized and the wall thickness and speed of sound of the waveguide material are maximized. The design goal of maximizing the phase velocity within the waveguide must be balanced with engineering considerations such as the size of the DUT to be measured and the cost and availability of waveguide materials.

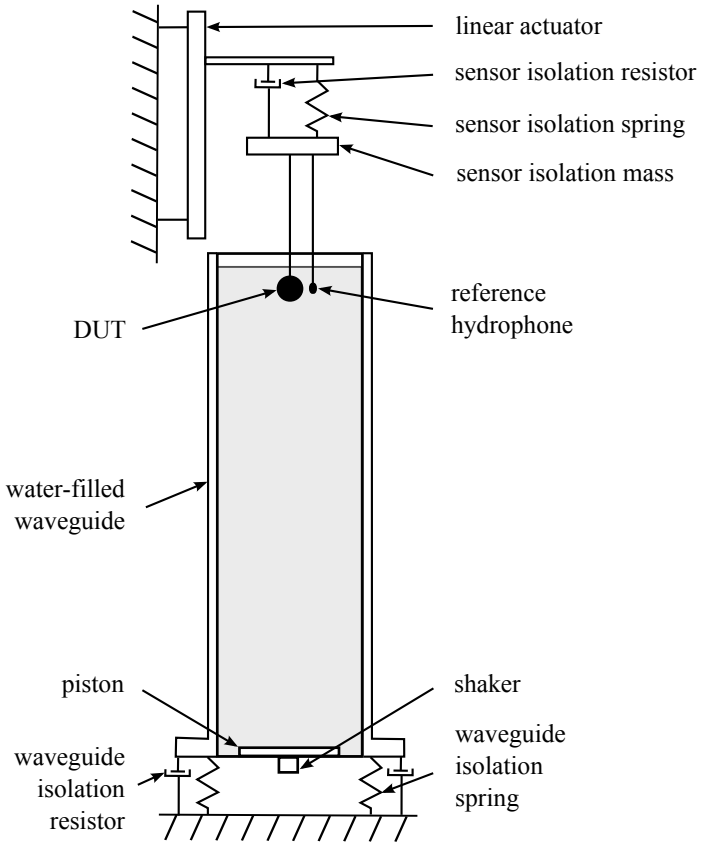

Figure 2.3: Illustration of waveguide, source, and isolation systems.

2.2 Design of Apparatus

The design of this apparatus, as with most engineering designs, was an iterative process. The apparatus is an electro-mechano-acoustical system composed of the waveguide, a source, and isolation and data collection subsystems. Figure 2.3 illustrates the waveguide, source, and isolation systems.

The remainder of this chapter is devoted to the design of the apparatus. It begins in Sec. 2.2.1 with a description of the design of the waveguide. Section 2.2.2 contains a discussion of the methods used to design the source. Next, Sec. 2.2.3

describes the waveguide and sensor mechanical isolation systems. Section 2.2.4 discusses the three-dimensional sound-structure interaction FEA modeling of the acoustic pressure field and, lastly, Sec. 2.2.5 contains a description of the reference hydrophone, sensor positioning system, and data collection system.

2.2.1 Design of Waveguide

The waveguide was the first subsystem designed. For this component, the author was constrained by the practical limits of cost and availability of candidate waveguide materials in addition to the dimensions of the laboratory space. Literature reviews of prior art indicated that usable circular cross-section pipe materials range from thin-walled polyvinyl chloride to thick-walled steel [15, 24]. It was the author's intention to create an apparatus that could calibrate vector sensors as large as 0.1 m in diameter from frequencies at or near the infrasonic range up to several kHz. To this end, the following criteria as delineated by McConnell [15] were applied:

- the size of the DUT must be small when compared to a wavelength based on the phase velocity in the waveguide
- the size of the DUT must be small when compared to the diameter of the waveguide so that it does not obstruct the acoustic field within the waveguide
- the wavefronts must be sufficiently planar to minimize the difference between the acoustic field at the DUT and at the reference hydrophone.

As laid out in the elastic-walled waveguide discussion presented in Sec. 2.1.2.2, the waveguide diameter, wall thickness, and material will determine the phase

velocity of a water-filled waveguide and, subsequently, the usable frequency band of the apparatus. Moreover, both the waveguide walls and source piston are susceptible to structural vibrations that may alter the usable frequency band and must be considered in the design of the apparatus. Sec. 2.2.1.1 describes the process of material selection and the determination of diameter and wall thickness, and Sec. 2.2.1.2 illustrates how the phase velocity affects the acoustic pressure field within the waveguide.

2.2.1.1 Phase Velocity Estimation

Since it is desirable that the calibration apparatus operate in the widest frequency band possible, it was important for the phase velocity to be as close to the intrinsic speed of sound as possible in order to maximize the acoustic wavelength for a given frequency. For this reason, waveguides constructed from polymers were excluded from consideration since their high compliance would significantly reduce the phase velocity. Additionally, aluminum pipes of large cross-section were difficult to find and were limited to 12 inch outside diameters [25] and stainless steel pipes were prohibitively expensive. Consequently, the author focused on analyzing seamless structural steel pipes with outside diameters in the range of 12 to 16 inches due to their relatively low cost, wide availability, and high fabrication quality [26, 27]. The phase velocities for 12 inch Schedule 120, 14 inch Schedule 120, and 16 inch Schedule 120 pipes were estimated by the Lafleur and Shields algorithm using the parameters shown in Table 2.2 and the results are shown in Fig. 2.4 for the first three modes: ET0, ET1, and ET2. Figure 2.4 also shows that similar phase velocities could be obtained for the ET0 mode in the three pipes between 0 and 5000 Hz. In order obtain a closed-form expression for

Table 2.2: Input parameters to the Lafleur and Shields algorithm. Material parameters are the densities of steel and water ρ_p [28] and ρ_w, respectively, compressional and shear speed of sound in steel c_c and c_s, respectively, and speed of sound of pure water at 24° C c_w. Pipe dimensions are inner radius a and outer radius b from Ref. [26].

Material properties				Pipe dimensions (m)		
pipe		water		Nominal size	b	a
ρ_p	7850 (kg/m^3)	ρ_w	997 (kg/m^3)	12 inch Sch. 120	0.162	0.137
c_c	5583 (m/s)[a]	c_w	1494 (m/s)	14 inch Sch. 120	0.178	0.15
c_s	3178 (m/s)[b]			16 inch Sch. 120	0.203	0.172

[a] Computed from $c_c = \sqrt{\frac{E(1-\nu)}{\rho_p(1+\nu)(1-2\nu)}}$ [29] where E is the elastic modulus and ν is Poisson's ratio. Material properties from Ref. [28].

[b] Computed from $c_s = \sqrt{\frac{G}{\rho_p}}$ [29] where G is the shear modulus from Ref. [28].

the phase velocity as a function of frequency for the ET0 mode of the 16 inch Schedule 120 pipe, a polynomial curve fitting routine in MATLAB was used to parameterize the curve of that mode shown in Fig. 2.4 as

$$c_{\mathrm{ET0}}^{\mathrm{ph}} = -7.39 \times 10^{-6}(\omega/2\pi)^2 + 0.0018(\omega/2\pi) + 1397, \tag{2.32}$$

and is valid in a frequency band from 20 to 2000 Hz at 24°C. Figure 2.4 also illustrates the existence of the ET1 mode at zero frequency where the amplitude of this mode was minimized by isolating the source piston from the walls of the annular plate using o-rings as will be described in Sec. 2.2.2.1.

In addition to the effect of phase velocity, the practical upper limit of the waveguide internal diameter also depends on the cutoff frequency of the first cross mode, labeled ET2 in Fig. 2.4. These modes are highly non-planar and must be avoided. The lowest cutoff frequency of the ET2 modes for the three pipes analyzed occurs at approximately 4250 Hz for the 16 inch Schedule 120 pipe.

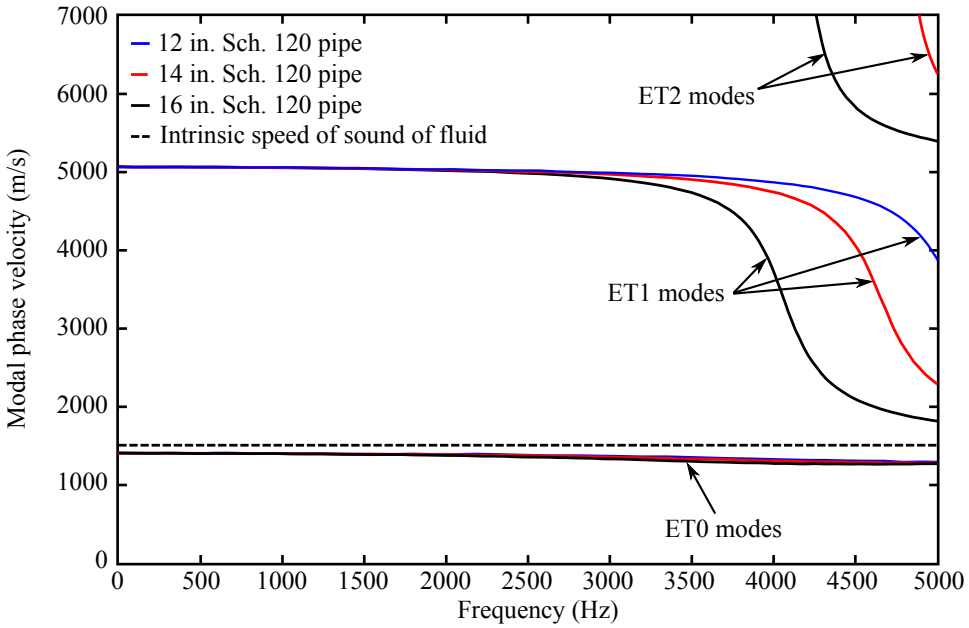

Figure 2.4: Comparison of the modal phase velocities in 12 inch Schedule 120, 14 inch Schedule 120, and 16 inch Schedule 120 steel pipes.

2.2.1.2 Acoustic Pressure Field Estimation

Axial acoustic resonance frequencies in a standing-wave field are determined by the phase velocity, waveguide length, and source impedance. A simple model of the acoustic pressure field can be determined from knowledge of the phase velocity inside the waveguide as determined by the Lafleur and Shields algorithm. For the standing-wave apparatus, the maximum length of the waveguide was limited by the ceiling height of the laboratory in which the waveguide is housed. The location chosen for the calibration apparatus was a large assembly building with a ceiling height of approximately 7.5 m that contains a mezzanine approximately 3.5 m above the floor. From the mezzanine, an operator can easily access the top of the waveguide in order position the reference hydrophone and the DUT for calibration

work. From these dimensions, it was decided that the laboratory could support a 4 m long waveguide and also have enough vertical clearance to add a scanning system capable of reaching depths of 1.5 m in the waveguide.

Since the source impedance was unknown at this point in the design, the transfer function between the acoustic pressure and the source velocity was computed in order to understand where the pressure extrema would occur in depth. To that end, the transfer function of Eq. (2.23) was recast

$$H_{\text{pvel}}(x,\omega) = \frac{p(x,\omega,t)}{u(0,\omega,t)} = j\rho_0 c_{\text{eff}} \frac{\sin(k_{\text{eff}}(l-x))}{\cos(k_{\text{eff}} l)}, \tag{2.33}$$

where

$$k_{\text{eff}} = \frac{\omega}{c_{\text{eff}}} + (1-j)\alpha_{\text{walls}}, \tag{2.34}$$

c_{eff} is the frequency-dependent phase velocity as determined by the Lafleur and Shields algorithm and can be represented by $c_{\text{ET0}}^{\text{ph}}$ from Eq. (2.32), and α_{walls} accounts for the viscous loss from the interaction between the waveguide walls and the water, characterized by [23]

$$\alpha_{\text{walls}} = \frac{1}{a}\sqrt{\frac{\mu\omega}{2\rho_0 c_{\text{eff}}^2}}, \tag{2.35}$$

where μ is the viscosity of water and is 0.907×10^{-3} kg/(m·s) at 24°C. The transfer function, $H_{\text{pvel}}(x,\omega)$ is shown in Fig. 2.5 and illustrates the existence of the extrema in the acoustic pressure field. From Fig. 2.5, the pressure maxima are equally spaced in frequency and the number of pressure nulls for a given frequency as a function of depth is proportional to frequency. Additionally, nulls in the acoustic pressure field are absent in the region between the air/water interface and a depth of approximately 0.5 m between 0 and 2000 Hz.

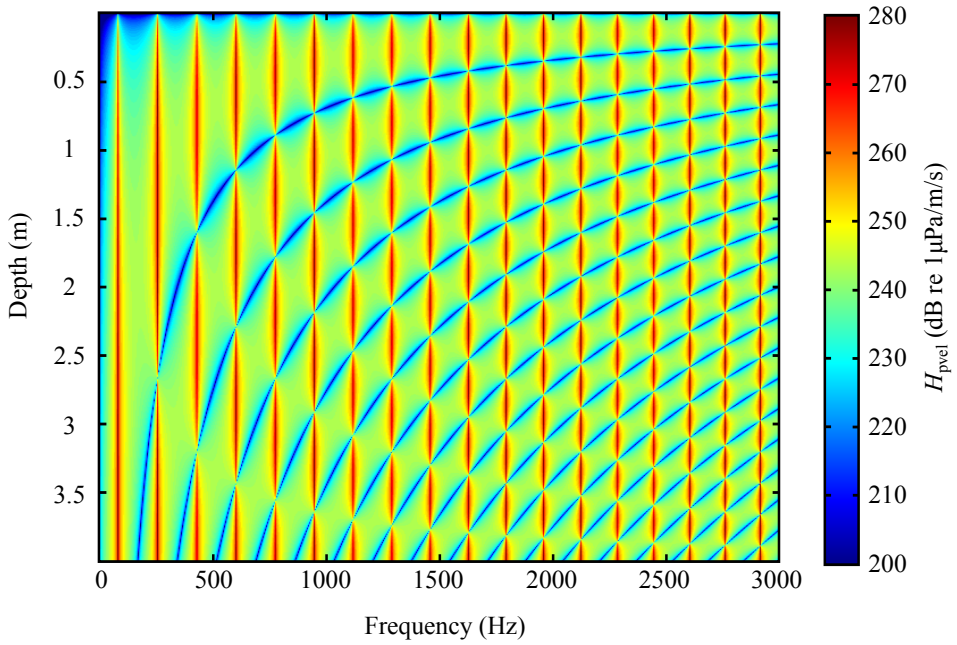

Figure 2.5: Transfer function as determined by the analytical model between acoustic pressure and piston velocity as a function of frequency and depth below the air/water interface in the waveguide.

The voltage response of pressure gradient and accelerometer-based vector sensors is proportional to the pressure gradient of the acoustic field to which they are subjected. Due to the presence of peaks and nulls in the acoustic pressure of a standing-wave field, peaks and nulls will also occur in the pressure gradient field. The spatial derivative of Eq. (2.33) taken along the waveguide axis of revolution is

$$\frac{\partial H_{\text{pvel}}(x,\omega)}{\partial x} = -\omega\rho\frac{\cos(k_{\text{eff}}(l-x))}{\cos(k_{\text{eff}}l)}, \tag{2.36}$$

and the magnitude of this transfer function is displayed in Fig 2.6. An apparent

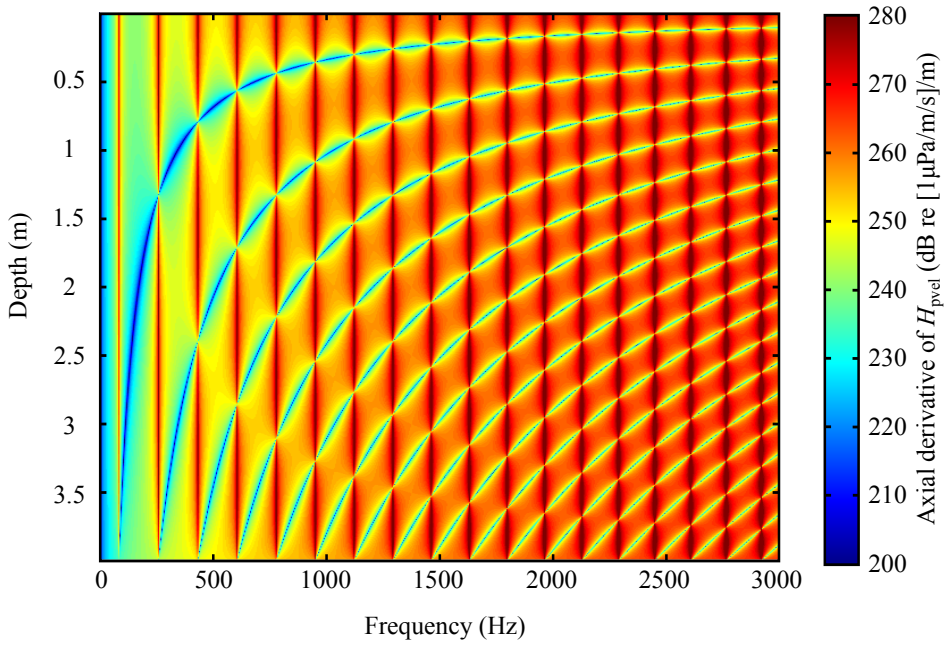

Figure 2.6: Axial derivative of the transfer function as determined by the analytical model between acoustic pressure and piston velocity (pressure gradient field) as a function of frequency and depth below the air/water interface in the waveguide.

feature of the pressure and pressure gradient fields are that the axial locations of the nulls in the pressure gradient field at a given frequency occur at the pressure field maxima and vice versa.

In addition to pressure-gradient and accelerometer-based vector sensors, the apparatus needed to be able to produce calibrations of geophone-based vector sensors, whose response is proportional to particle velocity. As with pressure-gradient vector sensors, the ability to produce calibrations of geophone-based

vector sensors depends on the ability to identify the locations of nulls in the particle velocity field. The transfer function between particle and piston velocities as a function of depth in the waveguide can be computed by combining Eq. (2.19) with Eq. (2.1) and accounting for the frequency-dependent phase velocity

$$H_{\text{uvel}}(x,\omega) = \frac{u(x,\omega,t)}{u(0,\omega,t)} = \frac{\cos(k_{\text{eff}}(l-x))}{\cos(k_{\text{eff}}l)}, \tag{2.37}$$

where the locations of the peaks and nulls are the same as for the pressure gradient field.

The existence of pressure and pressure gradient nulls significantly reduces the number of regions in which vector sensor calibration measurements can be performed since the acoustic field is rapidly changing in these regions. Inspection of Figs. 2.5 and 2.6 reveals the only region that is free of nulls in the acoustic field across the entire frequency band is that region between the air/water interface and the shallowest null in the pressure gradient and particle velocity fields. For this reason, vector sensor calibration measurements will be performed in the region just below the air/water interface.

Additional inspection of Figs. 2.5 and 2.6 reveals that the highest frequency region approximately 0.1 m wide that is unaffected by nulls in the acoustic field occurs around 2 kHz and sets a practical high frequency limit for performing calibration measurements in the standing-wave apparatus. From this high frequency limit, the bandwidth of the waveguide is 0 to 2000 Hz where the low-frequency limit of the apparatus will be bounded by the source. Since the high frequency limit of the standing-wave apparatus was determined by the axial distance between the air/water interface and the shallowest null in the pressure gradient field, the largest of the three pipes analyzed, 16 inch Schedule 120, was chosen for the waveguide

since it maximized the ratio of waveguide inner diameter to DUT diameter while exhibiting a similar ET0 mode phase velocity to the smaller pipes analyzed. For completeness, corrosion was mitigated by hot-dip galvanizing the steel waveguide weldment.

2.2.2 Source Design

The theory of standing wave fields laid out in Sec. 2.1.1 requires a velocity source at the lower terminus of the waveguide to reduce the first resonance frequency so that it occurs when $l = \lambda_{1A}/4$, where λ_{1A} is the acoustic wavelength at the first resonance frequency. Such a source can be designed with a shaker attached to a piston that is allowed one degree of freedom along the axis of revolution of the waveguide where the following criteria are met:

- the piston/shaker assembly is capable of producing a sound pressure level (SPL) in the waveguide that allows for near-unity coherence across the frequency band of interest for DUT calibration measurements
- the piston design does not support structural modes in the frequency band of interest
- the piston/shaker assembly is sufficiently isolated from the waveguide walls
- the piston/shaker assembly is isolated from the floor
- the piston/surround assembly is capable of supporting the weight of 4 m of water.

To meet the aforementioned criteria, the design shown in Fig. 2.7 was conceived. A flange is welded to the bottom end of the waveguide and accommo-

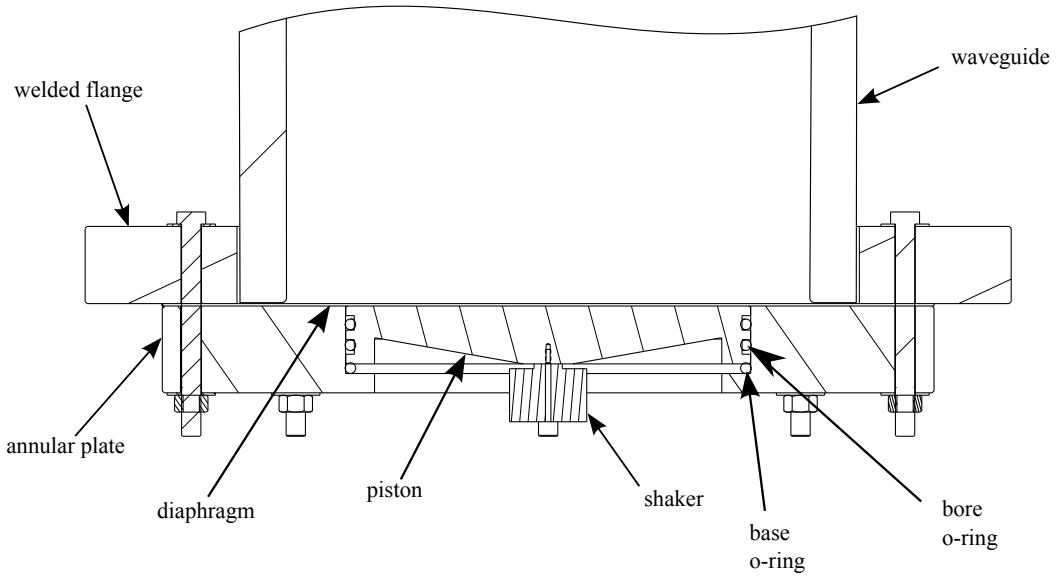

Figure 2.7: Cross-sectional view of the waveguide, piston, base and bore o-rings, annular plate, diaphragm, and shaker.

dates the bolting of a large, annular plate which supports an aluminum piston. The piston is isolated from the annulus by light-fitted bore o-rings and piston compliance is provided by a base o-ring that resides between the piston and a lip on the annular plate. The design of the piston required a balance between maximizing stiffness while minimizing mass in order to support the weight of the water and to avoid supporting structural modes while minimizing the mass-induced impedance of the source. A thin diaphragm between the waveguide flange and annular plate rests above the piston and acts as a water-tight seal without significantly impeding the motion of the piston.

2.2.2.1 Piston Design

The first component of the piston/shaker assembly to be designed was the piston. As mentioned in Sec. 2.2.2, the piston should be sufficiently stiff so that any structural modes of the piston would occur above the high frequency limit of the waveguide (2 kHz) and to support the weight of 4 m of water across the piston face. Candidate piston materials included 304 stainless steel, grade 2 titanium, and 6061-T6 aluminum. As a first order approximation, the author down-selected from these candidates by determining the material whose mass and stiffness would maximize the resonance frequency of a one-dimensional simple harmonic oscillator, $\sqrt{k_\mathrm{s}/m_\mathrm{w}}$, where k_s is the spring stiffness and is proportional to the elastic modulus of the material, E, and m_w is the mass of the weight and is proportional to the density of the material, ρ. Therefore the resonance of a one-dimensional simple harmonic oscillator f_res is proportional to $\sqrt{E/\rho}$. The yield strength, σ_s, of the three candidate materials is very similar, and therefore, the geometry of the piston design would not need to change for each piston material to accommodate supporting the weight of the water. The pertinent mechanical properties of the candidate piston materials and the results of the one-dimensional oscillator calculation are included in Table 2.3 where it is shown that 6061-T6 aluminum has the highest equivalent one-dimensional resonance frequency, but only nominally. Other benefits associated with the choice of aluminum for the piston material were its low mass and cost and high machinability, and therefore, it was chosen for the piston material.

The geometry of the piston is axisymmetric where the piston/water interface was chosen to be as flat as possible in order to avoid exciting any waveguide modes

Table 2.3: Candidate piston material properties

Material	E (GPa)	ρ (kg/m^3)	σ_s (MPa)	$\sqrt{E/\rho}$ (Hz)
6061-T6 aluminum [30]	68.9	2700	276	5052
304 stainless steel [31]	193	8000	205	4911
Gr. 2 Titanium [32]	102.7	4510	280	4772

other than the ET0 mode. The geometry of the back side of the piston was chosen so that the piston mass around the outer circumference would be minimized and the stiffness would be biased towards the piston center. The back side of the piston resembles that of a loudspeaker cone. A detailed engineering drawing can be found in Appendix D.1.

To ensure that the lowest structural mode of the piston was above 2 kHz, an ANSYS DesignSpace [33] eigenfrequency finite element analysis (FEA) was performed where the piston was modeled *in vacuo* with free edges. The model predicted that the first non-rigid body mode is one of a twisting type and occurs at approximately 2.1 kHz. This fundamental mode shape is consistent with plate vibration theory [34] and an image of this mode shape can be seen in Fig. 2.8. It should be noted that the outside diameter of the final piston design was 0.266 m and was smaller than the inside diameter of the pipe (0.344 m) in order to increase the frequency at which the lowest non-rigid body mode of the piston appears. The reduction in piston diameter from that of the waveguide wall will result in a reduction of the volume velocity of the water within the waveguide and, therefore, also a reduction of the acoustic pressure by the proportion $A_{\text{piston}}/A_{\text{pipe}}$ where A_i is the area of each.

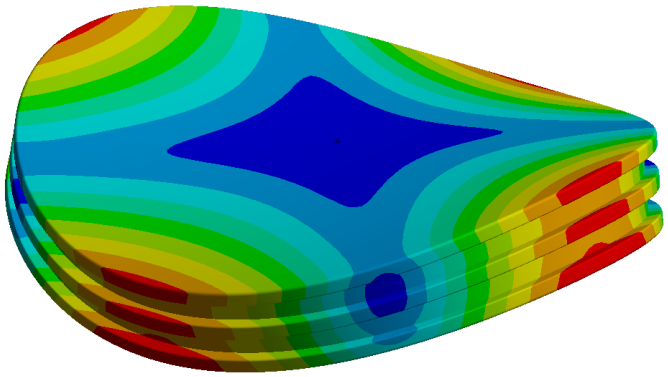

Figure 2.8: First non-rigid mode of the source piston as computed from ANSYS eigenfrequency analysis.

2.2.2.2 Compliance from O-ring

The compliance of the piston/shaker assembly was provided by an o-ring between the bottom of the piston and the lip on the annular plate. The o-ring is a Shore A durometer Buna-N rubber Parker 2-449 [35] and its dimensions were chosen so that they fit within the annular plate. The deflection as a function of load from the water on this o-ring was estimated by [36]

$$\frac{F}{\pi D d_{\mathrm{o}} E} = 1.25\delta^{3/2} + 50\delta^{6}, \tag{2.38}$$

where $\delta = \Delta d/d_{\mathrm{o}}$, Δd is the compression of the o-ring, d_{o} is the o-ring cross-section diameter, D is the o-ring mean diameter, F is the force applied to the o-ring, and E is the elastic modulus of the o-ring material. The elastic modulus of an elastomer can be estimated from the Shore A hardness $\mathrm{SH_A}$ by [37]

$$E = \frac{1-\nu^2}{2RC_3}\frac{C_1 + C_2\mathrm{SH_A}}{100 - \mathrm{SH_A}}(2.6 - 0.2\mathrm{SH_A})10^6, \tag{2.39}$$

where ν is the Poisson's ratio of the material, R is the radius of the indenter and is 0.395 mm, and C_1, C_2, and C_3 are constants and are equal to 0.549 N, 0.07516 N, and 0.025 mm, respectively. Solving Eq. (2.38) for the o-ring deflection Δd and relating that to the equation for a force on a spring, $F = -k_\mathrm{s}\Delta d$, allows one to estimate the stiffness of the o-ring and results in 2.9 kN/m. For completeness, the FEA result shown in Fig. 2.8 was repeated using an elastic boundary condition with the stiffness found from the above calculation. Since the results were very similar to that of the free edge computation, they are not presented here.

2.2.2.3 Shaker Selection

An inertial shaker was appropriate for the piston/shaker assembly since it attaches directly to the piston, does not require careful alignment between the piston and the shaker armature centers, and is isolated from the floor (since it does not require a base support). Trade studies of commercial off-the-shelf (COTS) inertial shakers showed that many manufacturers offer shakers designed to operate at their resonance frequency and not over a wide band of frequencies. The selected shaker was a Labworks Inc. FG-142 inertial shaker with an operating band spanning 20 to 3000 Hz [38].

As a first order approximation of the mechanical mass induced on the piston by the acoustic load, equivalent circuit elements for the radiation impedance of a plane piston into the end of a long tube as described by Beranek were used [39]. For values of $ka_\mathrm{p} < 0.5$, where k is the acoustical wave number and a_p is the piston radius, the acoustic mass in the mechanical mobility domain can be described as

$$M_M = 1.927 a_\mathrm{p}^3 \rho, \tag{2.40}$$

and has a value of 4.53 kg for this system. For completeness, it should be noted that ka_{p} at 2 kHz is 1.19, which is outside of the valid range for Eq. (2.40) but was determined to be a close enough approximation in order to estimate the parameters needed by the shaker. The mechanical mass of the piston was estimated from a PTC, Inc. Creo [40] CAD model and was found to be 4.53 kg. From these two masses, the shaker transfer function between output acceleration $\ddot{x}_{\mathrm{shaker}}$ and input voltage e_{in} was estimated from a Labworks Inc. equivalent circuit model and the results are shown in Fig. 2.9. Inspection of Fig. 2.9 reveals a large resonance at approximately 2 kHz. Manufacturing variances in the construction of this shaker could result in a shift in the resonance frequency and it was decided that in-band resonance of the shaker would be eliminated by reducing the mass of the piston if it was found to be problematic.

2.2.3 Isolation Systems

A mass-spring-damper isolation system was designed in order for the waveguide to be isolated from spurious noise sources from the laboratory floor. To this end, the waveguide was supported within a frame using compliant straps and rests on four air springs. Additionally, the reference hydrophone and DUT support structure is isolated from the linear actuator by a mass-spring-damper isolation system. Engineering drawings of the waveguide and sensor isolation systems can be seen in Appendices D.1 and D.5, respectively and Sec. 2.2.3.1 and Sec. 2.2.3.2 detail the designs for each isolation system.

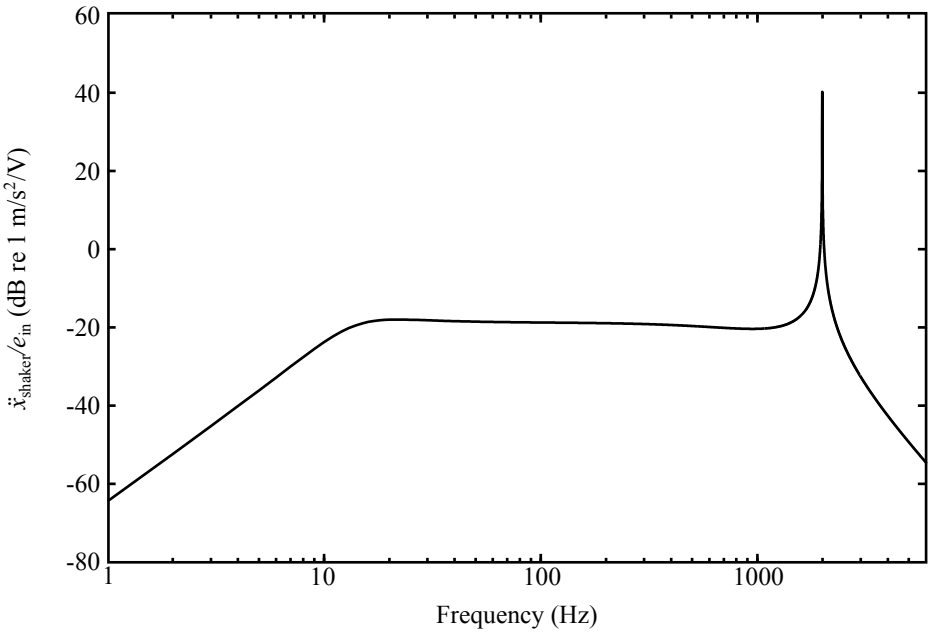

Figure 2.9: Predicted transfer function between shaker output acceleration and input voltage for a Labworks Inc. FG-142 inertial shaker.

2.2.3.1 Waveguide Isolation System

A mechanical model and the corresponding equivalent circuit model in the mechanical mobility domain, as seen in Figs. 2.10(a) and 2.10(b), respectively, were created to determine the appropriate spring compliance of the waveguide isolation system. The transfer function between the waveguide and floor velocities was computed from the equivalent circuit model

$$\frac{u_{\mathrm{wg}}}{u_{\mathrm{floor}}} = 1 - \frac{1}{1 + R_{\mathrm{m,sus}}/j\omega M_{\mathrm{wg}} - 1/\omega^2 C_{\mathrm{m,sus}} M_{\mathrm{wg}}}, \tag{2.41}$$

where u_{wg} and u_{floor} are the velocities of the waveguide and the floor, respectively, $R_{\mathrm{m,sus}}$ is the resistance of the suspension, M_{wg} is the water-filled waveguide mass, and $C_{\mathrm{m,sus}}$ is the compliance of the suspension. The waveguide mass with water

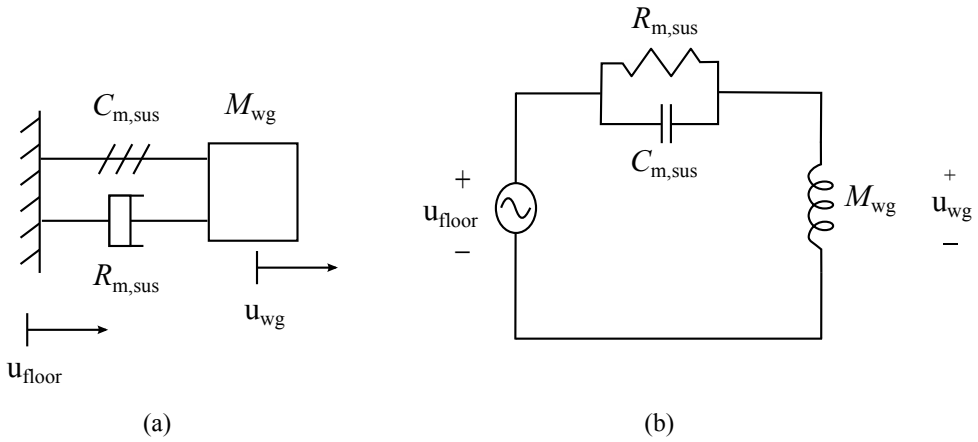

Figure 2.10: Waveguide isolation system: (a) mechanical model, (b) equivalent circuit model.

was estimated to be 1725 kg from the CAD model. The lowest usable frequency of the calibration system was determined by the source to be 20 Hz and it was desired to design a suspension system that would reject at least 90% of any spurious floor vibrations at and above this frequency. To this end, a transmissibility curve was generated from Eq. (2.41) where the waveguide isolation system compliance and resistance were provided by four Firestone 255-1.5 air springs in parallel where the air spring internal pressure was 60 psig [41]. Figure 2.11 shows that for light damping, 40 dB of velocity attenution is attainable at 20 Hz.

2.2.3.2 Sensor Isolation System

The reference hydrophone and DUT must be suspended in the water-filled waveguide and mechanically isolated from waveguide wall, support frame, and actuator vibrations to accurately perform calibration measurements. The apparatus required to suspend the transducers must be modular enough to allow

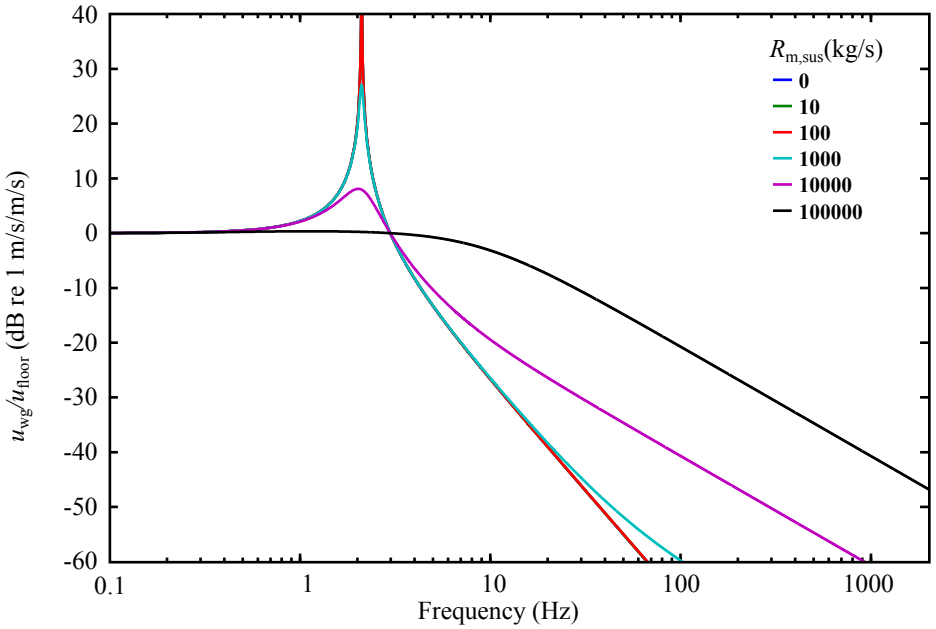

Figure 2.11: Predicted transmissibility curves of waveguide isolation system for a range of suspension mechanical resistances $R_{m,sus}$.

the operator to affix various sizes of transducers and to provide flexibility in the placement of a reference hydrophone. For the design of this system, the author found inspiration from microphone shock isolators frequently used in recording studios and an overview of this system is seen in Appendix D.5.

As with the waveguide isolation system, the sensor isolation system is also a mass-spring-damper system and is designed to be a mechanical low-pass filter where the frequency response can be predicted using an equivalent circuit model in the mechanical mobility domain. The resistive component, which is not shown in Appendix D.5, is comprised of craft stuffing adhered between the frame and the sensor isolation mass. The damping provided from the resistive element was tuned in order to make the isolation mass critically damped. The equivalent circuit

model for the sensor isolation system is identical to that of the waveguide isolation and is not repeated here. Similarly, the transfer function between the isolation frame velocity and the isolation mass velocity is

$$\frac{u_{\text{iso}}}{u_{\text{frame}}} = 1 - \frac{1}{1 + R_{\text{stuff}}/j\omega M_{\text{iso}} - 1/\omega^2 C_{\text{eqspring}} M_{\text{iso}}}, \tag{2.42}$$

where u_{iso} and u_{frame} are the velocities of the isolation mass and the frame, respectively, R_{stuff} is the resistance provided by the craft stuffing, M_{iso} is the mass of the isolation mass, and C_{eqspring} is the compliance of the combination of all springs in parallel. The mass of the isolation mass was estimated from the CAD model to be 11.25 kg and the equivalent stiffness of the springs was 620 N/m. For a critically damped system, the mechanical resistance can be determined from

$$R_{\text{m}} = 2\sqrt{1/C_{\text{eqspring}} M_{\text{iso}}}. \tag{2.43}$$

From these parameters, the transmissibility curve was computed and was found to provide 49 dB of attenuation at 20 Hz as seen in Fig. 2.12.

2.2.4 Three-Dimensional Finite Element Analysis of Waveguide

A three-dimensional sound-structure interaction finite element numerical model was created in COMSOL (a commercially available software package [40]), so that the effects of the waveguide structural modes on the acoustic pressure field within the waveguide were understood. The geometric model was designed in Creo and imported into COMSOL where the waveguide and welded flange, water, piston, annular plate, and stiffness of the spring isolators were modeled. Both structural displacement eigenfrequency and frequency-dependent acoustic pressure models were created and both models shared the same geometry, materials, and

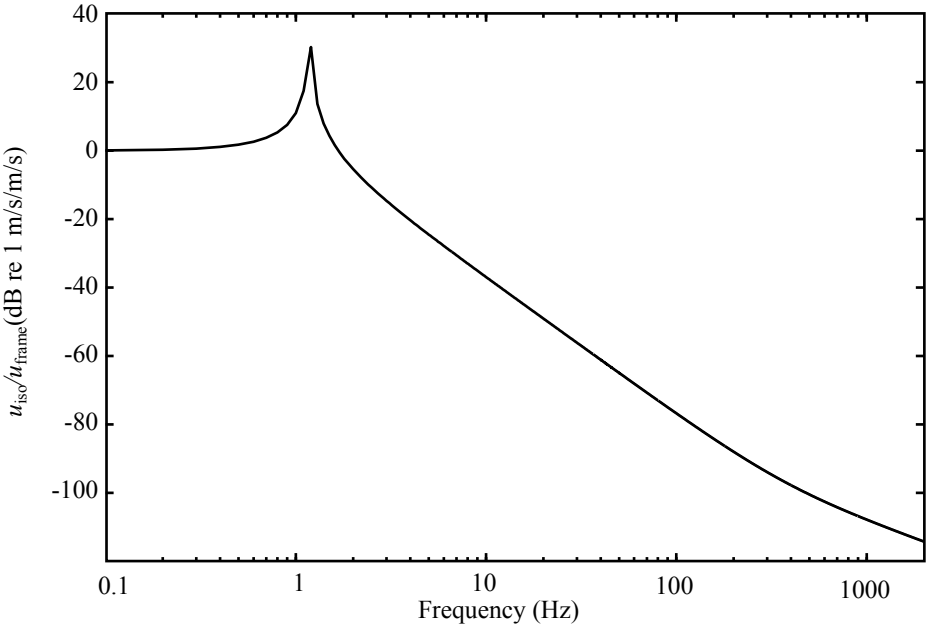

Figure 2.12: Predicted transmissibility curve for the sensor isolation system.

mesh. The eigenfrequency study allows the user to construct a fast and concise method of identifying all of the modal frequencies of the water-filled waveguide but the model was not constructed in a manner that would allow one to estimate the acoustic pressure field within the water. The eigenfrequency study estimated all modes within a frequency band regardless of whether or not the waveguide source condition would excite a particular mode. In the frequency-dependent acoustic pressure model, the waveguide was excited by prescribing an acceleration on the source piston through a user-specified frequency band and the acoustic field at each frequency was determined. The results of the eigenfrequency and frequency-dependent acoustic pressure models are described in Sec. 2.2.4.1 and Sec. 2.2.4.2, respectively.

2.2.4.1 Results of Eigenfrequency Analysis

The frequency band of the standing-wave apparatus was determined to be 20 Hz to 2 kHz from the previous analysis, therefore it was imperative that the structural modes be known throughout this frequency band. The results of this analysis predicted a number of mode shapes for a freely vibrating waveguide including those described as axial bending, axisymmetric, and circumferential. The eigenfrequencies and related mode shapes are listed in Table 2.4, four of the mode shapes are illustrated in Figs. 2.13(a)-2.13(d), and illustrations of all mode shapes predicted are presented in Appendix A.3.

2.2.4.2 Results of Frequency-Dependent Acoustic Pressure Analysis

The frequency-dependent acoustic pressure model investigated the effects of the waveguide structural modes on the acoustic field in the range of 20 to 2150 Hz in 5 Hz increments. The model prescribed a 1 m/s^2 frequency-independent acceleration on the base of the piston in order to ensonify the waveguide and a two-dimensional cross-section of the acoustic pressure field inside the waveguide computed by COMSOL was exported for post-processing in MATLAB. Since the piston acceleration in the COMSOL model is unity, the data are equivalent to the transfer function between acoustic pressure and source acceleration. A simple conversion from acceleration to velocity can be performed by multiplying the transfer function by $j\omega$ and the converted result as a function of depth in the waveguide and frequency is shown in Fig. 2.14. Comparison between Fig. 2.14 and Fig. 2.5 reveals features from potential structural modes of the waveguide at 555, 1080, and 1785 Hz. These frequencies do not correlate perfectly with the frequencies at which the eigenfrequency study predicted modes but these

Table 2.4: Eigenfrequencies and mode shapes of the waveguide as predicted by the COMSOL eigenfrequency model. Acoustic field disruptions were predicted by the COMSOL frequency-dependent acoustic pressure model.

Frequency (Hz)	mode shape	predicted to disrupt acoustic field
109	axial bending	no
282	axial bending	no
313	torsional	no
393	piston rocking	no
500	bending/circumferential	no
517	bending/circumferential	no
520	circumferential	no
524	circumferential	no
535	bending/circumferential	no
543	circumferential	no
581	circumferential	no
645	circumferential	no
651	circumferential	no
659	torsional/axisymmetric	no
733	circumferential	no
748	circumferential	no
761	circumferential	no
857	circumferential	no
1024	axisymmetric	no
1401	axisymmetric	no
1776	axisymmetric	yes

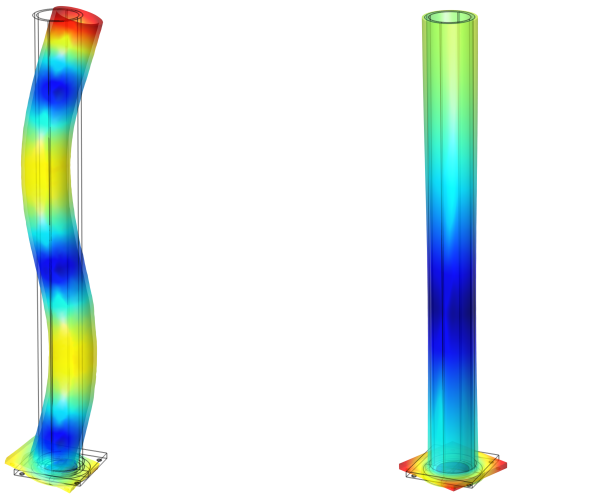

(a) 282 Hz bending mode.

(b) 313 Hz torsional mode.

(c) 543 Hz circumferential mode.

(d) 1776 Hz axisymmetric mode.

Figure 2.13: Illustration of four of the mode shapes of the water-filled waveguide as computed by the COMSOL eigenfrequency model.

discrepancies could be related to the difference in the frequency resolution between the two models and possibly compounded by the differences in the frequency response of the freely vibrating and driven waveguide. Also note that since a finite source distribution was used in the frequency-dependent acoustic pressure model, only a subset of the modes found in the eigenfrequency analysis will be excited.

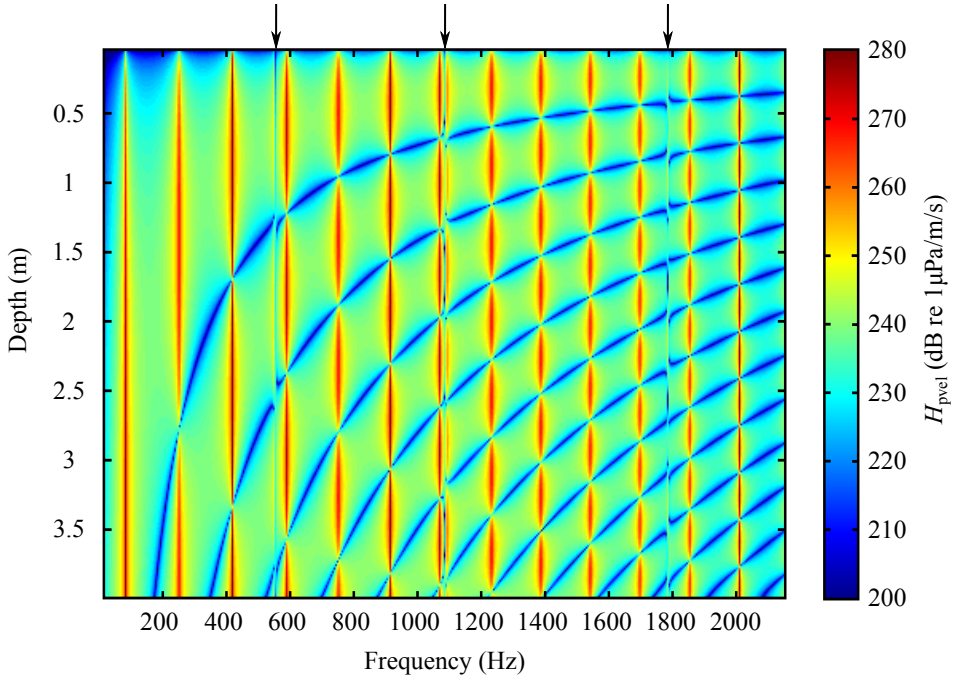

Figure 2.14: Predicted transfer function between acoustic pressure and piston velocity along the axis of revolution of the waveguide as determined from the COMSOL frequency-dependent acoustic pressure model. The arrows at the top of the figure highlight the predicted disruptions to the acoustic field at 555, 1080, and 1785 Hz.

In order to understand the radial particle velocity within the waveguide, the pressure gradient along the length and across the radius of the waveguide was computed numerically in MATLAB from the COMSOL two-dimensional pressure data using a five-point finite difference method. The ratio between the axial and

radial pressure gradients was then computed to visualize the relative importance of radial particle motion. The off-axis response of a vector sensor directional channel can be up to 40 dB lower than the on-axis response and, therefore, a threshold of 40 dB was used to find what eigenfrequencies of the waveguide disrupt the acoustic field enough to affect vector sensor calibrations. Figure 2.15 shows the results of the calculation of the ratio of axial pressure gradient to radial pressure gradient where Fig. 2.15(a) illustrates a frequency where there is at least 40 dB between the axial and radial pressure gradients in the region where calibration measurements are performed. Calibration measurements at this frequency should produce valid results since the volume of the maroon-colored region near the air/water interface encompasses both the reference hydrophone and a 0.1 m diameter DUT. However, Figs. 2.15(b)-2.15(e) illustrate four frequencies where calibrations will likely produce inaccurate results due to high radial pressure gradients and, therefore, non-planar wavefronts near the air/water interface. Non-planar wavefronts can lead to errors in calibration measurements since the acoustic pressure at the reference hydrophone and DUT will not be the same due to the radial offset between the two devices.

2.2.5 Reference Hydrophone, Sensor Positioning, and Data Collection Systems

All data acquisition from the waveguide is automated by a PC-based LabVIEW [42] software program. The software was designed so that the operator enters the desired test parameters, places all sensors in the desired orientation and location, and initiates the test. The software then sends the test parameters to a four-channel Agilent 35670A signal analyzer [43] and waits until the signal analyzer has completed the measurement. Once the measurement is finalized, the data are

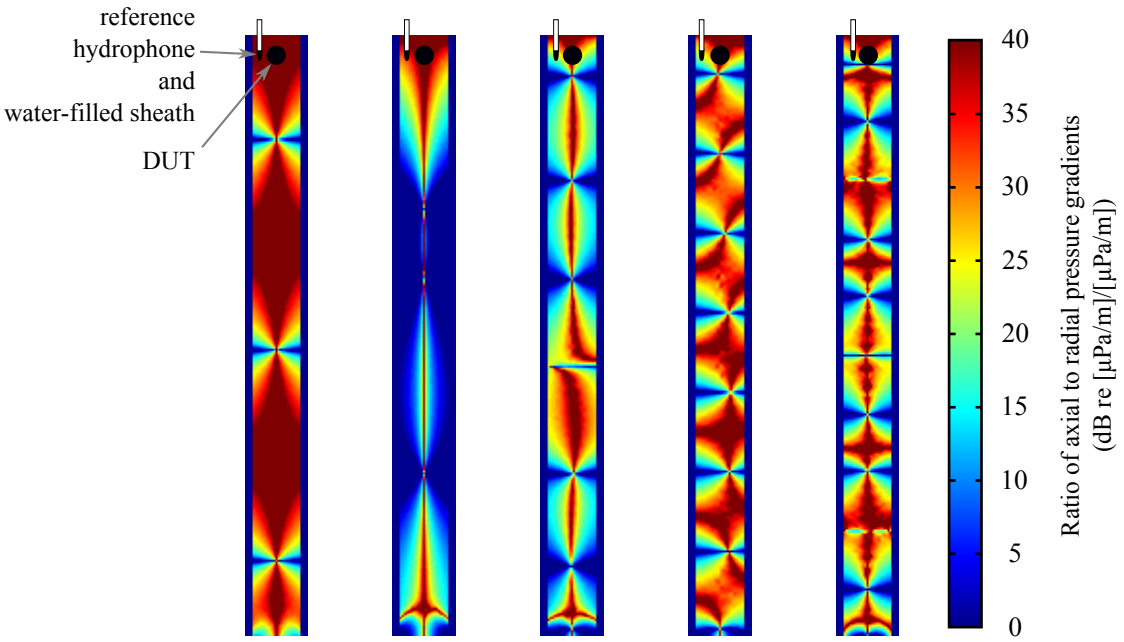

(a) 500 Hz (b) 555 Hz (c) 1085 Hz (d) 1315 Hz (e) 1780 Hz

Figure 2.15: Ratio of axial pressure gradient to radial pressure gradient computed from COMSOL frequency-dependent acoustic pressure model. (a) Frequency at which calibrations will likely produce valid results. (b)-(e) Frequencies at which calibrations may not produce valid results.

transferred to the PC through a general purpose interface bus (GPIB) and are stored for post-processing. The signal analyzer is used to generate the source signal, collect the time series data, and process the time series data into the frequency domain. Sections 2.2.5.1, 2.2.5.2, and 2.2.5.3 detail the design and selection of the reference hydrophone, sensor positioning system, and data collection system, respectively.

2.2.5.1 Reference Hydrophone

Data collection for both DUT calibration measurements and waveguide characterization testing required the use of a small, omnidirectional hydrophone in order to quantify the acoustic field with minimal disruption. The reference hydrophone, shown in Fig. 2.16, is a Teledyne RESON TC4013 omnidirectional hydrophone with a EC6067 conditioning charge amplifier [14, 44]. This transducer was chosen for the reference hydrophone because of its small size (9.5 mm diameter by 25 mm length) and use in previous literature [15, 45]. A water-filled stainless steel sheath was used to house the hydrophone cable to reduce its interaction with the acoustic field and to accurately position the sensor. Two TC4013 hydrophones and preamps were purchased for the system where each hydrophone/preamp combination was calibrated in the waveguide to a NUWC H52 reference hydrophone [46] and was marked to ensure only the calibrated hydrophone/preamp pair is used in subsequent measurements.

2.2.5.2 Sensor Positioning System

As mentioned in Sec. 2.2.3.2, the reference hydrophone and DUT are suspended from the sensor isolation system. The depth of the sensors is controlled using a Parker ERV5 series linear actuator [47] that is mounted to a support frame that rests above the waveguide and a schematic of this assembly is shown in Appendix D.1. A stepper motor provides the motion of the linear actuator and the stepper motor, motor controller, and linear actuator were specified and the motion-control software was written by SISU Devices [48] for the author. Initial testing of the apparatus showed that electromagnetic interference (EMI) produced by the stepper motor controller was capable of corrupting acoustic measurements

and so an Inertia Dynamics MPC power-off brake [49] was installed so that the controller could be placed in a disabled mode during measurements without the carriage on the linear actuator moving due to the weight of the sensor isolation system.

2.2.5.3 Data Collection System

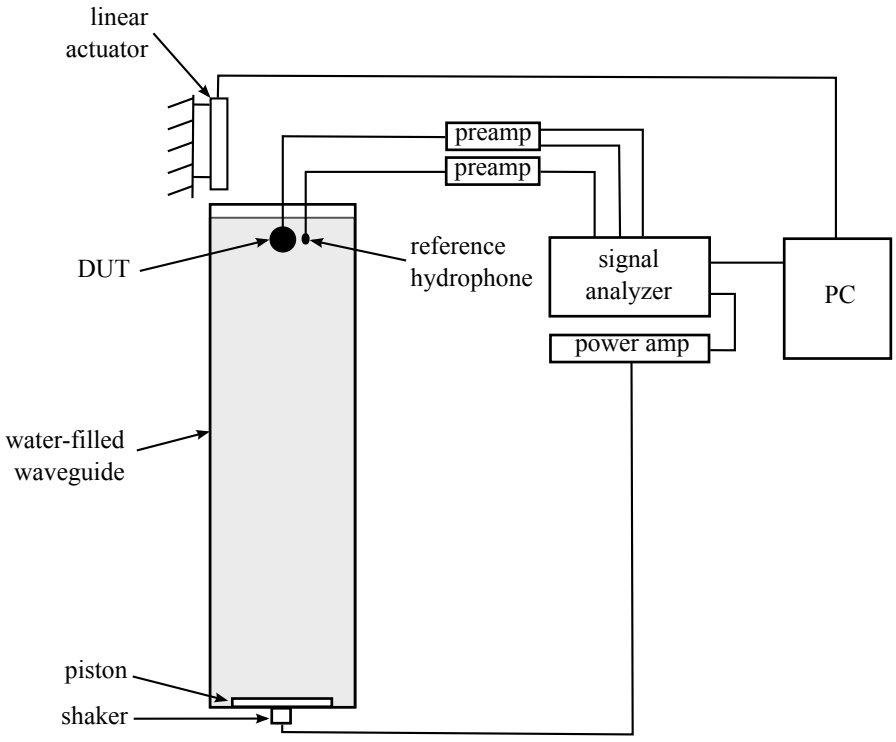

Figure 2.16: Schematic diagram of the data collection system.

The data collection system is comprised of the reference hydrophone and DUT including any preamps, Agilent 35670A signal analyzer, linear actuator, and a PC loaded with the LabVIEW control software. A schematic of the data collection system set up for calibration measurements is shown in Fig. 2.16.

The LabVIEW control graphical user interface (GUI) was designed so that the operator could easily set up and document test parameters and notes. Test set up parameters include

- source signal type and amplitude
- frequency band and resolution
- depth of water in waveguide
- percent dissolved oxygen content in water
- sensor depths and number of depth positions (used for waveguide characterization measurements)
- sensor types, sensitivities, and gain for each channel
- voltage range for analog to digital converter (ADC) on signal analyzer.

All parameters are recorded for post-processing and for reference at a later date.

A "jog motor" subpanel of the data collection system allows the operator to move the linear stage in a very precise and controllable manner. This allows one to accurately orient and position the acoustic centers of the reference hydrophone and the DUT at the air/water interface before lowering the sensors to the test depth desired by the operator. The operator can create a "home" position of the sensors at either the air/water interface or at the test depth and these metadata are stored along with the acoustic data from the subsequent measurement. The main, jog motor, and ADC voltage range GUIs can be seen in Figs. B.1, B.2, and B.3 in Appendix B, respectively.

Chapter 3

Apparatus Characterization

System characterization measurements were taken once the standing-wave apparatus was built and assembled. This chapter is organized in a manner to describe each set of measurements where Sec. 3.1 describes the determination of an appropriate apparatus stimulus signal, Sec. 3.2 details the process used to bring the water-filled waveguide to an equilibrium state, Sec. 3.3 presents the results of waveguide phase velocity measurements, Sec. 3.4 discusses the measured acoustic fields within the waveguide, Sec. 3.5 delineates the measurements to ensure that the wavefronts are sufficiently planar for calibration measurements, Sec. 3.6 details the measurements to determine the effectiveness of the waveguide and sensor isolation systems, Sec. 3.7 describes the measurements to ensure that the piston does not support structural modes in the operating frequency band, and Sec. 3.8 identifies the structural modes that disrupt the acoustic field within the waveguide.

3.1 Determination of Apparatus Stimulus Signal

The Agilent 35670A dynamic signal analyzer is used to generate the apparatus stimulus signal and allows the user to choose from numerous source signal types including: band-limited white noise, linear and logarithmic periodic chirps, burst chirp, single-frequency sine wave, and swept-sine. It is up to the user to determine the appropriate method based on system linearity and time to reach

steady-state [50]. Each signal type provides benefits for various system measurement needs. This thesis will describe two measurement/processing types used to characterize the apparatus: periodic chirps processed using a Fast Fourier Transform (FFT) and swept-sine measurements.

In order to take advantage of fast measurement times, the first stimulus signal type used for the apparatus characterization measurements was the periodic chirp. During this testing, it was found that the displacement of the reaction mass of the inertial shaker was high enough to hit the stops below 25 Hz when exciting the system using the peak excitation voltage allowed by the shaker, therefore the lowest excitation frequency was set at 25 Hz. The period chirp frequency band was 25 to 1625 Hz, due to the number of record lines of the signal analyzer, and the measurement was averaged 20 times with no windowing. The ambient noise measurement was taken by repeating the periodic chirp measurement only with the source amplifier turned off. Next, the waveguide was ensonified using a swept-sine signal with the same input signal amplitude as for the periodic chirp where the test frequency band was 25 to 2000 Hz. The measurement was repeated with the source amplifier turned off in order to record the ambient noise. The spectral levels of both the ensonified and quiet measurements at a depth of 0.5 m below the air/water interface was computed and are shown in Fig. 3.1.

From Fig. 3.1, the dynamic range of the spectral levels in the standing-wave field is the same for the both the swept-sine and periodic chirp measurements, which indicated that the sweep rate of the periodic chirp was slow enough to allow the apparatus to reach steady-state. Additionally, the SNR for both measurement types is at least 10 dB throughout the test frequency band where, as discussed in

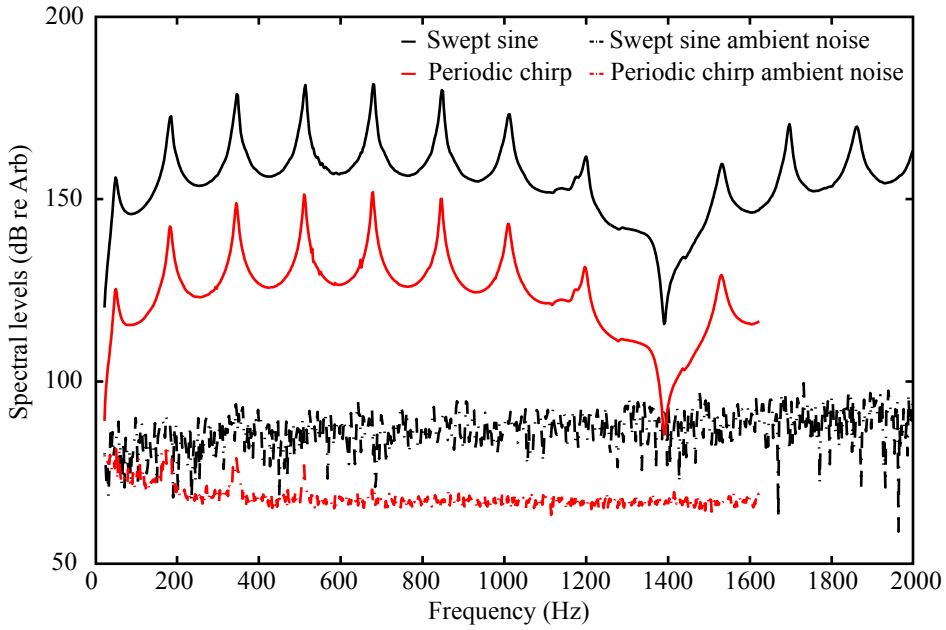

Figure 3.1: Comparison of the spectral levels measured in the waveguide using swept-sine and periodic chirp stimuli.

Sec. 4.2, this value is used as the SNR threshold in post-processing calibration measurements. While the standing-wave apparatus reached steady-state using periodic chirps, the swept-sine measurement type was chosen for most subsequent system characterization measurements and for all calibration measurements presented in this thesis since it avoids the high transients found in periodic chirps.

3.2 Methodology for Obtaining a Repeatable Acoustic Field

The water in the waveguide is drained when not in use to reduce corrosion. Once the waveguide is filled with tap water, it is desired that acoustic field within the waveguide be repeatable and time-invariant for up to five consecutive days.

To accomplish this, the dissolved oxygen content of the water must be minimized, the water must come to thermal equilibrium with the waveguide, and the water level in the waveguide must remain constant.

Degassing the water (which removes existing bubbles and prevents formation of new bubbles) in the waveguide is accomplished by sealing the top and bottom ends of the waveguide and evacuating the air via a vacuum pump. A vacuum is also required at the bottom of the waveguide since the water column is not deep enough to maintain positive gage pressure above the piston when a vacuum exists above the waterline and should be applied prior to evacuating the air above the waterline. Testing revealed that holding a vacuum of at least 27 mm Hg for 30 minutes while continuously mixing the water using a submersible pump consistently reduced the dissolved oxygen content from approximately 85% to roughly 40% of full saturation which then could be maintained for up to five days. A schematic of the degassing hardware can be found in Appendix D.7.

In addition to degassing, the water must be allowed to come to thermal equilibrium with the waveguide to produce a repeatable acoustic field. It was found that the time to reach thermal equilibrium varies throughout the year where during the summer months, the water is typically very close to room temperature as it flows from the spigot, but can take several hours for the water to reach thermal equilibrium with the waveguide during the winter. Additionally, a significant temperature gradient exists in the laboratory during the late summer months. The temperature at the bottom and top of the waveguide were measured to be 25.6 and 29.7° C, respectively. The speed of sound in pure water at these temperatures are 1498 and 1508 m/s, respectively, which is a difference of 0.7% and therefore

the effect of the temperature gradient on the phase velocity was ignored.

As a rule of thumb, the process of changing the water in the waveguide is: pump the water out of the waveguide using a submersible pump, refill the waveguide with tap water, cover the waveguide and hold a vacuum of at least 27 mm Hg for at least 30 minutes, release the vacuum, remove the sealing plates, and let the water sit overnight. This process brings the water in the waveguide to a repeatable state for up to five days at any point in the year. Lastly, evaporation at the air/water interface reduces the water level over time. Consequently the water level should be carefully measured and reset daily during testing.

3.3 Phase Velocity Measurements

Frequency-dependent phase velocity measurements were made after the system was degassed and allowed to reach a thermal equilibrium temperature of 26.4° C. These measurements were accomplished by placing the acoustic center of a Teledyne RESON TC4013 hydrophone at 2.000 m $\pm$ 0.002 m below the air/water interface without a cable sheath and exciting the piston using a single-frequency, single-cycle tone burst in the range of 400 to 2000 Hz in 100 Hz increments and capturing the first and second arrivals of the acoustic pressure signal. The first arrival of the signal traveled from the source at the bottom of the waveguide and the second arrival was caused by the reflection of the first signal arrival from the air/water interface. For this measurement, the low frequency limit of 400 Hz was determined by the acoustic wavelength short enough to be resolved at the test depth. The acoustic signals from the hydrophone were recorded using a Tektronics TDS2004C digital oscilloscope [51] and the data were downloaded to a PC and

post-processed in MATLAB by manually identifying the first and second arrivals, inverting and cross-correlating the second arrival with the first arrival in order to find the lag time $\tau(\omega)$ between the two pulses, and finally computing the frequency-dependent phase velocity $c^{\text{ph}}_{\text{measured}} = 2d/\tau(\omega)$ where d was the distance of the hydrophone below the air/water interface. For completeness, the diameter of the waveguide and the low frequencies at which it operates does not require a hydrophone cable sheath to prevent disruptions to the acoustic field within the waveguide that has been necessary for smaller diameter, higher frequency waveguides in previous literature.

The sampling frequency of the oscilloscope was 250 kHz which translated to a period of 4 μs between samples. As mentioned in the preceding paragraph, the resolution to which d could be measured was $\pm$ 0.002 m. The uncertainty arising from both the temporal and spatial resolution of the measurement was computed and is displayed as error bars in Fig. 3.2. The result of the phase velocity measurement is within 1% of that predicted by the Lafleur and Shields algorithm for a water/waveguide temperature of 26.4° C.

3.4 Acoustic Pressure Field Measurements

Acoustic pressure measurements were made in order to verify the estimates of the acoustic pressure fields detailed in Sec. 2.2.1.2. For this measurement, a Teledyne RESON TC4013 hydrophone was suspended under the sensor isolation mass by a water-filled stainless steel sheath (with an outside diameter and wall thickness of 9.5 and 1.2 mm, respectively) and was scanned along the waveguide axis of revolution, the waveguide was ensonified using the peak excitation voltage

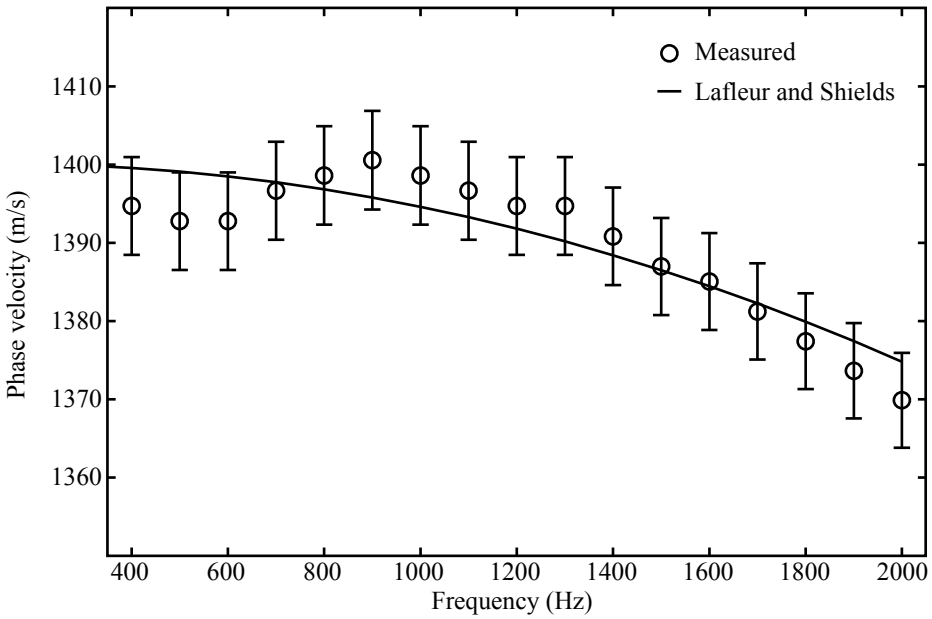

Figure 3.2: Comparison of measured phase velocity to that predicted by the Lafleur and Shields algorithm.

allowed by the shaker, and the acoustic pressure was recorded throughout a frequency band from 25 to 2000 Hz at each depth ranging from 0 to 1500 mm in 5 mm increments. The piston velocity was measured using a Polytec OFV-505 single point last doppler vibrometer (LDV) with OFV-5000 controller [52] and was recorded simultaneously with the acoustic pressure at a single point on the piston that is representative of the spatially averaged piston velocity. The transfer function between the measured acoustic pressure and piston velocity $H_{\text{pvel,meas}}$ was computed as a function of hydrophone depth and frequency and the results are shown in Fig. 3.3.

Careful inspection of Fig. 3.3 and Fig. 3.4 revealed disruptions in the acoustic pressure field at 536, 543, 555, 565, 575, 1208, and 1733 Hz. Several of

these frequencies had been identified from the COMSOL eigenfrequency model as structural modes of the waveguide in Table. 2.4 and the COMSOL frequency-dependent acoustic pressure model seen in Fig. 2.15.

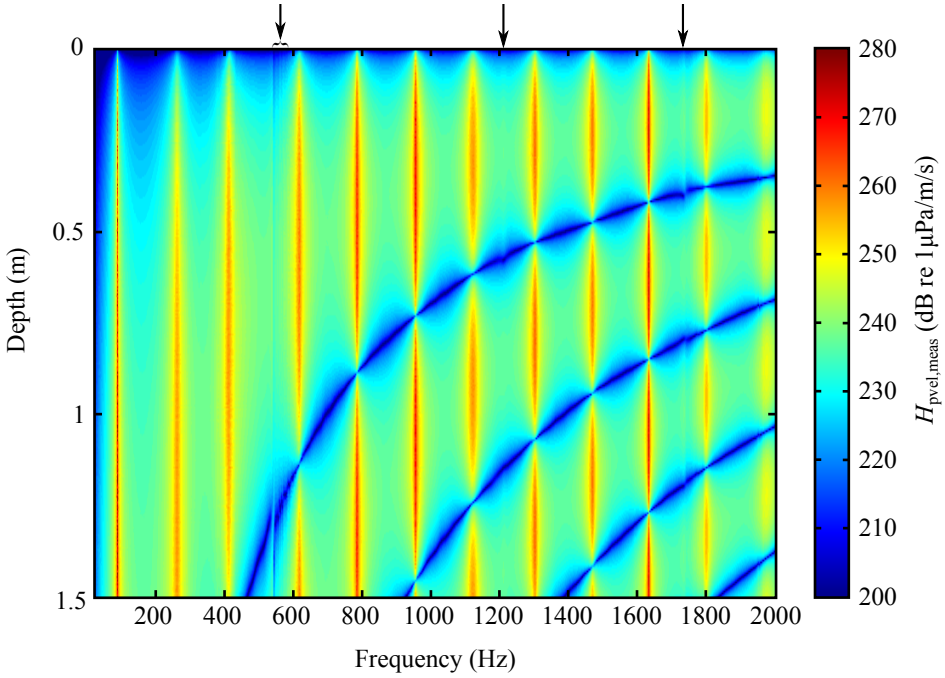

Figure 3.3: Transfer function between the measured SPL along the waveguide axis of revolution and piston velocity. The arrows at the top of the figure highlight the disruptions to the acoustic field in a frequency band from 536 to 580 Hz, 1208, and 1733 Hz.

Since the image plots of the transfer function between the acoustic pressure and piston velocity seen in Figs. 2.5 and 3.3 are not conducive for comparisons made on the same figure, Fig. 3.4 was created to illustrate the agreement between the predicted transfer function H_{pvel} described by Eq. (2.33) and the measured transfer function $H_{\text{pvel,meas}}$ at a depth of 0.500 m below the air/water interface. With the exception of the discrepancies seen between 536 and 580 Hz, 1208, and 1733 Hz, $H_{\text{pvel,meas}}$ and H_{pvel} agree very well. Additionally, H_{pvel} does not capture

the effects of attenuation via mechanisms other than viscous losses between the water and the waveguide walls at the acoustic resonance frequencies but the agreement between the measurement and the model was deemed sufficient, and hence these losses were ignored.

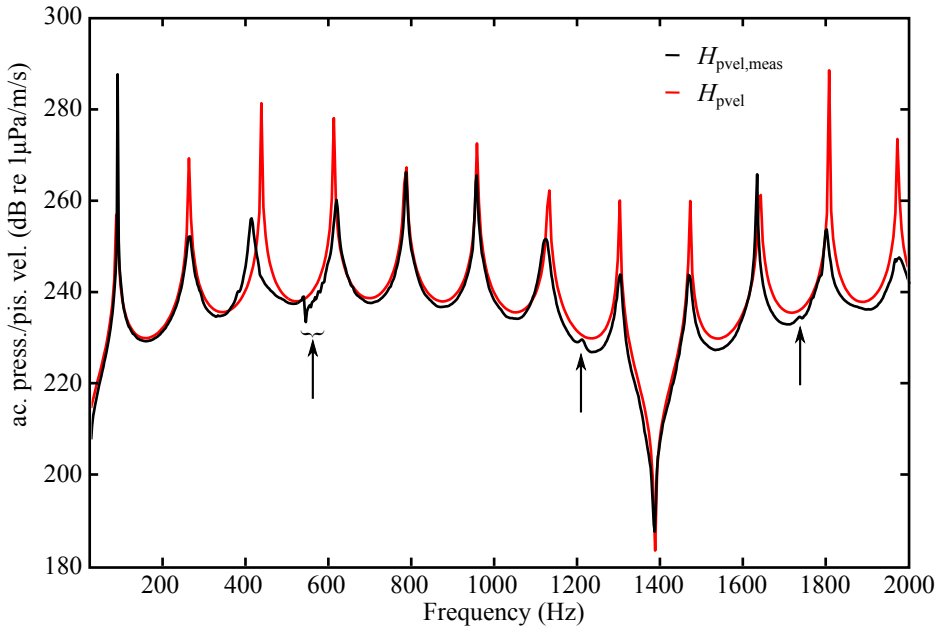

Figure 3.4: Comparison of measured and predicted transfer function between acoustic pressure and piston velocity along the waveguide axis of revolution 0.500 m below the air/water interface. The arrows in the figure highlight the disruptions to the acoustic field in a frequency band from 536 to 580 Hz, 1208, and 1733 Hz.

The levels of the acoustic pressure and pressure gradient fields from the same measurement as presented in Fig. 3.3 were processed in order to determine the peak acoustic pressure levels capable in the standing-wave apparatus and to verify the locations of pressure and pressure gradient nulls. The axial pressure gradient was determined from the measured data by computing the spatial derivative along

the axis of revolution using the same five-point finite difference algorithm as used to compute the axial and radial pressure gradients presented in Fig. 2.15. The measured SPL and computed pressure gradient are shown in Figs. 3.5(a) and (b), respectively, where the dashed lines in both figures illustrate the region where calibration measurements are made, 0.025 to 0.125 m below the air/water interface. Figure 3.5(a) shows the lowest acoustic resonance frequency in the waveguide occurs at 54 Hz and the remaining axial resonance frequencies are spaced approximately 164 Hz apart. The SPL range for the depths and frequencies measured spans 88 to 181 dB re 1 μPa. In the region where calibration measurements will be made, the SPL varies between 88 and 174 dB re 1 μPa. Figure 3.5(b) shows the locations of nulls in the pressure gradient field near the air/water interface and confirms the resulting depth limitation for calibration measurements as determined in Sec. 2.2.1.2.

3.5 Planar Wave Front Measurement

Significant efforts were made in the design of the waveguide to reduce the amplitude of radial particle motion of the ET0 mode to maximize the degree of wavefront planarity. A measurement of the degree of wavefront planarity was achieved by ensonifying the waveguide and recording the acoustic pressure while scanning a Teledyne RESON TC4013 hydrophone parallel to the axis of revolution of the waveguide between depths of 0.025 to 0.125 m in 0.010 m increments at 13 discrete positions across the inner diameter of the waveguide in 0.025 m increments. The order in which the radial positions were scanned was randomized in order to mitigate any time-dependent effects on the measured acoustic field. The data were

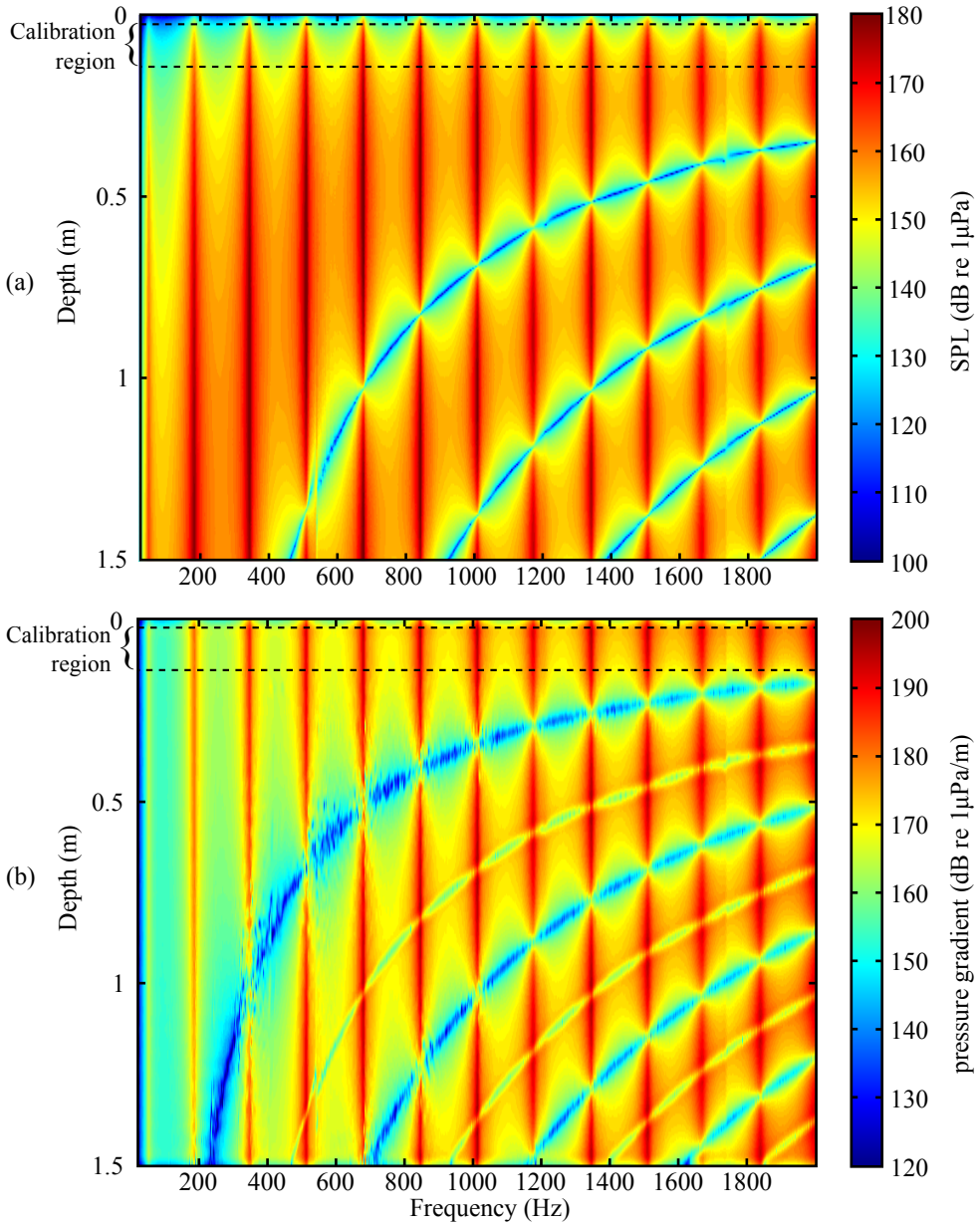

Figure 3.5: (a) Measured sound pressure level along the axis of revolution as a function of depth and frequency. (b) Axial pressure gradient computed from measured sound pressure level as a function of depth and frequency. The region where calibration measurements are performed is shown between the dotted lines

recorded using an Agilent 35670A signal analyzer and downloaded to a PC for post-processing in MATLAB.

The resulting data were processed by normalizing the measured acoustic pressure at each radial position, depth, and frequency, $p_{\text{meas}}(r, d, \omega)$, by the incoherently averaged pressure across the diameter for each depth and frequency, $\bar{p}_{\text{dia}}(d, \omega)$, as

$$p_{\text{norm}}(r, d, \omega) = \frac{p_{\text{meas}}(r, d, \omega)}{\bar{p}_{dia}(d, \omega)}, \tag{3.1}$$

where

$$\bar{p}_{\text{dia}}(d, \omega) = \sum_{n=1}^{N} \frac{|p_{\text{meas}}(r_n, d, \omega)|}{N}, \tag{3.2}$$

and the results for selected frequencies are shown in Fig. 3.6. For most frequencies, the measured wavefront was planar to within 1 dB. The plots between 536 and 580 Hz show a band of frequencies that are highly non-planar and are presumed to be caused by structural modes of the waveguide walls. Therefore, the frequency band spanning 536 to 580 Hz will be omitted from the reported calibration measurements. The figures above 1600 Hz show the effects of increased radial particle velocity on the wavefront but the variation was on the order of less than 1 dB across the waveguide inner diameter and, therefore, was found to be suitable for calibration measurements up to 2 kHz.

The normalized acoustic pressure from Eq. (3.1) was found to be consistent, for most frequencies, as a function of the depths measured therefore $p_{\text{norm}}(r, d, \omega)$ was incoherently averaged across all measured depths so that the data could be reduced to three dimensions to create the image plot shown in Fig. 3.7. Figure 3.7 illustrates that the wavefronts are planar within 1 dB for most frequencies and

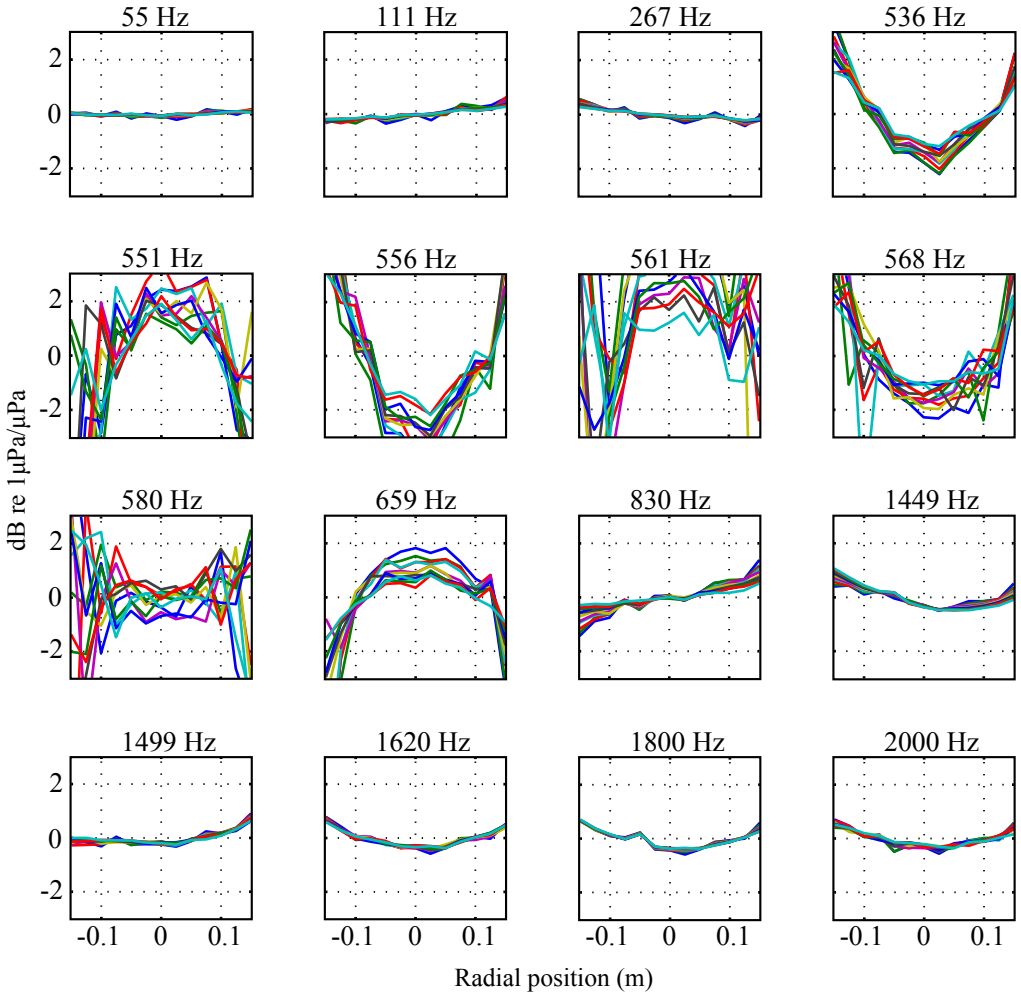

Figure 3.6: Acoustic pressure as a function of radial position and depth normalized by mean acoustic pressure across the inner diameter of the waveguide, p_{norm}. The various lines in each subplot represent a single depth in the waveguide.

radial positions measured where those whose wavefronts fall outside the $\pm$ 1 dB range are visually masked in black.

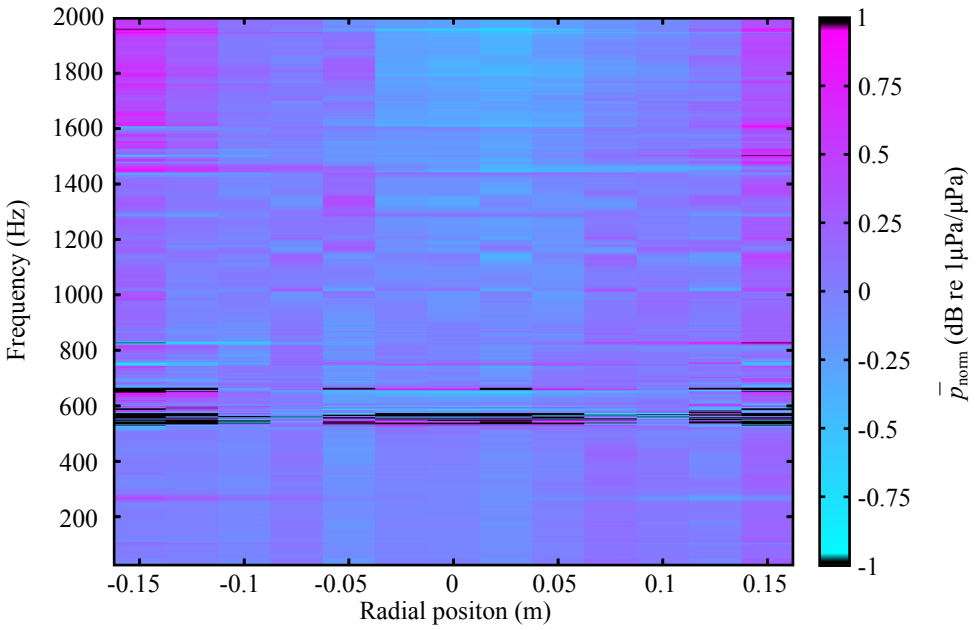

Figure 3.7: Normalized acoustic pressure as a function of radius averaged across depths spanning 0.025 to 0.125 m.

3.6 Vibration Isolation Testing

Measurements were performed to verify the effectiveness of the waveguide and sensor isolation systems. For these measurements, calibrated velocimeters were placed on the waveguide or sensor isolation mass where the waveguide isolation system was manually excited and the sensor isolation system was excited with a moving-coil shaker. Sections 3.6.1 and 3.6.2 discuss these measurements and the results of the waveguide and sensor isolation systems testing, respectively.

3.6.1 Waveguide Isolation System Measurements

The waveguide isolation system as described in Sec. 2.2.3.1 is a low-pass mechanical filter created from a mass-spring-damper system. In the design phase

of this isolation system, both the mass of the water-filled waveguide and the compliance of the air springs were estimated but the resistance produced by the viscoelastic effects of the air springs was unknown. The predicted transmissibility curves in Fig. 2.11 show a range of values for the mechanical resistance and their effect on vibration attenuation as a function of frequency. Several attempts were made to measure the transmissibility of the waveguide isolation system by exciting the waveguide using an eccentrically-loaded Vibco SCR-1000 shaker [53] in a frequency band spanning 2 to 20 Hz while measuring the waveguide and waveguide support frame velocities using the calibrated velocimeters. These attempts failed to produce meaningful results because the transverse vibrational modes were also excited by the shaker. Then, a Labworks Inc. ET-126HF moving-coil shaker was employed in an attempt to excite modes only along the axis of revolution of the waveguide. However, this shaker did not provide adequate SNR on the velocimeters.

Since attempts to measure the transmissibility of the waveguide isolation system by driving the system failed to produce meaningful results, the isolation system was instead excited by pushing lightly once on the base of the waveguide by hand and recording the response of a velocimeter mounted to the welded flange at the lower end of the waveguide using a Tektronix TDS2004C digital oscilloscope. The time-series data were downloaded onto a PC and post-processed in MATLAB using the log-decrement method to determine both the resonance frequency of the isolation system and the mechanical resistance provided by the air springs.

The log decrement method can be used to find the damping ratio of under-damped, unforced systems in the time domain where the damping ratio can be used

to find the mechanical resistance. The damping ratio ζ of a mass-spring-damper system is defined as

$$\zeta = \frac{R_{\mathrm{m}}}{R_{\mathrm{c}}}, \tag{3.3}$$

where R_{m} is the mechanical resistance of the system and R_{c} is the mechanical resistance for a critically damped system with the same mass and spring stiffness and is

$$R_{\mathrm{c}} = 2M_{\mathrm{mech}}\omega_0, \tag{3.4}$$

where M_{mech} is the mechanical mass and ω_0 is the natural frequency of the undamped system. The log decrement method from Ref. [54] is

$$\ln\left(\frac{x(t)}{x(t)+nT}\right) = \frac{2\pi n\zeta}{\sqrt{1-\zeta^2}}, \tag{3.5}$$

where $x(t)$ is the signal amplitude at time t, T is the period of one cycle of the under-damped signal, and n is an integer from 1 to ∞. Equation (3.5) can be simplified by neglecting the ζ^2 term on the right-hand side and can be recast as

$$\zeta \approx \frac{1}{2\pi n}\ln\left(\frac{x(t)}{x(t)+nT}\right), \tag{3.6}$$

and is valid for $\zeta < 0.2$. Figure 3.8 shows the measured waveguide velocity as a function of time where the highlighted maximum at 3.51 seconds was used as $x(t)$ in Eq. (3.6) and the damping ratio was computed between this point and each successive highlighted maxima to 11.26 seconds. The mean value for the damping ratio of the waveguide isolation system $\zeta_{\mathrm{m,sus}}$ was 0.0091 with a standard deviation of 0.00045.

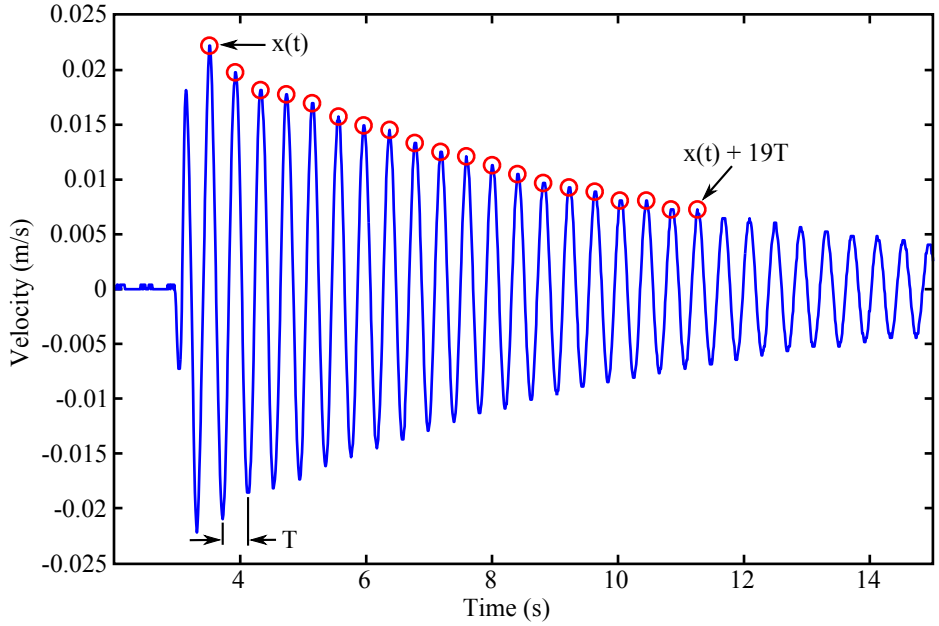

Figure 3.8: Time series of waveguide velocity used to compute the damping ratio of the air springs using the log decrement method.

Equations (3.3) and (3.4) were combined with the expression for the undamped natural frequency of a damped system

$$\omega_0 = \frac{\omega_\mathrm{d}}{\sqrt{1-\zeta^2}}, \tag{3.7}$$

where ω_d is the natural frequency of the damped system and were recast to find the expression for the mechanical resistance of the waveguide isolation system as

$$R_\mathrm{m,sus} = 2\zeta_\mathrm{m,sus} M_\mathrm{wg} \frac{\omega_\mathrm{d}}{\sqrt{1-\zeta^2}}, \tag{3.8}$$

where the natural frequency of the damped system can be found from the reciprocal of the period T from the time-series data and is 2.45 Hz. From Eq. (3.8), the mechanical resistance of the waveguide isolation system is estimated to be 483

kg/s and, therefore, the transmissibility of the waveguide isolation system was estimated to follow the curve in Fig. 2.11 for $R_{\mathrm{m,sus}} = 1000$ kg/s.

3.6.2 Sensor Isolation System Measurements

The transmissibility of the sensor isolation system described in Sec. 2.2.3.2 was measured using a Labworks Inc. ET-126HF shaker attached to the corner of the sensor isolation frame shown in Fig. 3.9 where a calibrated Wilcoxon Research 793V-5 velocimeter [55] was attached to the center of the sensor isolation mass and a Wilcoxon Research 786A accelerometer was attached at four equally-spaced points around the perimeter of the sensor isolation frame. Each Wilcoxon Research sensor utilized a Wilcoxon Research P702B power unit/amplifier that includes an user-selectable integrator circuit by which the accelerometer signal was integrated to be proportional to velocity. The sensor isolation frame was excited using a periodic chirp in a frequency band from 1 to 51 Hz and the transfer function between the two sensors was recorded by an Agilent 35670A signal analyzer. The data were then downloaded to a PC and post-processed using MATLAB. The frequency band of this measurement was limited to 51 Hz since the structural modal density of the sensor isolation frame was very high above this limit. Figure 3.10 shows the results of this measurement where the resonance frequency of the mass-spring-damper system is approximately 7 Hz, which is higher than what was predicted in the transmissibility curve in Fig. 2.12. Regardless, the sensor isolation system provided 23.6 dB of velocity attenuation at 25 Hz which was deemed sufficient for calibration measurements. The vertical gray line at approximately 5 Hz in Fig. 3.10 illustrates the frequency at which the coherence falls below 0.95 and data at frequencies below this line are prone to measurement error.

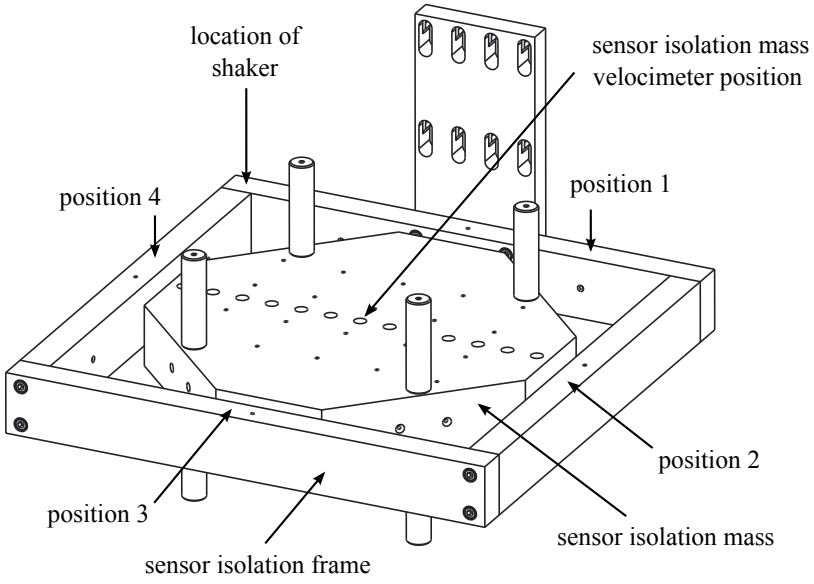

Figure 3.9: Simplified image of the sensor isolation system highlighting the locations of the shaker and velocimeters. Positions 1 to 4 show the measurement locations of the frame velocity.

3.7 Measured Piston Modes

Measurements to verify that the source piston does not support structural modes in the apparatus design frequency band and to attempt to verify the ANSYS FEA eigenfrequency model were performed *in situ* at frequencies between 25 and 2500 Hz using a Polytec OFV-505 single point LDV with an OFV-5000 controller. Figure 3.11(a) illustrates the measurement setup where the laser head rested on the laboratory floor and the laser beam was positioned on the back side of the piston using a mirror tilted at a 45° angle. A grid pattern similar to what is shown in Fig. 3.11(b) was sketched onto the backside of the piston where the mirror and laser head were repositioned on a point on the grid between each measurement,

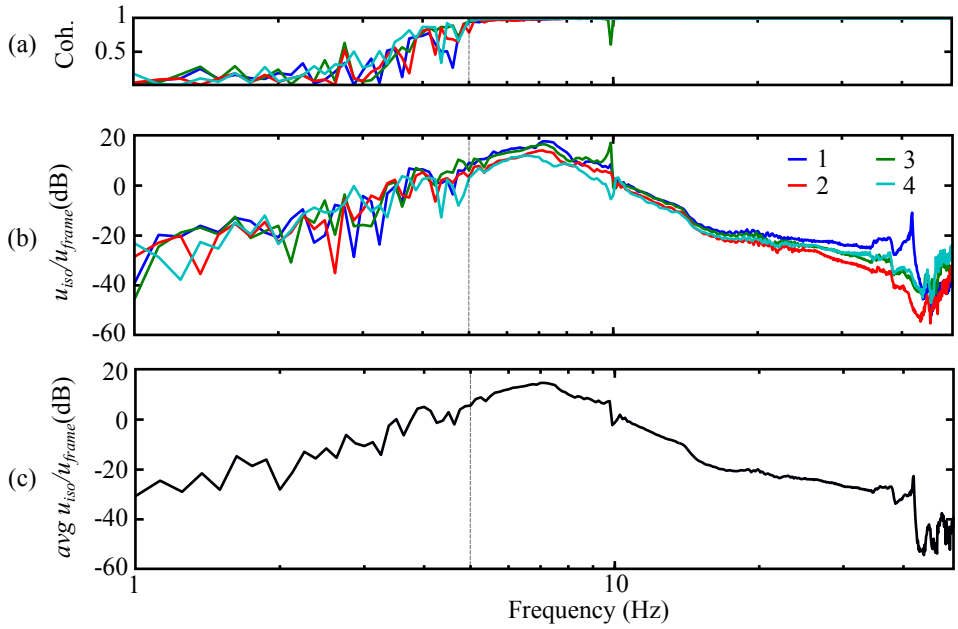

Figure 3.10: Measured transmissibility of sensor isolation system. (a) Coherence of the measurement at each velocimeter position on the frame. (b) Transmissibility determined at each velocimeter position on the frame. (c) Coherent average of transmissibility at each velocimeter position on the frame.

the waveguide was ensonified using the peak excitation voltage allowed by the shaker, and the transfer function between the piston velocity measured by the LDV and the shaker drive voltage was measured using an Agilent 35670A signal analyzer at a total of 127 positions across the piston. The data were downloaded after each measurement to a PC for post-processing in MATLAB.

The transfer function between the measured piston velocity and drive voltage was coherently averaged for all points measured and the averaged transfer function was used to normalize the transfer function at each individual measurement point. The normalized transfer functions across the back side of the piston were

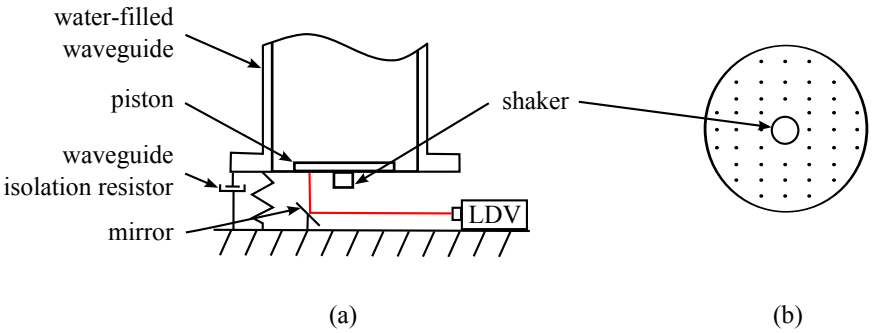

Figure 3.11: (a) Schematic of the LDV setup for the piston velocity measurement. (b) Illustration of measurement points on the bottom of the piston.

plotted for each frequency tested and the author manually searched over the frequency band for structural mode shapes. The result of this search concluded with the identification of several operating deflection shapes shown in Fig. 3.12.

The mode in Fig. 3.12(a) was identified as a rigid-body rocking mode, Fig. 3.12(b) is a rigid-body flapping mode, Fig. 3.12(c) is a bending mode across the piston diameter, and Fig. 3.12(d) is a circumferential mode. The piston mode shape at 1862.7 Hz is within the apparatus design frequency band but it does not appear to disrupt the acoustic pressure in the waveguide shown in Fig. 3.5(a). For completeness, the mode shape predicted in the ANSYS FEA eigenfrequency model was not identified.

An additional result of this measurement is that the spatially-averaged piston velocity was measured. This allowed for a more accurate estimate of the volume velocity within the waveguide and increased agreement between the measured and predicted transfer function between the piston velocity and acoustic pressure shown in Fig. 3.4.

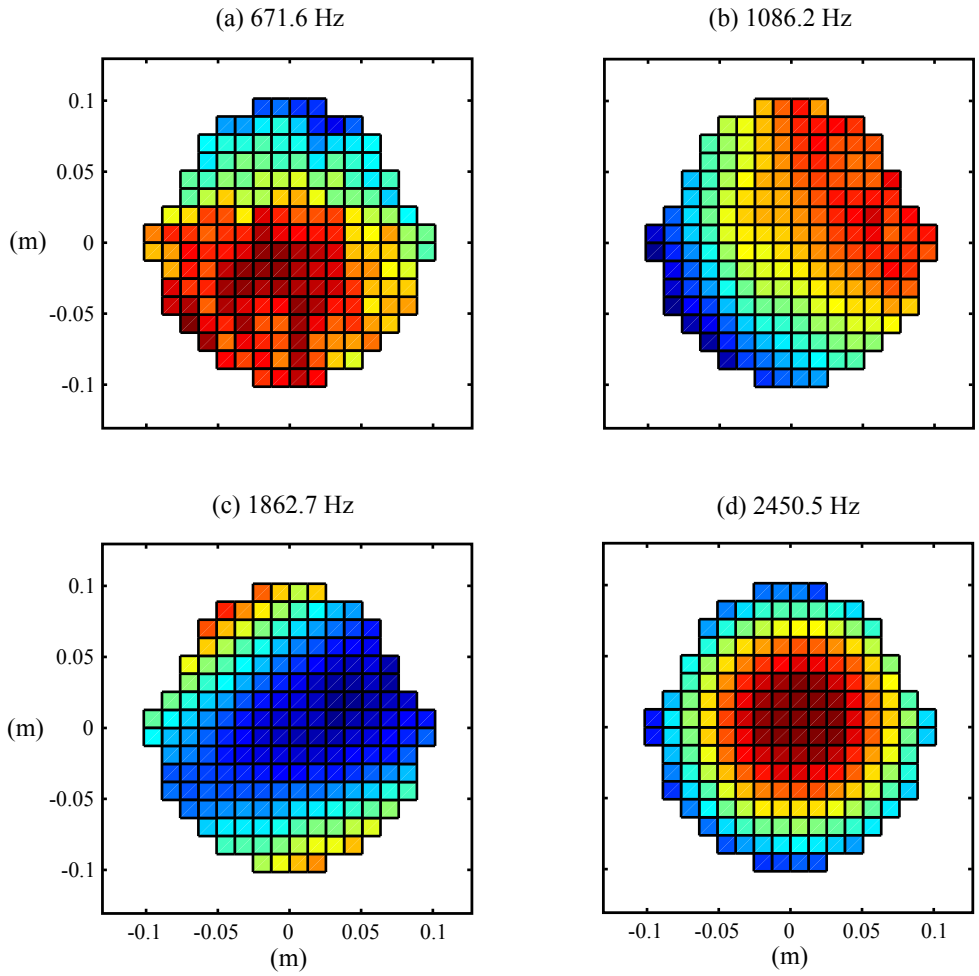

Figure 3.12: Measured modes of apparatus source piston.

3.8 Measured Three-Dimensional Structural Modes of the Waveguide

Prior to construction of the waveguide, COMSOL sound-structure interaction FEA models predicted the existence of structural modes of the waveguide where several of these modes could be disruptive to the acoustic pressure field.

Acoustic pressure measurements taken in the waveguide confirmed the disruption at various frequencies where the modes in the frequency band between 536 and 580 Hz appeared to disrupt the acoustic pressure field the most as shown in Fig. 3.3 and in the wavefront planarity measurements shown in Figs. 3.6 and 3.7. In order to identify the structural mode shapes of the waveguide walls, surface-normal acceleration measurements were made along the length of the water-filled waveguide in 0.1 m increments and in eight circumferential positions around the waveguide for a total of 320 measurement points. The transducer employed for the measurement was an Dytran Instruments, Inc. 3100A accelerometer [56] with a magnetic base. The waveguide was ensonified with a swept-sine signal in a frequency band from 40 to 1250 Hz while recording the transfer function between the accelerometer and the shaker drive signal using an Agilent 35670A signal analyzer. At the completion of each measurement, the data were downloaded onto a PC and post-processed using MATLAB.

In order to identify the structural eigenfrequencies of the waveguide, a mode indicator function, shown as the black curve in Fig. 3.13(a), was constructed. The mode indicator function (MIF) [57] was created by averaging the magnitude of the measured transfer function both along the circumference and the length of the waveguide at each measurement position. The resulting average helps to visualize the eigenfrequencies of the water-filled waveguide and to identify high amplitude structural modes. Additionally, the red curve in Fig. 3.13(a) is the average acoustic pressure measured within the waveguide at depths from 0 to 1.5 m in 0.0375 m increments. The inclusion of this curve illustrates the motion of the waveguide wall under the influence of the acoustic pressure inside the waveguide. The image plot shown in Fig. 3.13(b) was created by averaging the accelerometer data across the

circumference of the waveguide at each axial measurement position. The averaged magnitude was then color-mapped as a function of axial position and frequency to visualize the modal nodes and anti-nodes along the length of the waveguide. Figure 3.13(b) illustrates that a region of high modal density of the waveguide wall exists between 536 and 592 Hz and this frequency band roughly corresponds with the frequency band of non-planar wave fronts shown in Figs. 3.6 and 3.7. Additionally, the modes at 277.5 and 747.9 Hz are two examples of mode shapes with multiple nodes and anti-nodes along the length of the waveguide where the full mode shapes are included in Fig. 3.14. The mode shapes in the 536 to 592 Hz band in Fig. 3.14 confirms the existence of high amplitude waveguide structural modes in the region where calibration measurements are performed and, therefore, calibration data within this frequency band are deemed to be unusable.

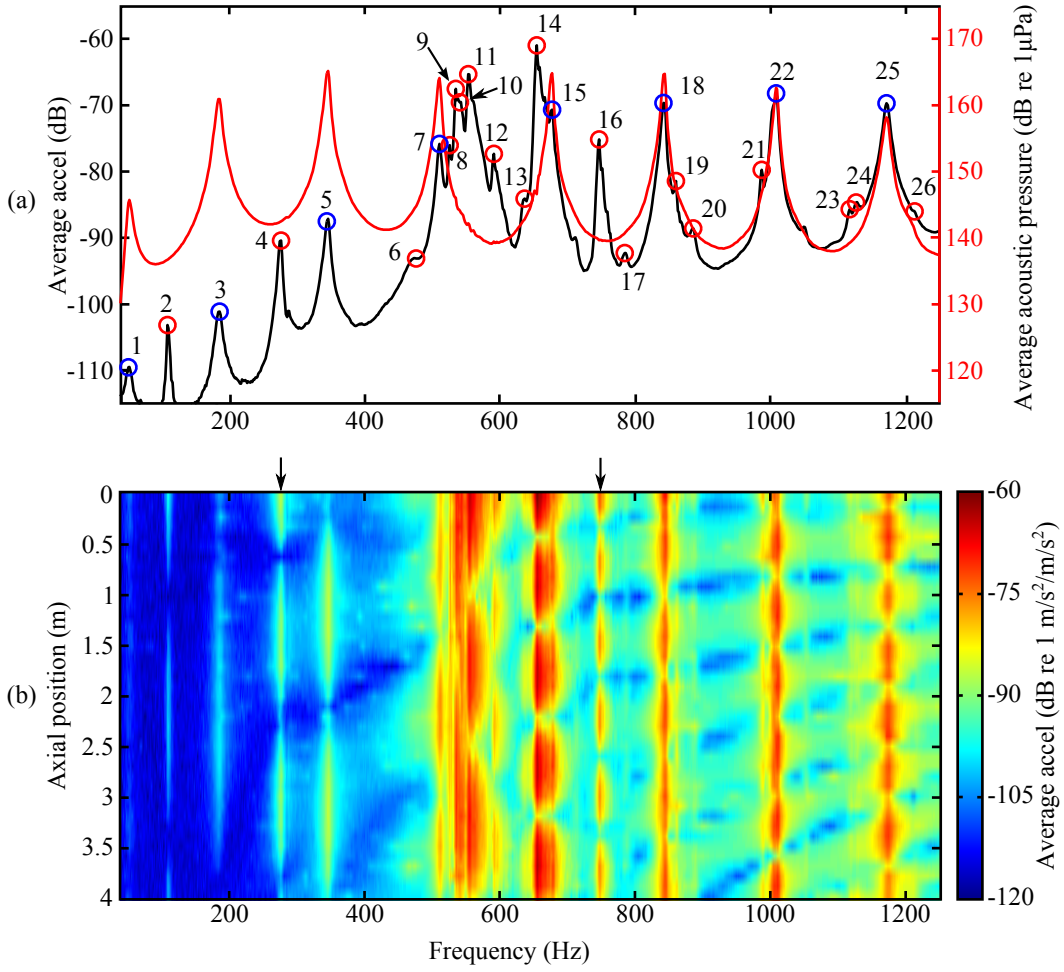

Figure 3.13: (a) Mode indicator function (black curve) of average waveguide wall acceleration and average acoustic pressure (red curve) as a function of frequency. (b) Waveguide wall acceleration averaged over the waveguide outside circumference as a function of axial position and frequency. The two arrows at the top of the figure highlight two modes with multiple nodes and anti-nodes along the waveguide axis of revolution.

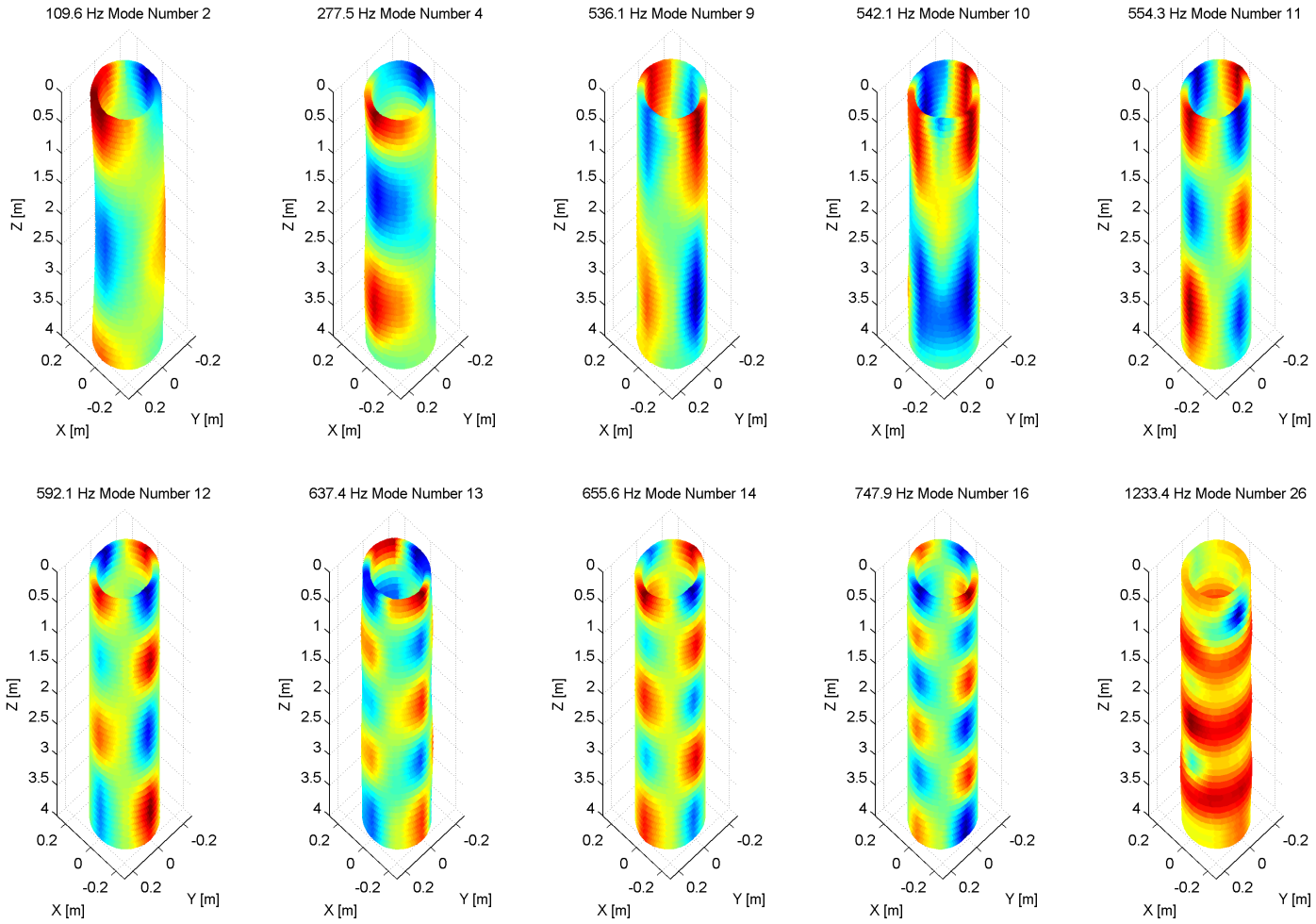

Figure 3.14: Measured mode shapes of waveguide wall acceleration. The mode numbers of each shape illustrated correspond to the mode numbers on the MIF of Fig. 3.13(a).

Chapter 4

Calibration of Underwater Electroacoustic Receivers in a Standing-Wave Apparatus

As described in Sec. 1.2, underwater electroacoustic receivers can be calibrated in a standing-wave apparatus using a comparison method. This chapter details the process of calibrating underwater electroacoustic receivers in such an apparatus where Sec. 4.1 provides a brief overview of the steps taken to make a calibration measurement in the waveguide, Sec. 4.2 describes the algorithm used to post-process the raw standing-wave calibration measurement data and derives the correction factor to relate these data to plane wave, free-field conditions. Sec. 4.3 describes the sources of error in the standing-wave calibration measurements, and Sec. 4.4 presents comparisons of a pressure hydrophone, pressure-gradient vector sensor, and accelerometer-based vector sensor calibration measurements taken in a standing-wave field to those taken in a free-field.

4.1 Calibration Measurement Procedure

This section gives a brief overview of how to prepare the standing-wave apparatus to perform calibration measurements. A detailed measurement procedure is contained in Appendix B.

The calibration measurement setup of an underwater electroacoustic receiver can be performed once the standing-wave apparatus is prepared as described in

Sec. 3.2. First, the acoustic centers of the fully-submerged reference hydrophone and the DUT are carefully placed at the same depth within a region 0.025 to 0.125 m below the air/water interface. Next, the operator ensures there are no bubbles on the surfaces of either transducer, verifies that the acoustic source level does not overload any preamplifier by ensonifying the waveguide and observing the output of all desired channels of each transducer on an oscilloscope, and appropriately sets the input voltage range of the analog-to-digital converter (ADC) on the signal analyzer. The Agilent 35670A signal analyzer computes the transfer function between all recorded channels relative to channel 1, to which the reference hydrophone is connected. Next, an ambient noise measurement is taken with the source amplifier turned off, and then the measurement is repeated with the source turned on. Finally, once the calibration measurement has been completed, the data are downloaded to a PC where they are post-processed using MATLAB. Calibration computations of the omni and directional channels of a vector sensor are performed from the same measurement where the post-processing algorithm first processes the vector sensor omni channel sensitivity relative to the reference hydrophone followed by the directional channel sensitivity relative to the calibrated vector sensor omni.

4.2 Calibration Measurement Post-Processing Algorithm

Comparison calibration measurements are post-processed by compensating for signal gain on each transducer, relating the measured voltage of the reference hydrophone to the acoustic pressure through its sensitivity and then correcting for the differences in the acoustic impedance between free and standing-wave fields. The complex DUT sensitivity M_{DUT} can be found from the calibration

measurement transfer function by

$$M_{\mathrm{DUT}} = \Xi_{\mathrm{sw}}(d,\omega)\left(\frac{e_{\mathrm{out,DUT}} G_{\mathrm{ref}} M_{\mathrm{ref}}}{e_{\mathrm{out,ref}} G_{\mathrm{DUT}}}\right), \tag{4.1}$$

where $e_{\mathrm{out,DUT}}$ is the voltage output of the DUT, G_i is the gain applied to each transducer, $e_{\mathrm{out,ref}}$ is the voltage output of the reference hydrophone, M_{ref} is the sensitivity of the reference hydrophone, and $\Xi_{\mathrm{sw}}(d,\omega)$ is the correction term to relate the standing-wave measurement to the free field. $\Xi_{\mathrm{sw}}(d,\omega)$ is unity for pressure hydrophones and is derived below for vector sensor directional channels.

The directional-channel correction term for a standing-wave field is necessary since the frequency response (transfer function) measured between the vector sensor directional channels and reference hydrophone channel depends on the acoustic impedance of the field in which it is measured. The correction factor is derived by determining the difference between the acoustic impedance of a standing-wave field and a plane wave in a free field. The acoustic impedance at any point in a standing-wave field was derived in Sec. 2.1.1 where Eq. (2.22) is repeated here for convenience

$$Z(x,\omega)_{\mathrm{sw}} = j\rho_0 c_0 \tan(k(l-x)), \tag{4.2}$$

which differs from the free-field, plane wave acoustic impedance

$$Z_{\mathrm{ff}} = \rho_0 c_0, \tag{4.3}$$

by $j\tan(k(l-x))$. Therefore

$$\Xi_{\mathrm{sw}}(x,\omega) = \frac{Z(x,\omega)_{\mathrm{sw}}}{Z_{\mathrm{ff}}} = j\tan(k(l-x)). \tag{4.4}$$

Substitution of $d = l - x$ and accounting for the complex phase velocity within the waveguide from Eq. (2.34) will recast Eq. (4.4) as

$$\Xi_{\text{sw}}(d, \omega) = j \tan(k_{\text{eff}} d), \tag{4.5}$$

where the complex correction factor accounts for both magnitude and phase differences between the acoustic impedance of standing-waves and plane waves in a free field.

The calibration algorithm uploads the linear spectra of all channels and the transfer functions between the DUT channels and the reference hydrophone for both the ambient noise and ensonified measurements along with the accompanying metadata such as measurement depth, transducer preamplifier gain, and sensitivity of the reference transducer. The calibrations are then computed as follows:

1. The signal-to-noise ratio between the ensonified and ambient data SNR_i is computed from the linear spectra of each channel and for all frequency bins measured

$$\text{SNR}_i = 20 \log \left(\frac{e_{\text{out},i,\text{ens}}}{e_{\text{out},i,\text{amb}}} \right), \tag{4.6}$$

   where $e_{\text{out},i,\text{ens}}$ and $e_{\text{out},i,\text{amb}}$ are the ensonified and ambient voltage output levels, respectively, of each channel measured.

2. The transfer function between the DUT omni channel and the reference hydrophone is used to determine the sensitivity of the DUT omni where Eq. (4.1) is recast as

$$M_{\text{DUT,omni}} = \left(\frac{e_{\text{out,DUT,omni}} G_{\text{ref}} M_{\text{ref}}}{e_{\text{out,ref}} G_{\text{DUT,omni}}} \right), \tag{4.7}$$

where $e_{\text{out,DUT,omni}}$ is the voltage output and $G_{\text{DUT,omni}}$ is the applied gain for the DUT omni channel.

3. The signal analyzer computes the transfer function between the DUT directional channel and the reference hydrophone but the complex sensitivity of the DUT directional channel relative to the DUT omni is the desired output from the calibration. To this end, the transfer function between the DUT directional channel and the reference hydrophone is normalized by the transfer function between the DUT omni and the reference hydrophone

$$H_{\text{DUT,dir/omni}} = \frac{e_{\text{out,DUT,dir}} G_{\text{ref}} / e_{\text{out,ref}} G_{\text{DUT,dir}}}{e_{\text{out,DUT,omni}} G_{\text{ref}} / e_{\text{out,ref}} G_{\text{DUT,omni}}} = \frac{e_{\text{out,DUT,dir}} G_{\text{omni}}}{e_{\text{out,DUT,omni}} G_{\text{dir}}}, \quad (4.8)$$

where $e_{\text{out,DUT,dir}}$ is the voltage output and $G_{\text{DUT,dir}}$ is the applied gain for the DUT directional channel. The complex sensitivity of the directional channel is determined by applying the absolute value of the DUT omni sensitivity $M_{\text{DUT,omni}}$ determined from Eq. (4.7) and the standing-wave impedance correction factor Ξ_{sw} to the transfer function $H_{\text{DUT,dir/omni}}$ determined from Eq. (4.8) as

$$M_{\text{DUT,dir}} = j \tan(k_{\text{eff}} d) \frac{e_{\text{out,DUT,dir}} G_{\text{omni}}}{e_{\text{out,DUT,omni}} G_{\text{dir}}} |M_{\text{DUT,omni}}|, \quad (4.9)$$

An SNR threshold of 10 dB is typically used for calibrations where any frequency bin whose SNR for any measured channel does not meet this threshold is not displayed in the calibration curve. Additionally, calibration data in the 536 to 592 Hz frequency band is discarded from the calibration result due to the non-planar wavefronts induced by the structural resonance of the waveguide. Finally, the magnitude and phase of the free-field-corrected receive voltage sensitivity

(RVS) is plotted in dB re 1 V/μPa and degrees, respectively, and the complex calibration data is stored. The MATLAB code of the calibration algorithm is contained in Appendix C.

4.3 Sources of Calibration Error

Comparison calibration measurements in any acoustic field are susceptible to errors arising from non co-located transducers, disruptions of the acoustic field due to the inclusion of either the DUT or the reference hydrophone, inclusion of bubbles on either transducer, and the effects of water temperature fluctuations.

As described throughout this thesis, calibration measurement errors in a standing-wave apparatus can be caused by non-planar wavefronts within the waveguide. Additionally, calibration error associated with placing a DUT omni hydrophone and reference hydrophone at different depths can be estimated from the ratio between the acoustic pressure at the two transducer depths in the waveguide. The ratio is cast by substituting Eq. (2.2) into Eq. (2.21) and dividing the pressure at each depth as

$$\varepsilon_{d,\text{mismatch}} = \frac{\sin(k_{\text{eff}} d_{\text{DUT}})}{\sin(k_{\text{eff}} d_{\text{ref}})} \tag{4.10}$$

where d_{DUT} and d_{ref} are the depths of the DUT and reference hydrophone, respectively. The error as a function of depth mismatch and frequency is shown in Fig. 4.1 for a reference hydrophone depth of 0.075 m and depth mismatch of 0.001 to 0.005 m in 0.001 m increments. As shown in the figure, the calibration measurement error from depth mismatch is approximately 0.11 dB per millimeter of position error. Also, the frequency dependence of the error increases with with increasing position error.

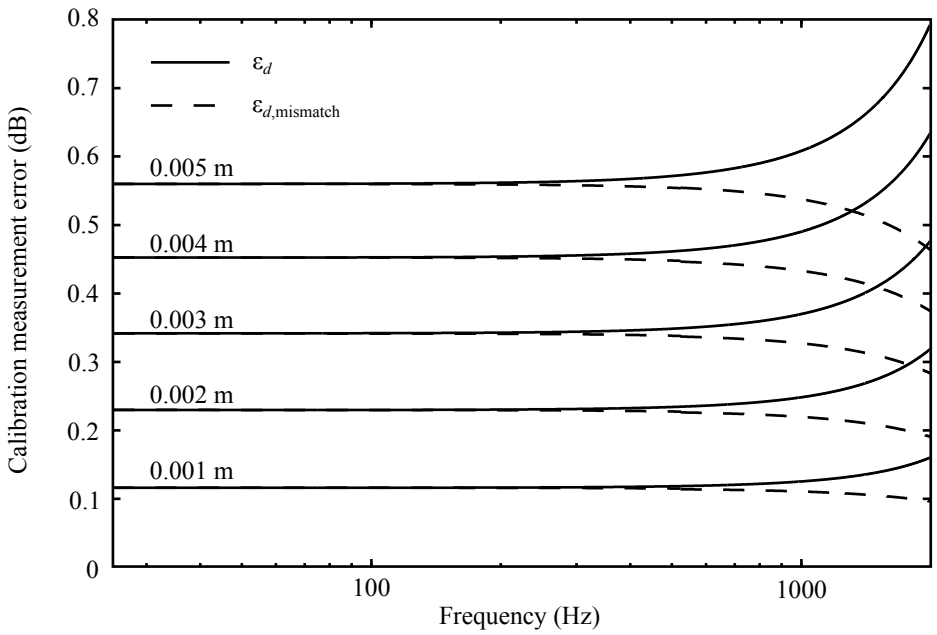

Figure 4.1: Estimated error in calibration measurement $\varepsilon_{d,\text{mismatch}}$ for two pressure hydrophones placed at different depths and vector sensor directional channel post-processing error ε_d from incorrect depth for $d = 0.075$ m.

Additionally, inaccuracies in the depth measurement of a co-located reference hydrophone and DUT will introduce errors in the calibration of vector sensor directional channels. The correction term Ξ_{sw} shown in Eq. (4.5) is dependent on the depth of the reference hydrophone and the DUT below the air/water interface. The calibration measurement error generated from an incorrect depth placement is

$$\varepsilon_d = \frac{\tan(k_{\text{eff}} d_{\text{DUT}})}{\tan(k_{\text{eff}} d)}, \tag{4.11}$$

where the magnitude of the calibration measurement error for a depth error of 0.001 to 0.005 m in 0.001 m increments when $d = 0.075$ m is shown in Fig. 4.1 and is also approximately 0.11 dB per millimeter of depth error. The frequency dependence of the calibration measurement error associated with incorrect depth

placement is greater than for the error associated with the DUT and reference hydrophone placed at two different depths.

Finally, the equilibrium water temperature in the waveguide can vary throughout the year between approximately 18 to 30° C. Consequently, the phase velocity in the waveguide also has a seasonal dependence. The maximum, minimum, and median temperature-dependent phase velocities are shown in Fig. 4.2. The median estimated phase velocity at 24° C, described by Eq. (2.32) and shown in Fig. 4.2, is used to compute k_{eff} in the post-processing algorithm. However, the algorithm does not account for the temperature-dependent shift in the phase velocity. The phase velocities for the temperature extremes vary from the median phase velocity by approximately 14 m/s, which is 1% of the peak median phase velocity. Error introduced by the water temperature uncertainty is ignored since this effect induces magnitude errors on the order of 0.1 dB.

The author's experience with performing calibration measurements in the standing-wave apparatus has shown that the expected positional accuracy is ±2 mm for both the depth of the DUT and the co-location of the DUT omni and reference hydrophone. Therefore, the nominal error associated with ε_d and $\varepsilon_{d,\text{mismatch}}$ is 0.22 dB each. These errors and the error introduced from the water temperature uncertainty combine for an estimated total measurement uncertainty of 0.54 dB plus the uncertainty of the sensitivity of the reference hydrophone for calibration measurements performed in the standing-wave apparatus.

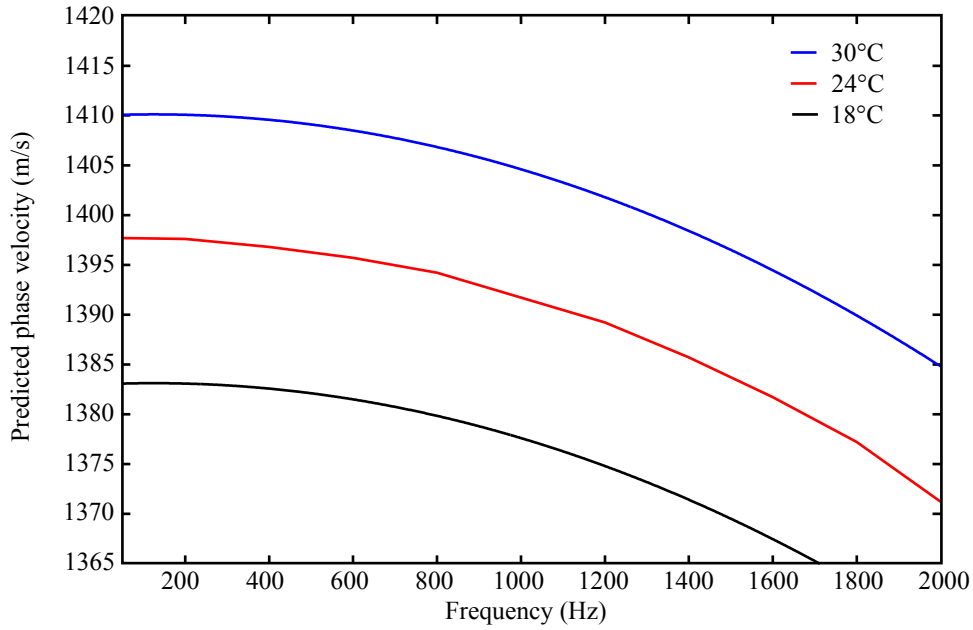

Figure 4.2: Comparison of predicted phase velocities for three equilibrium temperatures in the standing-wave apparatus.

4.4 Measurement Validation

Comparison calibration measurements of a pressure hydrophone, a pressure-gradient vector sensor, and an accelerometer-based vector sensor were made in the standing-wave apparatus. The pressure hydrophone and pressure-gradient vector sensor were then calibrated in a free field at the Lake Travis Test Station (LTTS) of Applied Research Laboratories: The University of Texas at Austin (ARL:UT) [58] and the accelerometer-based vector sensor was calibrated in a large tank at ARL:UT in order to validate the standing-wave calibration measurement procedure and post-processing algorithm. The remainder of this section describes the free-field measurement procedures, derives the correction factor for free-field

calibration measurements of vector sensors when the receiver is not in the geometric far-field of the source, compares the results between standing-wave and free field calibration measurements, and provides a discussion of the author's experience with calibration measurements performed in a free field and in the standing-wave apparatus.

4.4.1 Pressure Hydrophones

The first transducer calibration measurement performed in the standing-wave apparatus was a Teledyne RESON TC4013 pressure hydrophone. The standing-wave correction factor Ξ_{sw} for this transducer type is unity. Additionally, the Teledyne RESON TC4013 is not calibrated below 5 kHz from the manufacturer and this transducer was purchased as the reference hydrophone for the apparatus due to its small size. The Teledyne RESON TC4013 was calibrated in a 25 to 2000 Hz frequency band in the standing-wave apparatus using a NUWC H52 standard hydrophone following the procedures delineated in Appendix B and post-processed using the steps described in Sec. 4.2.

A free-field calibration was also performed at LTTS using a NUWC J9 projector and a NUWC H52 standard hydrophone (this was a different hydrophone than what was used in the standing-wave apparatus) where the measurement setup is illustrated in Fig. 4.3. Both the Teledyne RESON TC4013 and the NUWC H52 were placed at a depth of approximately 3 m (the depth was limited by the Teledyne RESON TC4013 cable length) and the source/receiver distance was estimated to be 1.9 m $\pm$0.1 m. The 10 cm uncertainty resulted because the transducer locations are set at the surface and then the entire measurement setup is lowered to the measurement depth. Precise control of the transducer locations

is not possible at the current LTTS facility. The Teledyne RESON TC4013 and NUWC H52 hydrophones were ensonified using a 30 ms tone burst at a single frequency over a 100 to 2000 Hz frequency band in 25 Hz increments. The tone burst was repeated four times at each frequency and the data were averaged and stored for post-processing in LabVIEW. The recorded data was post-processed by gating the received signal from both the Teledyne RESON TC4013 and NUWC H52 with the edges of the gate corresponding to the arrival of the direct path of the acoustic wave and the arrival of the surface reflection. The signal amplitude at each frequency was determined by a peak detection algorithm, the mean value of the amplitude of the peaks was calculated at each frequency, and the transfer function between the Teledyne RESON TC4013 and the NUWC H52 was computed in order to determine the sensitivity of the Teledyne RESON TC4013. The comparison between the calibration measurements performed in the apparatus and at LTTS are shown in Fig. 4.4. Figure 4.4 shows that the two calibration measurements agreed within 0.6 dB within the overlapping frequency band.

4.4.2 Pressure-Gradient Vector Sensors

The next transducer calibrated was a pressure-gradient vector sensor designed as an engineering prototype at ARL:UT. The transducer was calibrated in both the apparatus and at LTTS. The calibration measurement in the waveguide was performed at a depth of 0.078 m and utilized the calibrated Teledyne RESON TC4013 as the reference hydrophone and the calibration measurement was post-processed as described in Sec. 4.2. The calibration measurement made at LTTS was performed at a depth of 9 m using a NUWC J9 projector where the source/receiver distance was 1.9 m $\pm$ 0.1 m, the reference was a NUWC

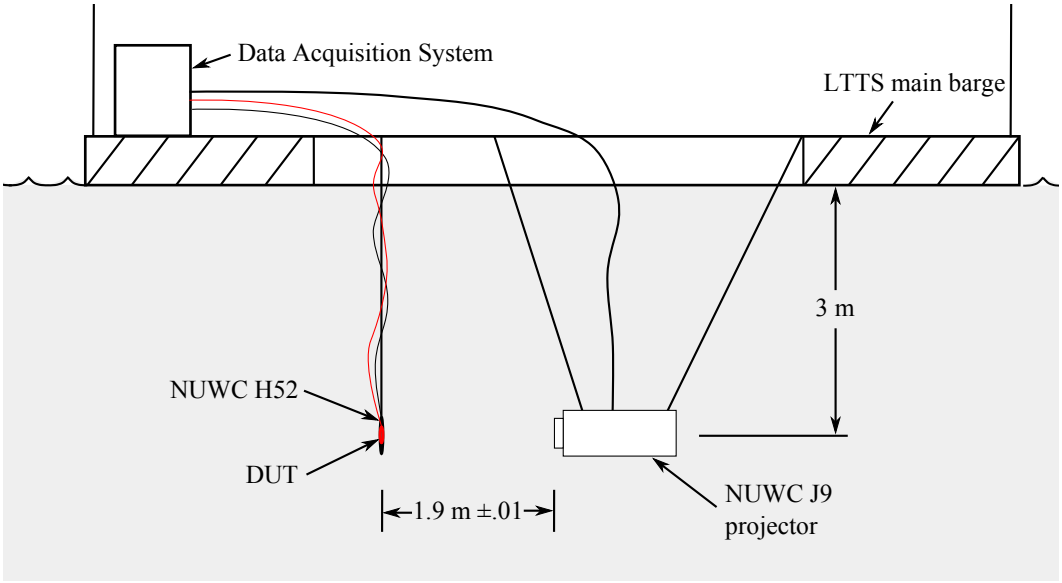

Figure 4.3: Illustration of calibration measurement setup of the Teledyne RESON TC4013 hydrophone calibration of LTTS.

H52 standard hydrophone, and the speed of sound in the water was measured to be 1491 m/s. The transducers were ensonified and post-processed using the same gated-burst technique as described in Sec. 4.4.1. First, the omni channel of the DUT was calibrated to the NUWC H52 standard hydrophone. Next, the NUWC H52 was removed and the directional channels of the DUT were calibrated using the calibrated DUT omni channel as the reference. The directional channel calibrations were post-processed at LTTS using the same technique as for the DUT omni channel.

The conditions at LTTS on the day the pressure-gradient vector sensor and Teledyne RESON TC4013 pressure hydrophone were calibrated were conducive to more accurate calibration measurements due to low ambient acoustic noise levels in Lake Travis. The measurement was performed on 30 October, 2013 on a very

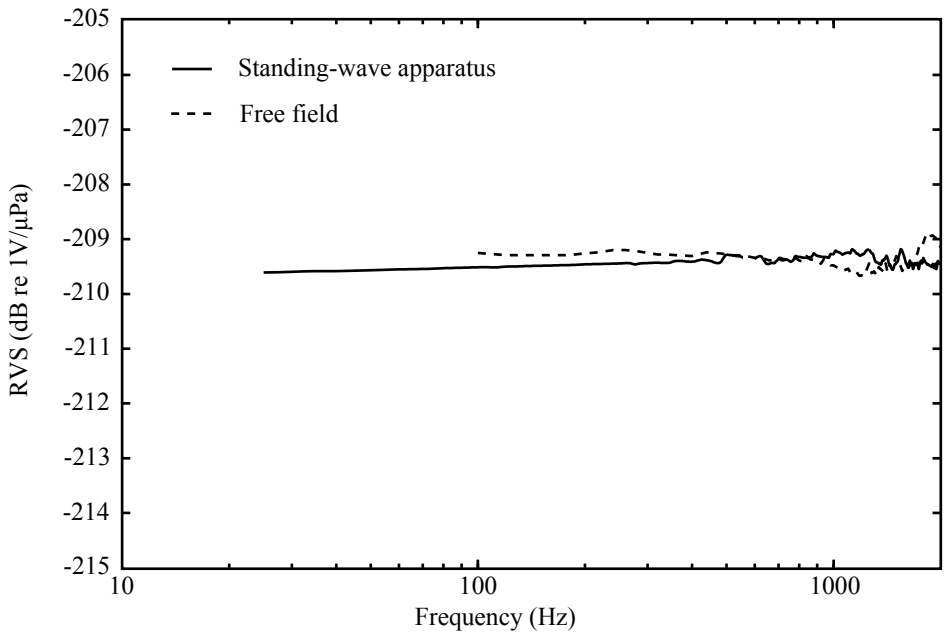

Figure 4.4: Comparison of RVS for a Teledyne RESON TC 4013 in the standing-wave apparatus and at LTTS.

calm day with no recreational boat traffic.

The source/receiver distance for the directional channel calibration at LTTS was such that the acoustic wave was propagating spherically but the frequency response of vector sensor directional channel calibrations are presented for plane waves. The reason for this source/receiver distance was to both increase the SNR of the measurement and to increase the time between the initial direct path and surface-reflected arrivals. This leads to measurements in the geometric near field of the source which must be corrected. The correction factor is determined by the difference in the acoustic impedance between plane and spherical waves. The

acoustic impedance of spherical waves from Ref. [17] is

$$Z_{\text{sph}} = \frac{\rho_0 c_0}{1 + 1/jkr_{\text{sr}}}, \tag{4.12}$$

where r_{sr} is the distance from the observation point to the source. The free field spherical-to-plane wave correction factor for a vector sensor directional channel is

$$\Xi_{\text{ff,sph}} = \frac{Z_{\text{ff}}}{Z_{\text{sph}}}. \tag{4.13}$$

Equation (4.13) can be recast by substituting Eqs. (4.3) and (4.12) as

$$\Xi_{\text{ff,sph}} = \frac{1}{1 + 1/jkr_{\text{sr}}}, \tag{4.14}$$

where $\Xi_{\text{ff,sph}}$ is shown in Fig. 4.5(a) for a range of source/receiver distances and frequencies using a speed of sound of 1491 m/s. Figure 4.5(a) shows that the impedance difference between spherical and plane waves are significant for small values of kr_{sr}. Figure 4.5(b) illustrates the correction factors for a source/receiver distance of 1.9 m and 1491 m/s speed of sound and for a source/receiver distance of 0.8 m and 1499 m/s speed of sound used in $\Xi_{\text{ff,sph}}$ for the calibration described in Sec. 4.4.3. The correction factor required for the pressure-gradient vector sensor calibration measurement described here is the curve for the source/receiver distance of 1.9 m. Figure 4.5(b) shows that at the low frequency limit of the LTTS calibration measurement, the error in the uncorrected magnitude is 4 dB while the phase error is 51°.

Figure 4.6 shows the comparison between the free field, plane-wave-corrected calibration measurements made in the standing-wave apparatus and at LTTS. The magnitude of the two calibrations agree within 1 dB at most frequencies above 200 Hz but errors in the measurement of the source/receiver distance may have

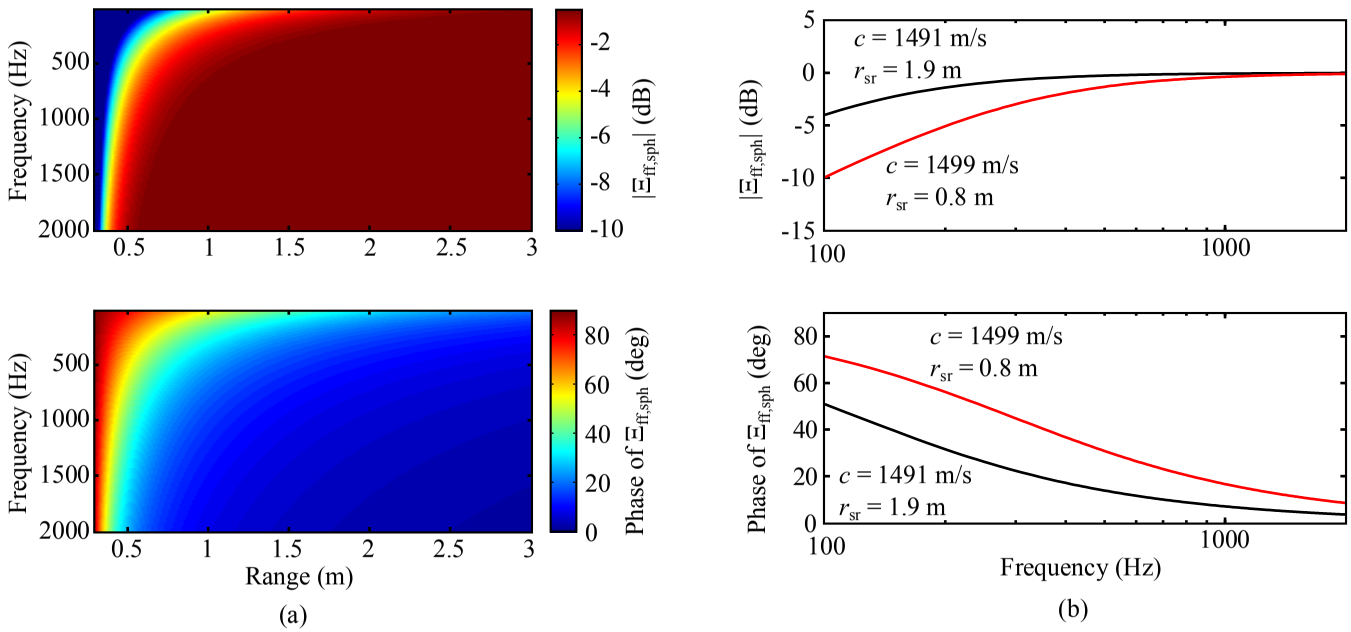

Figure 4.5: (a) Spherical to plane wave correction factor $\Xi_{\text{ff,sph}}$ for vector sensor directional channel calibrations performed in the geometric near-field of the source for a range of distances and frequencies for a 1491 m/s speed of sound. (b) $\Xi_{\text{ff,sph}}$ for 1.9 m source/receiver distance and 1491 m/s speed of sound and 0.8 m source/receiver distance and 1499 m/s speed of sound.

led to the discrepancy seen between the two curves at the lower frequencies. The LTTS calibration facility does not provide phase calibrations of vector sensors but does provide the time series data for the calibration measurement. From this data, the author estimated the phase of the directional channel by cross-correlating the DUT omni and directional channel signals for each frequency measured in order to determine the time delay between the two channels. This delay was then related to the period of the signal at each frequency in order to estimate the phase difference in degrees. The ripples in the LTTS phase measurement are caused by noise in the cross-correlation approach.

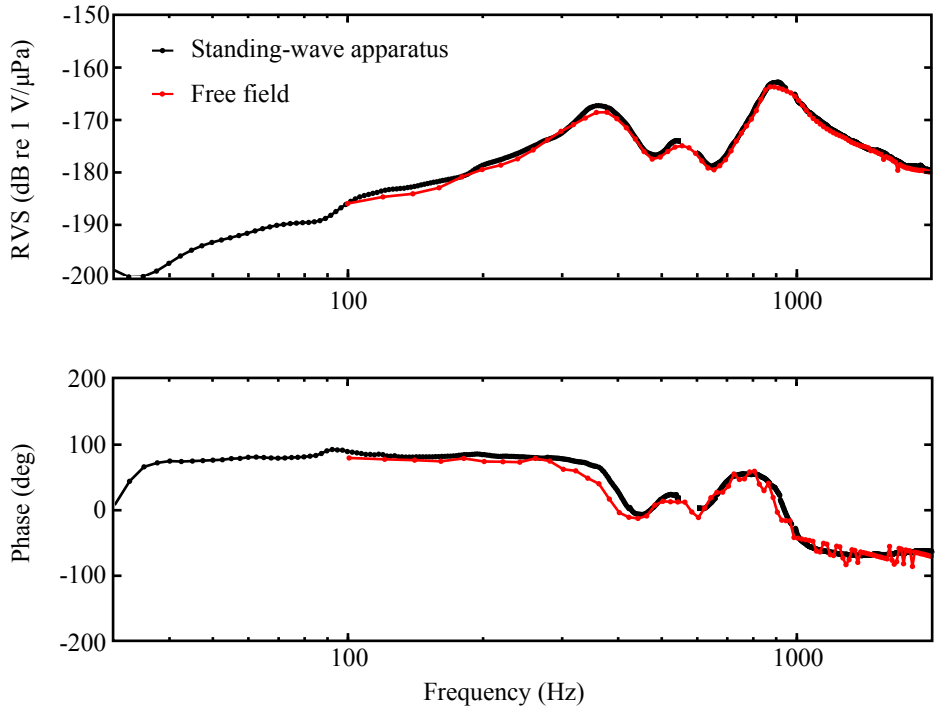

Figure 4.6: Comparison of the results of a pressure-gradient vector sensor calibration measurement between the standing-wave apparatus and at LTTS.

4.4.3 Accelerometer-Based Vector Sensors

Calibration measurements of an accelerometer-based vector sensor were made in both the standing-wave apparatus and the large tank at ARL:UT. The make, model, and RVS levels of the vector sensor are suppressed at the request of the manufacturer but a quantitative comparison between standing-wave and free field calibration measurements can still be presented by relating the magnitude of the RVS of the calibrations to an arbitrary reference.

The calibration measurement of the accelerometer-based vector sensor was made in the waveguide at a depth of 0.075 m using the calibrated Teledyne RESON TC4013 as the standard. The calibration measurement was post-processed using MATLAB in the same manner as described in Sec 4.4.2. The omni channel of the DUT was calibrated to the Teledyne RESON TC4013 standard and then a single directional channel was calibrated to the DUT omni. The free field calibration measurement was performed at a depth of 3.4 m in a cylindrical tank of 18 m diameter and 12 m depth using a NUWC J13 projector as the source, the calibrated Teledyne RESON TC4013 as the reference hydrophone, a source/receiver distance of 0.8 m, and a speed of sound estimate of 1499 m/s from the measured water temperature. The DUT and reference hydrophone were ensonified in a frequency band from 600 to 2000 Hz in 100 Hz increments using a 10 cycle tone burst where the lowest frequency measured was limited by the shallow test depth. The data were recorded using a Tektronix TDS2004C oscilloscope where each tone burst was time-averaged 64 times and the data were downloaded at the end of each test to be post-processed using MATLAB. First, the DUT omni was calibrated to the Teledyne RESON TC4013 reference hydrophone and then the DUT directional

channel was calibrated to the DUT omni.

The data were post-processed in MATLAB by computing the FFT of each channel and then computing the transfer function between the unknown channel and the reference. The magnitude and phase of this transfer function was computed and each were corrected for the impedance difference between spherical and plane waves. The correction factor $\Xi_{\mathrm{ff,sph}}$ for the source/receiver distance of 0.8 m and speed of sound of 1499 m/s is shown in Fig. 4.5(b). This figure illustrates the error in the uncorrected tank calibration measurement to be as high as 10 dB for the magnitude and 70° for the phase.

The comparison of the calibration measurements performed in the standing-wave apparatus and in the large tank are shown in Fig. 4.7. Figure 4.7 shows that the two calibration measurements agree within 1 dB between 600 and 1400 Hz but begin to deviate above 1400 Hz. The discrepancy is possibly due to co-location errors between the DUT and the reference hydrophone for the DUT omni calibration.

4.4.4 Commentary on Calibration Measurements

The author has obtained significant experience in conducting low frequency calibration measurements of underwater electroacoustic receivers before and throughout the development of the standing-wave apparatus. This experience has shown the level of difficulty in obtaining accurate calibration results when performed in a free field. Sources of measurement error in any comparison calibration include high levels of both persistent and transient acoustic noise, electromagnetic interference (especially at power line frequencies), and inaccurate co-location of the

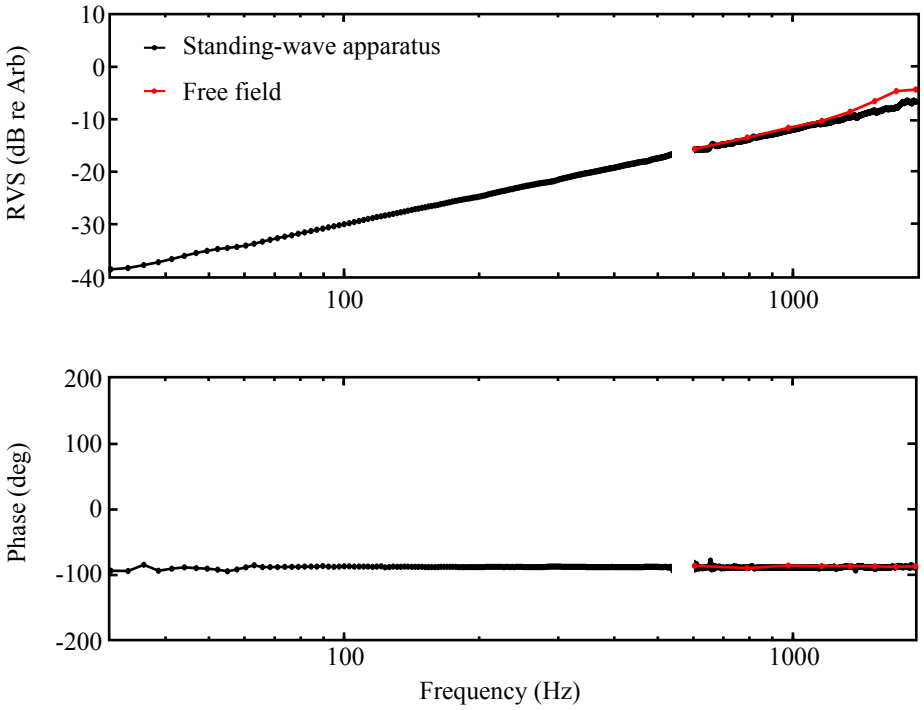

Figure 4.7: Comparison of the results of an accelerometer-based vector calibration measurement between the standing-wave apparatus and in a large tank.

DUT and reference hydrophone. It was found that these error sources generally have been easier to control when performed in a laboratory-based standing-wave apparatus than for a free field. Additionally, calibration measurement limitations associated only with free field calibrations include the ability to obtain and maintain accurate measurements of the source/receiver distance, the effects of reflecting bodies such as facility boundaries and fish, and the ability for the source and receiver to reach a steady-state response within the time between the arrivals of the direct path and surface-reflected wavefronts.

Chapter 5

Conclusion and Future Work

This thesis has presented the development of a laboratory-based, standing-wave apparatus to perform comparison calibration measurements of underwater electroacoustic receivers. Calibration measurements performed in such an apparatus allow one to mitigate some of the difficulties associated with free field calibration measurements such as reducing ambient noise levels, precisely co-locating the DUT and the reference hydrophone, determining and maintaining the source/receiver distance, and avoiding interference from reflecting bodies.

The development of the standing-wave apparatus began with analytical and numerical modeling of a standing-wave field inside an elastic-walled waveguide. The result of this modeling was a 4 m long, vertically-oriented, water-filled waveguide constructed from a 16 inch Schedule 120 steel pipe with a pressure release boundary condition at the top and a velocity boundary condition at the bottom. Modeling showed that this apparatus would support propagation of the ET0 (near-plane wave) mode to zero frequency with minimal dispersion. Additionally, the high frequency limit for calibration measurements of a DUT with a diameter of 0.1 m was determined to be 2000 Hz and was limited by the size of a region within the waveguide that was free of nulls in both the pressure and pressure gradient fields. Three-dimensional FEA models of the water-filled waveguide were created in order

to identify its structural modes and anticipate their effects on the acoustic pressure field within the waveguide.

A velocity source was designed using a piston/shaker assembly. The piston was designed in a manner to decouple its motion from the waveguide walls in order to reduce the amplitude of the ET1 mode. The operating frequency band of the selected shaker was 20 to 3000 Hz, therefore, the design frequency band for calibration measurements in the standing-wave apparatus is 20 to 2000 Hz.

Vibration isolation systems for the waveguide and sensors were designed utilizing mass-spring-damper systems in order to reduce the amplitude of spurious vibrations. The sensor isolation system is mounted to a vertically-oriented linear actuator that allows one to accurately position the DUT and reference transducer within the waveguide. The calibration measurement data are collected using an Agilent 35670A signal analyzer and the analyzer, linear actuator, and measurement parameters are automated using a LabVIEW software program.

The standing-wave apparatus was characterized using a series of measurements. A swept-sine source signal type was chosen for calibration and characterization measurements since it avoids the high transients associated with periodic chirps. During these measurements, it was found that the displacement of the moving mass within the source shaker was high enough to hit the stops at frequencies below 25 Hz. Therefore, the apparatus calibration measurement frequency band is limited to 25 to 2000 Hz.

The acoustic field within the waveguide is made repeatable by degassing the tap water, allowing the system to reach thermal equilibrium with the waveguide, and ensuring that the water level within the waveguide remains constant. Phase

velocity measurements were performed to verify the phase velocity predicted by the Lafleur and Shields algorithm where the measurements and predictions agreed to within 1%.

Acoustic field measurements were performed in order to validate the analytical model of the standing-wave field, identify the locations of nulls in the pressure and pressure gradient fields, verify a region within the standing-wave field suitable for calibration measurements, and determine the maximum obtainable SPL within this region. The result of these measurements showed the analytical model accurately predicted the acoustic field within the waveguide, and that a region 0.025 to 0.125 m below the air/water interface was free of nulls in both the pressure and pressure gradient fields. The range of SPL within this region is 88 to 174 dB re 1 μPa and is deemed sufficient for calibration measurements. The planarity of the wavefront in the calibration measurement region was determined by scanning a Teledyne RESON TC4013 hydrophone in depth and at 13 positions along the diameter of the waveguide. The result from the measurement showed that the wavefronts were planar to within 1 dB for all depths and radial positions and throughout the 25 to 2000 Hz frequency band except between 536 to 580 Hz and at 659 Hz.

Measurements to characterize the waveguide and sensor isolation systems were performed and the results showed that both systems provided at least 20 dB of vibration amplitude reduction at 25 Hz. Additionally, structural measurements were made to determine the mode shapes of both the source piston and waveguide. The result of these measurements showed a piston mode at 1863 Hz and several structural modes of the steel pipe within a 536 to 592 Hz band. Correlation with

acoustic measurements revealed that the piston mode does not disrupt the expected acoustic field but that disruptions of the acoustic pressure field within the 536 to 580 Hz frequency band and at 659 Hz are caused by waveguide structural modes.

Finally, a standing-wave calibration measurement procedure and post-processing algorithm were developed. Sources of measurement error for standing-wave calibrations were identified and the total measurement uncertainty was determined to be $\pm$ 0.54 dB. Comparison calibration measurements were performed in both the standing-wave apparatus and in a free field for a Teledyne RESON TC4013 pressure hydrophone, a pressure-gradient vector sensor, and an accelerometer-based vector sensor. Correction factors for both standing- and spherical- waves were derived to relate the results of vector sensor calibration measurements in these acoustic fields to a plane wave field. The calibration results for the transducers measured were presented and the agreement between the standing-wave and free field results are within 0.6 dB for the pressure hydrophone, 1 dB for most frequencies above 200 Hz for the pressure-gradient vector sensor, and within 1 dB between 600 and 1400 Hz for the accelerometer-based vector sensor.

Continued development of the standing-wave apparatus should include performing calibration measurements of a geophone-based vector sensor in both the standing-wave apparatus and in a free field, attempting to reduce the impact of the structural resonance frequencies of the waveguide in the frequency band between 536 and 592 Hz, and evaluating the feasibility of directivity measurements in the standing-wave apparatus.

Appendices

Appendix A

Design Computations

A.1 Lafleur and Shields Algorithm

The following code is an adaptation of a code by Sagers, which was itself an adaptation of the original code by Wilson.

```
clear all; clc;
% Script to calculate elastic waveguide phase speeds from
% Lafleur and Shields, JASA 97(3):1434-1445
%
% Maps out Cphase vs. Frequency by displaying the
% zero contour of Eq. 5
%
%
% Set C0m: the phase speeds that you are interested in observing
% C1 = intrinsic velocity of sound in fluid (m/s)
% Cc = compressional velocity of sound in solid (m/s)
% Cs = shear velocity of sound in solid (m/s)
%
% b = inner radius of cylinder (m)
% d = outer radius of cylinder (m)
% pl = density of liquid
% pw = density of cylinder wall material
%
% w = angular frequency (rad/s) - CAN BE AN ARRAY!!
% C0m = phase velocity of axisymmetric wave in system (m/s)

%% Input Parameters ------------------------------------------------

C0m                 = 800:5:7500; %Set sound speed range of ...
   interest. (m/s)
fmax                = 8000;       %max value frequency (Hz)
fmin                = 0;          % start value frequency (Hz)
N                   = 100;        % number of frequency steps
```

```
% Material parameters

T = 24;  %temperature of waveguide

C1 = BilaniukandWong(T); %Speed of sound of pure water

mat = 'A36';

switch(mat)
    case 'PVC'       %From McConnell Thesis Table 4.1
        Y          = 2.7e9; %GPa
        nu          = .5;
        pw          = 1295;
        G          = Y./(2*(1+nu));
        Cc          = sqrt((Y*(1-nu))/((pw*(1+nu)*(1-2*nu))));
        Cs          = sqrt(G/pw);
        pw          = 1295;
    case 'al'
        Cc          = 6300;
        Cs          = 3173;
        pw          = 2800;
    case 'ss'
        Cc          = 6100;
        Cs          = 3283;
        pw          = 9000;
    case 'A36'
        pw          = 7850;
        Cc          = 5583;
        Cs          = 3178;
end

% Dimensional inputs
b                   = 13.562/2*.0254;
d                   = 8*.0254;

pl                  = 997;

%% Calculations ----------------------------------------------------
wf                  = 2*pi*fmax; % final frequency
w0                  = 2*pi*fmin; % initial frequency
dw                  = (wf-w0)/(N-1);

sum = complex(zeros(N,length(C0m)));

for n = 1:N
    n;
    w               = (n-1)*dw + w0;
    f(n)            = w/2/pi;
```

```
    sum(n,:)        = LandS_eqsolvr2(C0m,w,C1,Cc,Cs,b,d,pl,pw);
end

lambda = C1./f;

%% Rigid wall dispersion curve ------------------------------------
ap01 = 0;
ap02 = 3.832;
ap03 = 7.016;
ap04 = 10.173;
ap05 = 13.324;

c01 = C1./sqrt(1-(ap01*C1./(2*pi*f*b)).^2); c01(c01<1) = NaN;
c02 = C1./sqrt(1-(ap02*C1./(2*pi*f*b)).^2); c02(c02<1) = NaN;
c03 = C1./sqrt(1-(ap03*C1./(2*pi*f*b)).^2); c03(c03<1) = NaN;
c04 = C1./sqrt(1-(ap04*C1./(2*pi*f*b)).^2); c04(c04<1) = NaN;
c05 = C1./sqrt(1-(ap05*C1./(2*pi*f*b)).^2); c05(c05<1) = NaN;

%% Plots ----------------------------------------------------------
figure()
clf
[C,h] = contour(f,C0m,real(sum)',[-0 0],'LineWidth',2,'Color',[0 ...
    0 0]);
title('Phase Speed in 16" SCH 120 ...
    Waveguide','FontSize',12,'FontWeight','bold')
ylabel('phase speed (m/s)','FontSize',12,'FontWeight','bold')
xlabel('frequency (Hz)','FontSize',12,'FontWeight','bold')
set(gca,'FontSize',12,'FontWeight','bold')
hold on
plot(f,C1.*ones(1,length(f)),'cy','LineWidth',2)



function [ c ] = BilaniukandWong( T )
%   Speed of sound in pure water as a function of temperature
%   Inputs: Water temperature in degrees C

c = 1.40238677*1e3 + 5.03798765.*T - 5.80980033*1e-2.* T.^2 + ...
    3.34296650*...
     1e-4.* T.^3 - 1.47936902 *1e-6 .*T.^4 + 3.14893508 *1e-9 .*T.^5;

end



function sum = LandS_eqsolvr(C0m,w,C1,Cc,Cs,b,d,pl,pw)
```

```
q0m                 = w./C0m;
kl                  = w/Cc;
kt                  = w/Cs;
k1                  = w/C1;

X0m                 = b*sqrt(k1^2-q0m.^2);
Pm                  = sqrt(kl.^2-q0m.^2);
Tm                  = sqrt(kt.^2-q0m.^2);
Em                  = q0m.^2 - kt.^2/2;

Qm                  = ...
    (pl*w^2*b*besselj(0,X0m))./(2*pw*Cs.^2*X0m.*besselj(1,X0m));

% Define L terms
L00_Pm              = besselj(0,d*Pm).*bessely(0,b*Pm) - ...
   besselj(0,b*Pm).*bessely(0,d*Pm);
L00_Tm              = besselj(0,d*Tm).*bessely(0,b*Tm) - ...
   besselj(0,b*Tm).*bessely(0,d*Tm);

L01_Pm              = besselj(0,d*Pm).*bessely(1,b*Pm) - ...
   besselj(1,b*Pm).*bessely(0,d*Pm);
L01_Tm              = besselj(0,d*Tm).*bessely(1,b*Tm) - ...
   besselj(1,b*Tm).*bessely(0,d*Tm);

L10_Pm              = besselj(1,d*Pm).*bessely(0,b*Pm) - ...
   besselj(0,b*Pm).*bessely(1,d*Pm);
L10_Tm              = besselj(1,d*Tm).*bessely(0,b*Tm) - ...
   besselj(0,b*Tm).*bessely(1,d*Tm);

L11_Pm              = besselj(1,d*Pm).*bessely(1,b*Pm) - ...
   besselj(1,b*Pm).*bessely(1,d*Pm);
L11_Tm              = besselj(1,d*Tm).*bessely(1,b*Tm) - ...
   besselj(1,b*Tm).*bessely(1,d*Tm);

% Sum
sum = 1 + ( L11_Pm.*L00_Tm ).*( ...
    (pi^2.*q0m.^2.*b.*d.*Pm.^2.*Tm.^2)./(8*Em.^2) ) + ( ...
    L11_Tm.*L00_Pm ).*( (pi^2*b*d*Em.^2)./(8*q0m.^2) )...
      + ( L10_Pm.*L01_Tm + L01_Pm.*L10_Tm ).*( ...
          (pi^2*b*d*Pm.*Tm)./(8) )...
      + ( b*L11_Pm.*L10_Tm + d*(1+Qm*b).*L11_Pm.*L01_Tm ).*( ...
          (pi^2*Pm.^2.*Tm)./(8*Em) - ...
          (pi^2*Pm.^2.*q0m.^2.*Tm)./(8*Em.^2) )...
      +( b*L11_Tm.*L10_Pm + d*(1+Qm*b).*L11_Tm.*L01_Pm ).*( ...
          (pi^2*Pm.*Em)./(8*q0m.^2) - (pi^2*Pm)./(8) )...
      +( (1 + Qm*b).*L11_Tm.*L11_Pm ).*( (pi^2*Pm.^2)./(8*q0m.^2) ...
          + (pi^2*Pm.^2.*q0m.^2)./(8*Em.^2) - ...
          (pi^2*Pm.^2)./(4*Em) );
```

A.2 Algorithm to Predict Acoustic Field within 16 inch Schedule 120 Steel Waveguide

Code to compute transfer function between acoustic pressure and piston velocity shown in Fig. 2.5, and Fig. 3.4 and transfer function between pressure gradient and piston velocity shown in Fig. 2.6.

```
clear all; clc;

% Script to compute transfer function between acoustic pressure ...
   and piston
% velocity in a waveguide constructed from a 16" Schedule 120 ...
   steel pipe

%Define frequency vector
f       = 1:5:2000;
w       = 2*pi*f;

%Properties of waveguide
rho     = 997;                                  %density of water
c       = -7.39e-6.*f.^2+.0018.*f+1.397e3;      %from Lafleur and ...
   Shields alg.
rp      = .133;                                 %radius of piston
Sp      = pi*rp^2;                              %area of piston
rt      = .17;                                  %inner radius of pipe
St      = pi*rt^2;                              %area of inner pipe
l       = 4;                                    %length of pipe
mu      = .907e-3;                              %viscosity of water
alpha   = 1./rt.*sqrt(mu.*w./(2*rho.*c.^2));    %attenation from ...
   viscosity
k       = w./c+ (1-1i).*alpha;

%% Compute frequency response in waveguide-----------------

dx = .005;
d = 0:dx:l;
for ii=1:length(d)
    TF(ii,:) = Sp/St.*rho./1e-6.*c.*sin(k.*d(ii))./cos(k.*l);
end

%Compute pressure gradient in waveguide
for ii=1:length(d)
```

```
    grad(ii,:) = ...
       -Sp/St.*rho./1e-6.*2*pi.*f.*cos(k.*d(ii))./cos(k.*l);
end

%% Plot-----------------------------------------------
ind = find(d == 4);
TFsm = TF(1:ind,:);
%
figure(),clf
imagesc(f,d(1:ind),20*log10(abs(TFsm)))
h1 = colorbar;
set(gcf,'Name','TF from Simple Model')
caxis([200 280])
xlabel('Frequency (Hz)','FontSize',12,'FontWeight','bold')
ylabel('Depth (m)','FontSize',12,'FontWeight','bold')
ylabel(h1,'dB re 1 uPa/m/s','FontSize',12,'FontWeight','bold')
set(gca,'FontSize',12,'FontWeight','bold')
title('Transfer Function Between Acoustic Pressure and Piston ...
   Velocity')

figure(),clf
imagesc(f,d,20*log10(abs(grad)))
h1 = colorbar;
set(gcf,'Name','Gradient of TF from Simple Model')
caxis([200 280])
xlabel('Frequency (Hz)','FontSize',12,'FontWeight','bold')
ylabel('Depth (m)','FontSize',12,'FontWeight','bold')
ylabel(h1,'dB re 1 uPa/m/m/s','FontSize',12,'FontWeight','bold')
set(gca,'FontSize',12,'FontWeight','bold')
title('Axial Gradient of Transfer Function Between Acoustic ...
   Pressure and Piston Velocity')

figure(),clf
plot(f,20*log10(abs(TF(101,:))),'r')
set(gcf,'Name',['TF from Simple Model at ', num2str(d(ind)), ' m'])
```

A.3 Three-Dimensional Mode Shapes of 16 inch Schedule 120 Steel Waveguide Predicted by COMSOL

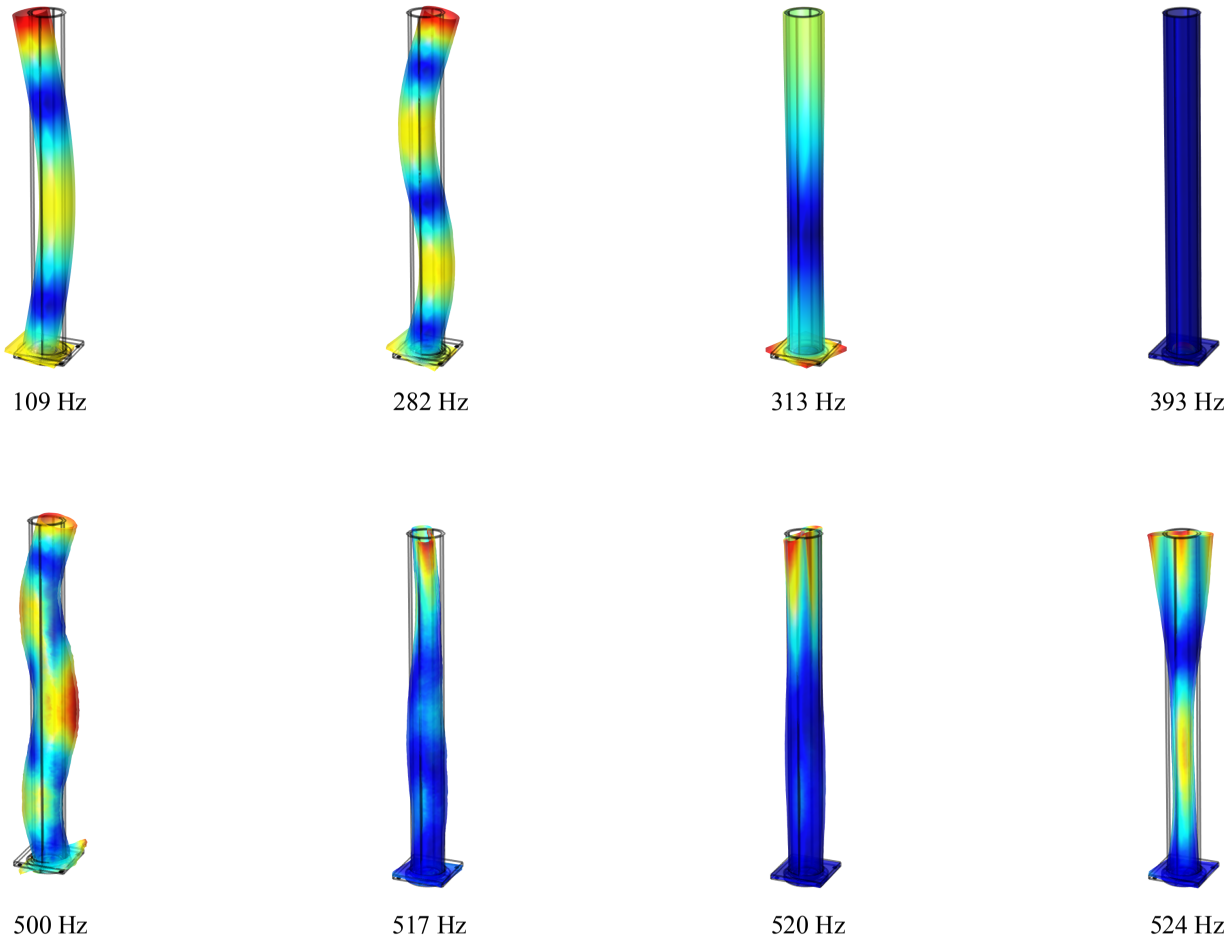

Figure A.1: Mode shapes 1 to 8 of waveguide as predicted by the COMSOL eigenfrequency model.

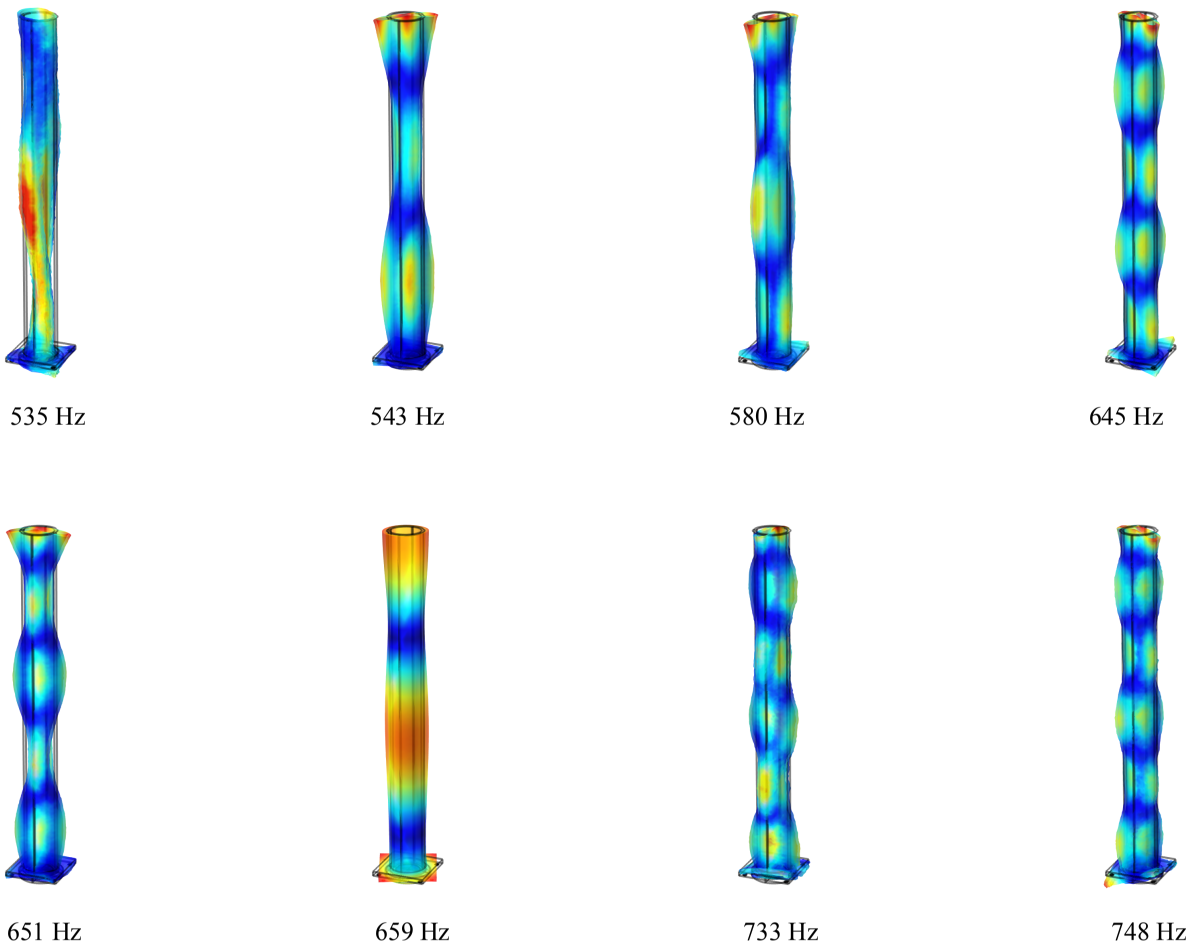

Figure A.2: Mode shapes 9 to 16 of waveguide as predicted by the COMSOL eigenfrequency model.

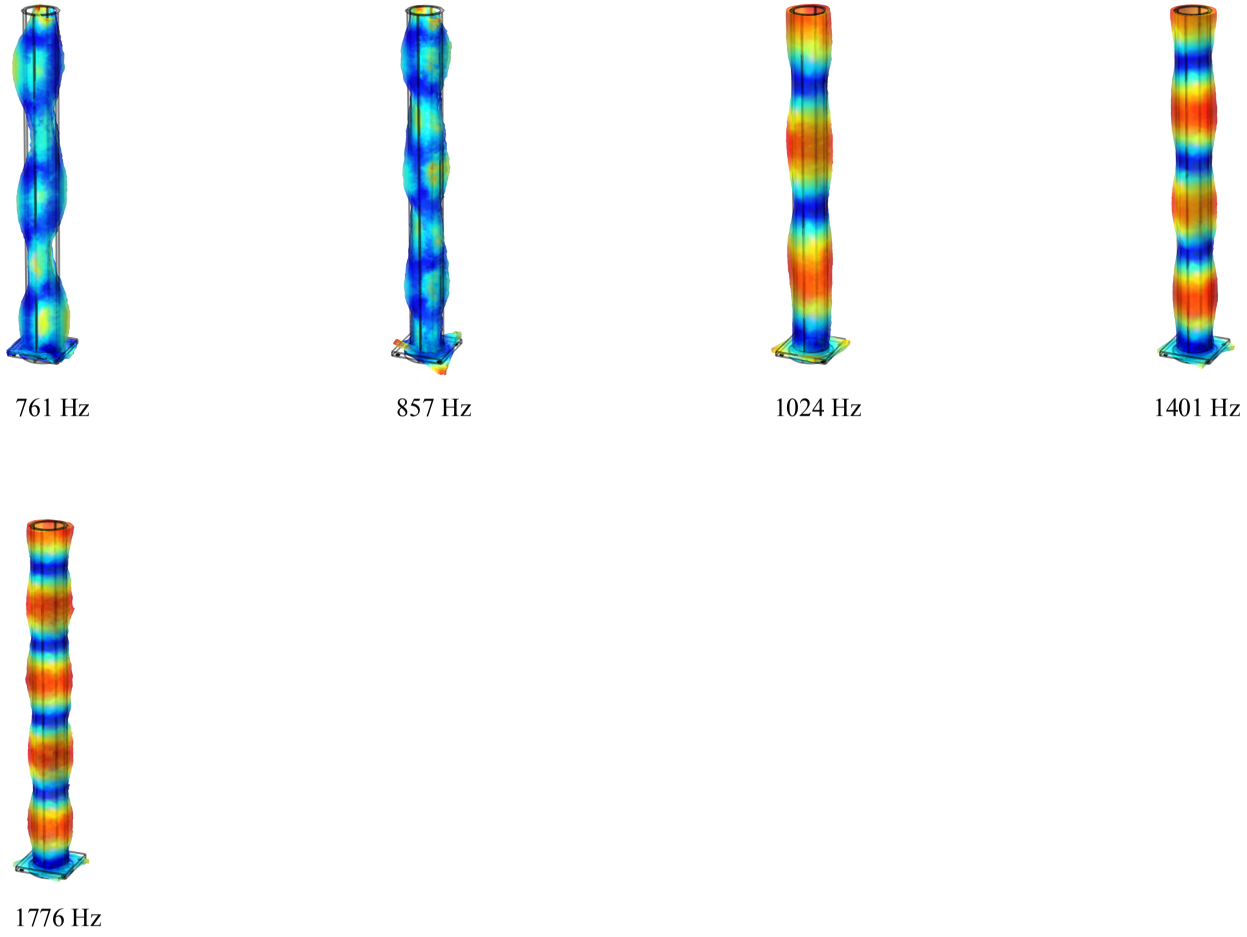

Figure A.3: Mode shapes 17 to 21 of waveguide as predicted by the COMSOL eigenfrequency model.

Appendix B

Standing-Wave Apparatus Calibration Measurement Procedure

The following procedure is to be performed for comparison calibrations in the standing-wave apparatus once the waveguide has been prepared according to Sec. 3.2:

1. Fill out the fields in the LabVIEW data collection system control GUI seen in Fig. B.1. These fields include DUT name and serial number, calibration measurement frequency band, source signal level, frequency resolution desired, signal gain applied to all channels, water depth in waveguide, the measured percent dissolved oxygen, and DUT depth under the air/water interface. The transducer position is controlled through a LabVIEW position control GUI shown in Fig. B.2.

2. Use a water-filled sheath to hold the reference hydrophone and house its cable. Place only the reference hydrophone at the calibration depth for the DUT, ensonify the waveguide, and measure the SPL at the test depth. This measurement will be used to benchmark the acoustic field of the waveguide without a DUT in order to determine if the DUT disrupts the acoustic field when placed at the measurement depth.

3. Suspend the DUT in a suitable manner for calibrations below the sensor isolation mass and lower the transducer into the water until it is fully submerged. Measure the water level in the waveguide and remove the volume of water displaced by the DUT. This step is unnecessary for pressure hydrophones and may be unnecessary for small vector sensors but is imperative for larger vector sensors.

4. Level the DUT relative to the waterline to ensure that the desired transducer response axis is parallel to the axis of revolution of the waveguide and position the acoustic center of the DUT using the PC-controlled actuator to the desired test depth, typically 0.075 m below the air/water interface. It is important to perform this step with the DUT fully submerged in order to account for any change in the position due to the compliance of the DUT mounts.

5. Inspect all surfaces of the DUT and reference hydrophone to ensure no bubbles are attached to either transducer. A small, water-filled syringe is useful for removing bubbles from blind holes and pockets in either transducer.

6. Ensonify the waveguide and measure the SPL using the reference hydrophone and compare this measurement to that taken without the DUT. Ensure that the two measurements agree within 1 dB re 1 μPa across the frequency band desired for the calibration measurement. Generally, if disruptions to the acoustic pressure field occur, it is only at the high end of the measurement frequency band and calibration measurements can still be performed accurately but in a reduced frequency band.

7. Ensonify the waveguide while observing the voltage output of the DUT on an oscilloscope to ensure that any related transducer preamplifier does not overload. Once the optimum SPL inside the waveguide is determined, connect the DUT output to the signal analyzer, ensonify the waveguide, and set the input voltage range of the analog-to-digital converter (ADC) on the signal analyzer to ensure that the DUT and reference hydrophone output voltages at the resonance frequencies of the waveguide are within the half-range and maximum values of the ADC. The input voltage range is entered in the LabVIEW ADC voltage range GUI shown in Fig. B.3.

8. Turn off the piston/shaker assembly power amplifier and record the ambient noise of the DUT and the reference hydrophone. This data will be downloaded to the PC and stored in order to determine the SNR of the ensonified calibration measurement.

9. Ensonify the waveguide while ensuring that no channel overloads during the measurement, record the voltages of the reference hydrophone and DUT channels, and download them to a PC to be post-processed in MATLAB. For a high sensitivity DUT, it is important to observe the ambient noise in the laboratory to ensure that it does not change significantly during the test. If a transient noise occurs during the calibration measurement, it is up to the operator to consider repeating the measurement to ensure a satisfactory SNR was achieved.

10. Run the post-processing algorithm and inspect the results. It is recommended to perform the calibration measurement several times where the DUT is

removed from and replaced in the water, the DUT is inspected and any bubbles are removed, and the DUT depth is verified between each measurement. This process is to ensure that the results are repeatable.

11. Save the frequency vector and final complex calibration result.

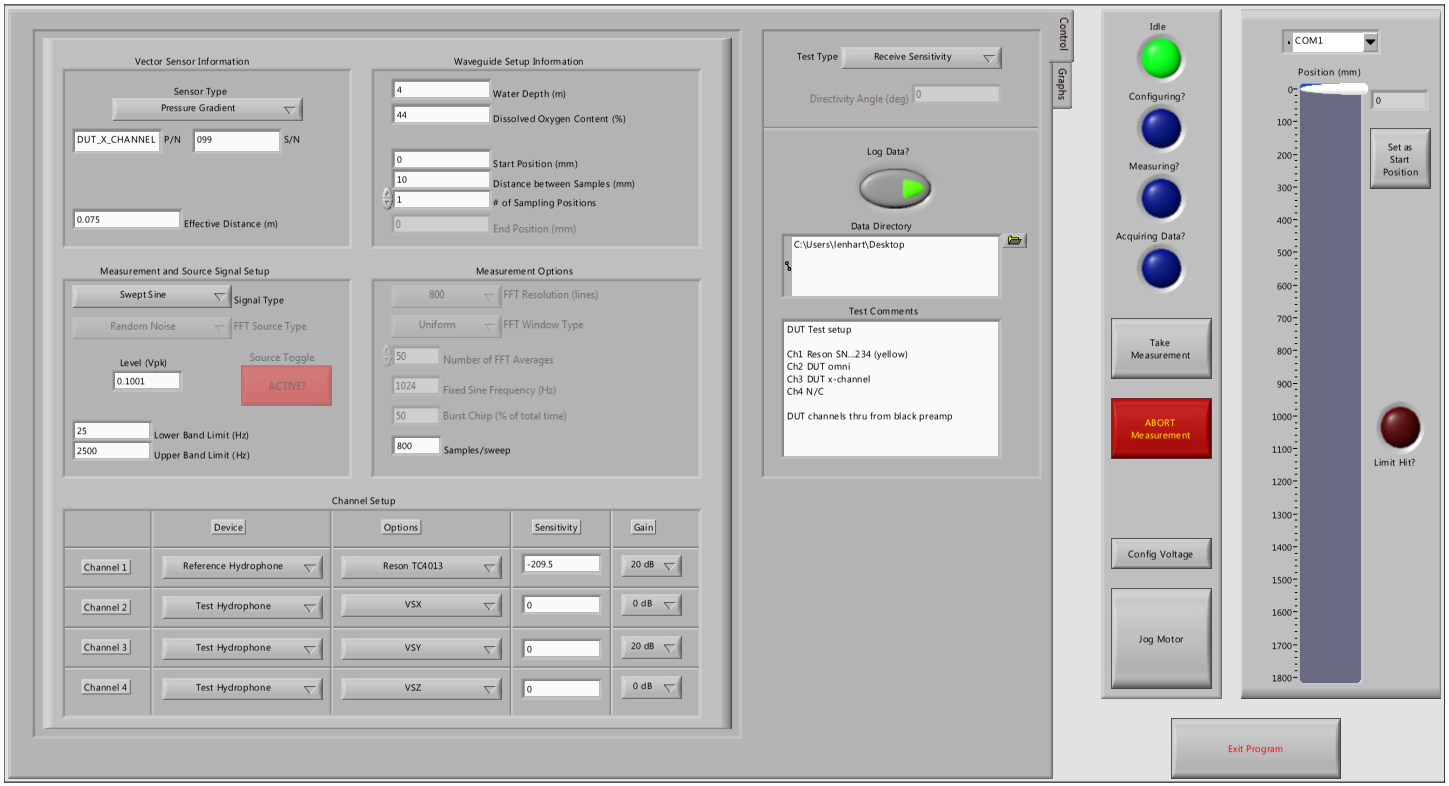

Figure B.1: LabVIEW data collection system control GUI.

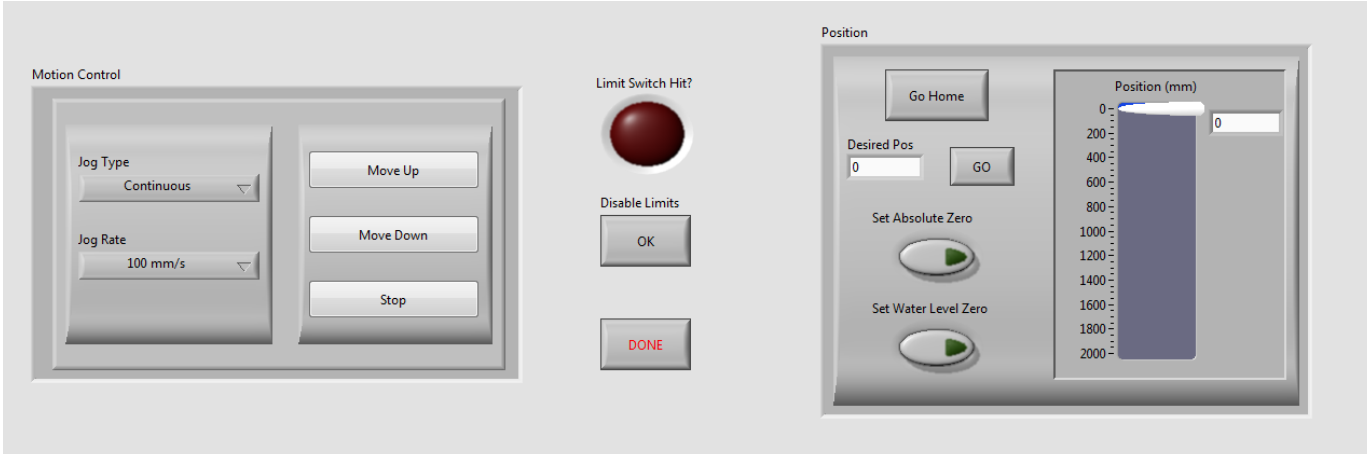

Figure B.2: LabVIEW position control GUI.

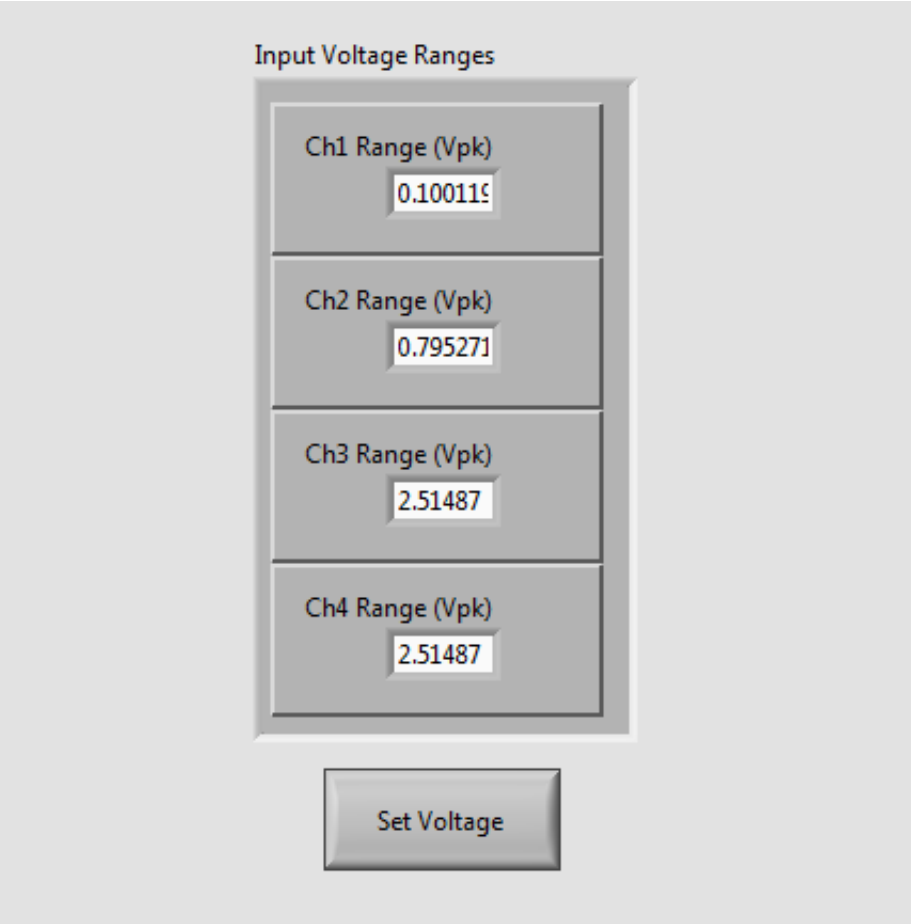

Figure B.3: LabVIEW ADC voltage range GUI.

Appendix C

Standing-Wave Apparatus Calibration Measurement Post-Processing Algorithm

```
% Script to post-process calibration measurements taken in the
% standing-wave apparatus at ARL

% Channel 1 is reference hydrophone
% Channel 2 is DUT omni
% Channel 3 is DUT directional channel
% Channel 4 N/C

% Both ensonified and ambient noise measurements must be taken
% with NO changes to setup between measurements

%%
clear all; clc;

%% Define path and file names to the *.tdms files
% Get path and filename to ambient noise measurement
[datafile.amb.filename,datafile.amb.pathname,¬] = ...
    uigetfile('*.tdms','Select Ambient Noise file');

% Get path and filename to calibration measurement -----------
[datafile.cal.filename,datafile.cal.pathname,¬] = ...
    uigetfile('*.tdms','Select Calibration Data file');

%% Read in the data files -------------------------------------
A       = convert_TDMS([datafile.amb.pathname ...
    datafile.amb.filename]);
C       = convert_TDMS([datafile.cal.pathname ...
    datafile.cal.filename]);
clc

%% Simple error checking --------------------------------------
if any(A(1,1).frequency.data ≠ C(1,1).frequency.data)
```

```
    error('The frequency vectors in the AMBIENT and CALIBRATION ...
       data files are different');
end

%% Default processing parameters --------------------------
f       = A(1,1).frequency.data;           % freq vector [Hz]
omega   = 2*pi*f;                          % freq vector [rad/s]
c       = -7.39e-6.*f.^2 + 0.0018.*f + 1397; %phase velocity ...
   estimated by L&S at 24  C  [m/s]
a       = .1722;                             %inner radius of ...
   waveguide [m]
mu      = .907e-3;                           %viscosity of water ...
   at 24  C
alpha   = (1/a)*sqrt(mu.*(2*pi*f)./(2*997.*(c).^2)); %attenuation ...
   from viscosity between water and wall
k       = omega./c + (1-1i)*alpha;           % complex wavenumber ...
   from phase velocity and losses
d       = A(1,end).Props.effective_distance__m_; %depth of DUT ...
   below surface [m]

%% Process calibration data --------------------------------
% Load calibration measurement data
% Need linear spectra and transfer functions

Npts.amb    = numel(A)-1;
Npts.cal    = numel(C)-1;

% Loop over channel number
for i = 1:4
    Amb{i}.sensor.type  = ...
       eval(['A(1,end).Props.Channel_',num2str(i),'_Device;']);
    Amb{i}.sensor.brand = ...
       eval(['A(1,end).Props.Channel_',num2str(i),'_Options;']);
    Amb{i}.gain.dB = eval(['str2double(A(1,end).Props.Channel_',...
    num2str(i),'_Gain);']);
    Amb{i}.gain.lin     = 10^(Amb{i}.gain.dB/20);
    Amb{i}.sens.dB      = eval(['A(1,end).Props.Channel_',...
    num2str(i),'_Sensitivity;']);
    Amb{i}.sens.lin     = 10^(Amb{i}.sens.dB/20);

    Cal{i}.sensor.type  = ...
       eval(['C(1,end).Props.Channel_',num2str(i),'_Device;']);
    Cal{i}.sensor.brand = ...
       eval(['C(1,end).Props.Channel_',num2str(i),'_Options;']);
    Cal{i}.gain.dB = eval(['str2double(C(1,end).Props.Channel_',...
    num2str(i),'_Gain);']);
    Cal{i}.gain.lin     = 10^(Cal{i}.gain.dB/20);
```

```
    Cal{i}.sens.dB      = ...
       eval(['C(1,end).Props.Channel_',num2str(i),'_Sensitivity;']);
    Cal{i}.sens.lin     = 10^(Cal{i}.sens.dB/20);

    % Loop over the number of measurement points and extract the data
    for in = Npts.amb:-1:1
        Amb{i}.spect.linsq(in,:)    = ...
           eval(['A(1,in).ch',num2str(i),'_power_spectrum.data;']);
        Cal{i}.spect.linsq(in,:)    = ...
           eval(['C(1,in).ch',num2str(i),'_power_spectrum.data;']);

        if i > 1
        realtemp  = eval(['C(1,in).c_',num2str(i),'...
        _1_frequency_response__real_.data']);
        imagtemp = eval(['C(1,in).c_',num2str(i),'...
        _1_frequency_response__imag_.data']);
        Cal{i}.spect.frf(in,:)  = realtemp + 1j*imagtemp; ...
                        % Complex FRF relative to channel 1 [V/V]
        end

        clear realtemp imagtemp
    end
end

%% Load in measured Reson calibration file --------------
load('Reson_TC4013_SN_2212234_Sens.mat')
load('Reson_TC4013_SN_2212263_Sens.mat')

% Linearize the Reson sensitivity
Reson.f             = linspace(25,2000,801);

Reson.SN2212234.dB  = Reson_TC4013_SN_2212234_Sens;
Reson.SN2212234.lin = 10.^(Reson.SN2212234.dB/20);
Reson.SN2212234.lin = interp1(Reson.f,Reson.SN2212234.lin,f);

Reson.SN2212263.dB  = Reson_TC4013_SN_2212263_Sens;
Reson.SN2212263.lin = 10.^(Reson.SN2212263.dB/20);
Reson.SN2212263.lin = interp1(Reson.f,Reson.SN2212263.lin,f);

%% SNR computations ---------------------------------
% Check each channel
for i = 1:4
    Cal{i}.SNR = 10*log10(abs(Cal{i}.spect.linsq))-...
    10*log10(abs(Amb{i}.spect.linsq));
    Cal{i}.SNRidx   = find(Cal{i}.SNR < 10);
end

% find indices of 536-592 Hz band
```

```
[¬,indres1]          = min(abs(f-536));
[¬,indres2]          = min(abs(f-592));

SNRidx               = unique([Cal{1}.SNRidx Cal{2}.SNRidx ...
   Cal{3}.SNRidx indres1:indres2]);



%% Calculations ------------------------------------------
ResonColor = 'yellow';
switch ResonColor
    case 'red'
        DUT.omni.sens   = ...
           (Cal{2}.spect.frf).*(Cal{1}.gain.lin./Cal{2}.gain.lin)...
        .*Reson.SN2212263.lin;
    case 'yellow'
        DUT.omni.sens   = ...
           (Cal{2}.spect.frf).*(Cal{1}.gain.lin./Cal{2}.gain.lin)...
        .*Reson.SN2212234.lin;
end

DUT.dir.sens = ((Cal{3}.spect.frf.*Cal{2}.gain.lin) ./ ...
   (Cal{2}.spect.frf.*Cal{3}.gain.lin))...
.*abs(DUT.omni.sens).*(1j.*tan(k*d));

DUT.omni.sens_dB_sm = smoothn(20*log10(abs(DUT.omni.sens)),5);
DUT.dir.sens_dB_sm = smoothn(20*log10(abs(DUT.dir.sens)),5);
DUT.dir.sens_phase = smoothn(180/pi*angle(DUT.dir.sens),5);

DUT.dir.sens(SNRidx)    = NaN;
DUT.dir.sens_dB_sm(SNRidx) = NaN;
DUT.dir.sens_phase(SNRidx) = NaN;
DUT.omni.sens(SNRidx)   = NaN;
DUT.omni.sens_dB_sm(SNRidx) = NaN;

%%
figure(),clf
subplot 211
semilogx(f,DUT.dir.sens_dB_sm,'LineWidth',2)
ylabel('RVS (dB re 1V/\muPa)','FontSize',12,'FontWeight','bold')
set(gca,'FontSize',12,'FontWeight','bold')
title({'Directional Channel Receive Sensitivity','Test Date' ...
   A(1,end).Props.date_of_test})

grid on
xlim([10 2000])

subplot 212
```

```
semilogx(f,DUT.dir.sens_phase,'LineWidth',2)
ylabel('Phase (degrees)','FontSize',12,'FontWeight','bold')
xlabel('Frequency (Hz)','FontSize',12,'FontWeight','bold')
ylim([-200 200])
set(gca,'FontSize',12,'FontWeight','bold')
grid on
xlim([10 2000])

figure(),clf
semilogx(f,DUT.omni.sens_dB_sm,'LineWidth',2)
ylabel('RVS (dB re 1V/\muPa)','FontSize',12,'FontWeight','bold')
set(gca,'FontSize',12,'FontWeight','bold')
title({'Omni Channel Receive Sensitivity','Test Date' ...
   A(1,end).Props.date_of_test})
grid on
xlim([10 2000])
ylim([min(DUT.omni.sens_dB_sm)-10 max(DUT.omni.sens_dB_sm+10)])

function [z,s,exitflag] = smoothn(varargin)

% Smoothn is a robust, automatic smoothing routing written by  ...
   Anil Gannepalli.
% http://www.mathworks.com/matlabcentral/fileexchange/725-smoothn

function Y = smoothn(X,sz,filt,std)

%SMOOTHN Smooth N-D data
%   Y = SMOOTHN(X, SIZE) smooths input data X. The smoothed data is
%       retuirned in Y. SIZE sets the size of the convolution kernel
%       such that LENGTH(SIZE) = NDIMS(X)
%
%   Y = SMOOTHN(X, SIZE, FILTER) Filter can be 'gaussian' or ...
   'box' (default)
%       and determines the convolution kernel.
%
%   Y = SMOOTHN(X, SIZE, FILTER, STD) STD is a vector of standard ...
   deviations
%       one for each dimension, when filter is 'gaussian' ...
   (default is 0.65)

%     $Author: ganil $
%     $Date: 2001/09/17 18:54:39 $
%     $Revision: 1.1 $
%     $State: Exp $

if nargin == 2,
  filt = 'b';
elseif nargin == 3,
```

```
  std = 0.65;
elseif nargin>4 | nargin<2
  error('Wrong number of input arguments.');
end

% check the correctness of sz
if ndims(sz) > 2 | min(size(sz)) ≠ 1
  error('SIZE must be a vector');
elseif length(sz) == 1
  sz = repmat(sz,ndims(X));
elseif ndims(X) ≠ length(sz)
  error('SIZE must be a vector of length equal to the ...
     dimensionality of X');
end

% check the correctness of std
if filt(1) == 'g'
  if length(std) == 1
    std = std*ones(ndims(X),1);
  elseif ndims(X) ≠ length(std)
    error('STD must be a vector of length equal to the ...
       dimensionality of X');
  end
  std = std(:)';
end

sz = sz(:)';

% check for appropriate size
padSize = (sz-1)/2;
if ¬isequal(padSize, floor(padSize)) | any(padSize<0)
  error('All elements of SIZE must be odd integers ≥ 1.');
end

% generate the convolution kernel based on the choice of the filter
filt = lower(filt);
if (filt(1) == 'b')
  smooth = ones(sz)/prod(sz); % box filter in N-D
elseif (filt(1) == 'g')
  smooth = ndgaussian(padSize,std); % a gaussian filter in N-D
else
  error('Unknown filter');
end


% pad the data
X = padreplicate(X,padSize);
```

```
% perform the convolution
Y = convn(X,smooth,'valid');

%%%%%%%%%%%%%%%%%%%%%%%%%%%%%%%%%%%%%%%%%%%%

function h = ndgaussian(siz,std)

% Calculate a non-symmetric ND gaussian. Note that STD is scaled ...
   to the
% sizes in SIZ as STD = STD.*SIZ


ndim = length(siz);
sizd = cell(ndim,1);

for i = 1:ndim
  sizd{i} = -siz(i):siz(i);
end

grid = gridnd(sizd);
std = reshape(std.*siz,[ones(1,ndim) ndim]);
std(find(siz==0)) = 1; % no smoothing along these dimensions as ...
   siz = 0
std = repmat(std,2*siz+1);


h = exp(-sum((grid.*grid)./(2*std.*std),ndim+1));
h = h/sum(h(:));

%%%%%%%%%%%%%%%%%%%%%%%%%%%%%%%%%%%%%%%%%%%%

function argout = gridnd(argin)

% exactly the same as ndgrid but it accepts only one input ...
   argument of
% type cell and a single output array

nin = length(argin);
nout = nin;

for i=nin:-1:1,
  argin{i} = full(argin{i}); % Make sure everything is full
  siz(i) = prod(size(argin{i}));
end
if length(siz)<nout, siz = [siz ones(1,nout-length(siz))]; end

argout = [];
for i=1:nout,
```

```
  x = argin{i}(:); % Extract and reshape as a vector.
  s = siz; s(i) = []; % Remove i-th dimension
  x = reshape(x(:,ones(1,prod(s))),[length(x) s]); % Expand x
  x = permute(x,[2:i 1 i+1:nout]);% Permute to i'th dimension
  argout = cat(nin+1,argout,x);% Concatenate to the output
end

%%%%%%%%%%%%%%%%%%%%%%%%%%%%%%%%%%%%%%%%%%%%%%

function b=padreplicate(a, padSize)
%Pad an array by replicating values.
numDims = length(padSize);
idx = cell(numDims,1);
for k = 1:numDims
  M = size(a,k);
  onesVector = ones(1,padSize(k));
  idx{k} = [onesVector 1:M M*onesVector];
end

b = a(idx{:});
```

Appendix D

Engineering Drawings

D.1 Standing-Wave Apparatus Assembly

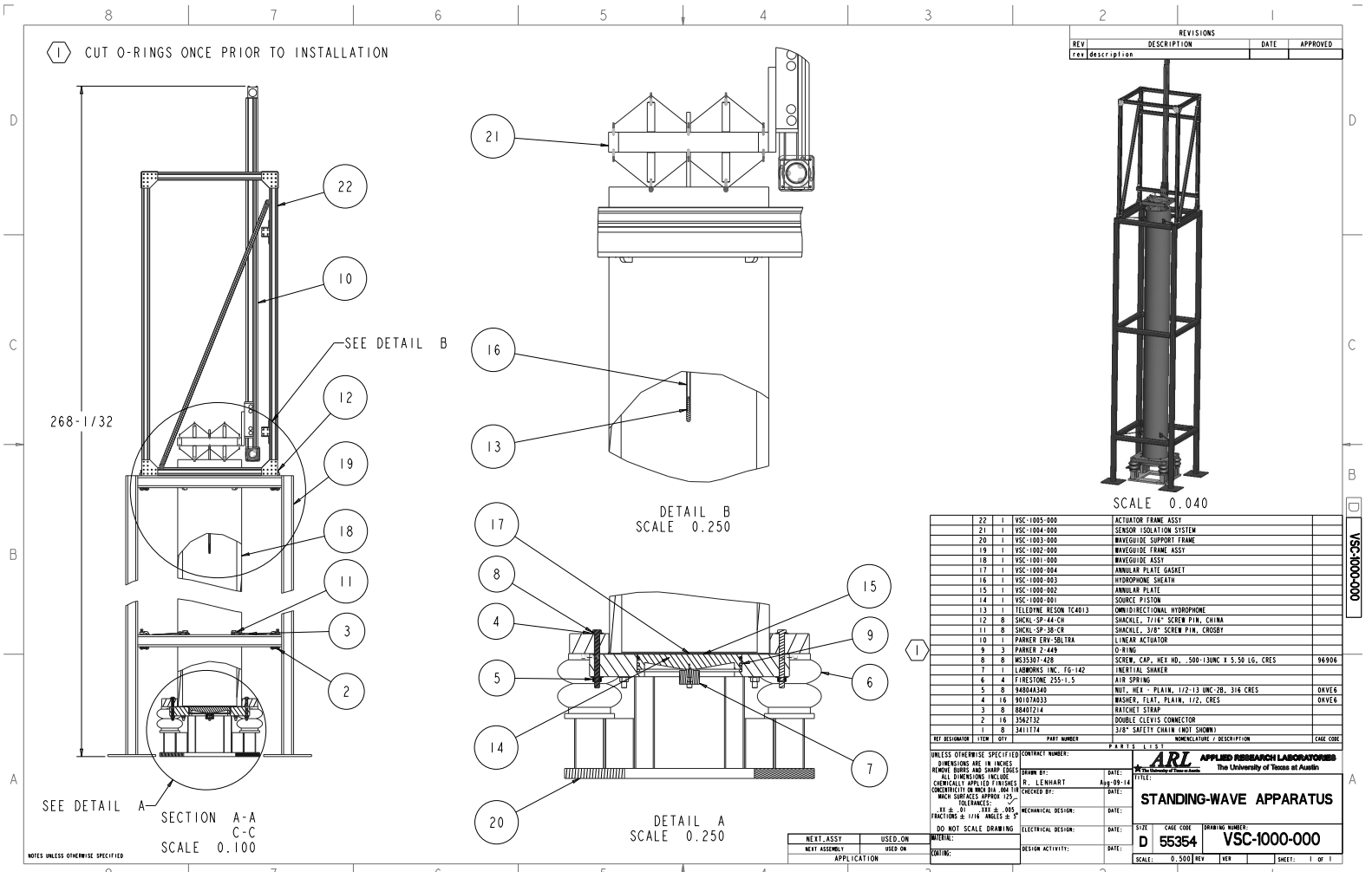

REF DESIGNATOR	ITEM	QTY	PART NUMBER	NOMENCLATURE / DESCRIPTION	CAGE CODE
	22	1	VSC-1005-000	ACTUATOR FRAME ASSY	
	21	1	VSC-1004-000	SENSOR ISOLATION SYSTEM	
	20	1	VSC-1003-000	WAVEGUIDE SUPPORT FRAME	
	19	1	VSC-1002-000	WAVEGUIDE FRAME ASSY	
	18	1	VSC-1001-000	WAVEGUIDE ASSY	
	17	1	VSC-1000-004	ANNULAR PLATE GASKET	
	16	1	VSC-1000-003	HYDROPHONE SHEATH	
	15	1	VSC-1000-002	ANNULAR PLATE	
	14	1	VSC-1000-001	SOURCE PISTON	
	13	1	TELEDYNE RESON TC4013	OMNIDIRECTIONAL HYDROPHONE	
	12	8	SHCKL-SP-44-CH	SHACKLE, 7/16" SCREW PIN, CHINA	
	11	8	SHCKL-SP-38-CR	SHACKLE, 3/8" SCREW PIN, CROSBY	
	10	1	PARKER ERV-5BLTRA	LINEAR ACTUATOR	
	9	3	PARKER 2-449	O-RING	
	8	8	MS35307-428	SCREW, CAP, HEX HD, .500-13UNC X 5.50 LG, CRES	96906
	7	1	LABWORKS INC. FG-142	INERTIAL SHAKER	
	6	4	FIRESTONE 255-1.5	AIR SPRING	
	5	8	94804A340	NUT, HEX - PLAIN, 1/2-13 UNC-2B, 316 CRES	OKVE6
	4	16	90107A033	WASHER, FLAT, PLAIN, 1/2, CRES	OKVE6
	3	8	88407214	RATCHET STRAP	
	2	16	3562T32	DOUBLE CLEVIS CONNECTOR	
	1	8	3411T74	3/8" SAFETY CHAIN (NOT SHOWN)	

PARTS LIST

UNLESS OTHERWISE SPECIFIED
DIMENSIONS ARE IN INCHES
REMOVE BURRS AND SHARP EDGES
ALL DIMENSIONS INCLUDE CHEMICALLY APPLIED FINISHES
CONCENTRICITY ON MACH DIA .004 TIR
MACH SURFACES APPROX 125
TOLERANCES:
.XX ± .01 .XXX ± .005
FRACTIONS ± 1/16' ANGLES ± 5°
DO NOT SCALE DRAWING

CONTRACT NUMBER:
DRAWN BY: R. LENHART DATE: Aug-09-14
CHECKED BY: DATE:
MECHANICAL DESIGN: DATE:
ELECTRICAL DESIGN: DATE:
DESIGN ACTIVITY: DATE:
MATERIAL:
COATING:

NEXT ASSY | USED ON
NEXT ASSEMBLY | USED ON
APPLICATION

APPLIED RESEARCH LABORATORIES
The University of Texas at Austin

TITLE: STANDING-WAVE APPARATUS

SIZE D | CAGE CODE 55354 | DRAWING NUMBER: VSC-1000-000

SCALE: 0.500 | REV | VER | SHEET: 1 OF 1

REVISIONS			
REV	DESCRIPTION	DATE	APPROVED
rev	description		

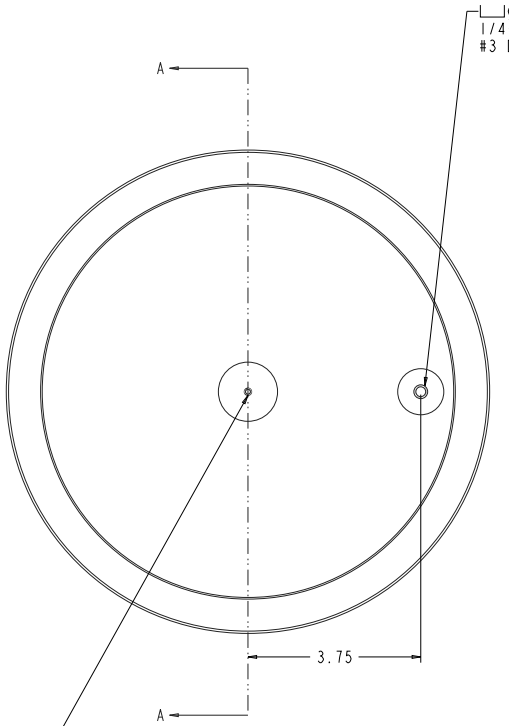

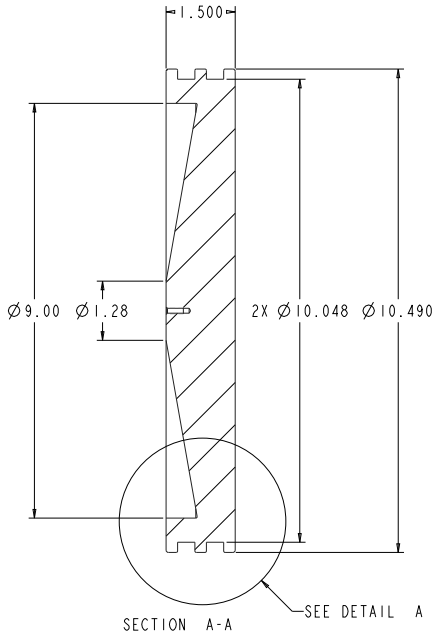

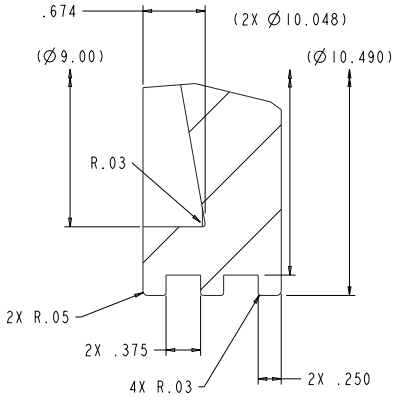

DETAIL A
SCALE 2.000

VSC-1000-001

NOTES UNLESS OTHERWISE SPECIFIED

REF DESIGNATOR	ITEM	QTY	PART NUMBER	NOMENCLATURE / DESCRIPTION	CAGE CODE

PARTS LIST

NEXT ASSY	USED ON
NEXT ASSEMBLY	USED ON
APPLICATION	

UNLESS OTHERWISE SPECIFIED
DIMENSIONS ARE IN INCHES
REMOVE BURRS AND SHARP EDGES
ALL DIMENSIONS INCLUDE CHEMICALLY APPLIED FINISHES
CONCENTRICITY ON MACH DIA .004 TIR
MACH SURFACES APPROX 125
TOLERANCES:
.XX ± .01 .XXX ± .005
FRACTIONS ± 1/16 ANGLES ± 5°
DO NOT SCALE DRAWING

MATERIAL: 6061-T6 AL
COATING: NONE

CONTRACT NUMBER:
DRAWN BY: R. LENHART DATE: Aug-09-14
CHECKED BY: DATE:
MECHANICAL DESIGN: DATE:
ELECTRICAL DESIGN: DATE:
DESIGN ACTIVITY: DATE:

ARL APPLIED RESEARCH LABORATORIES
The University of Texas at Austin

TITLE: SOURCE PISTON

SIZE	CAGE CODE	DRAWING NUMBER
D	55354	VSC-1000-001

SCALE: 1.000 REV VER SHEET: 1 OF 1

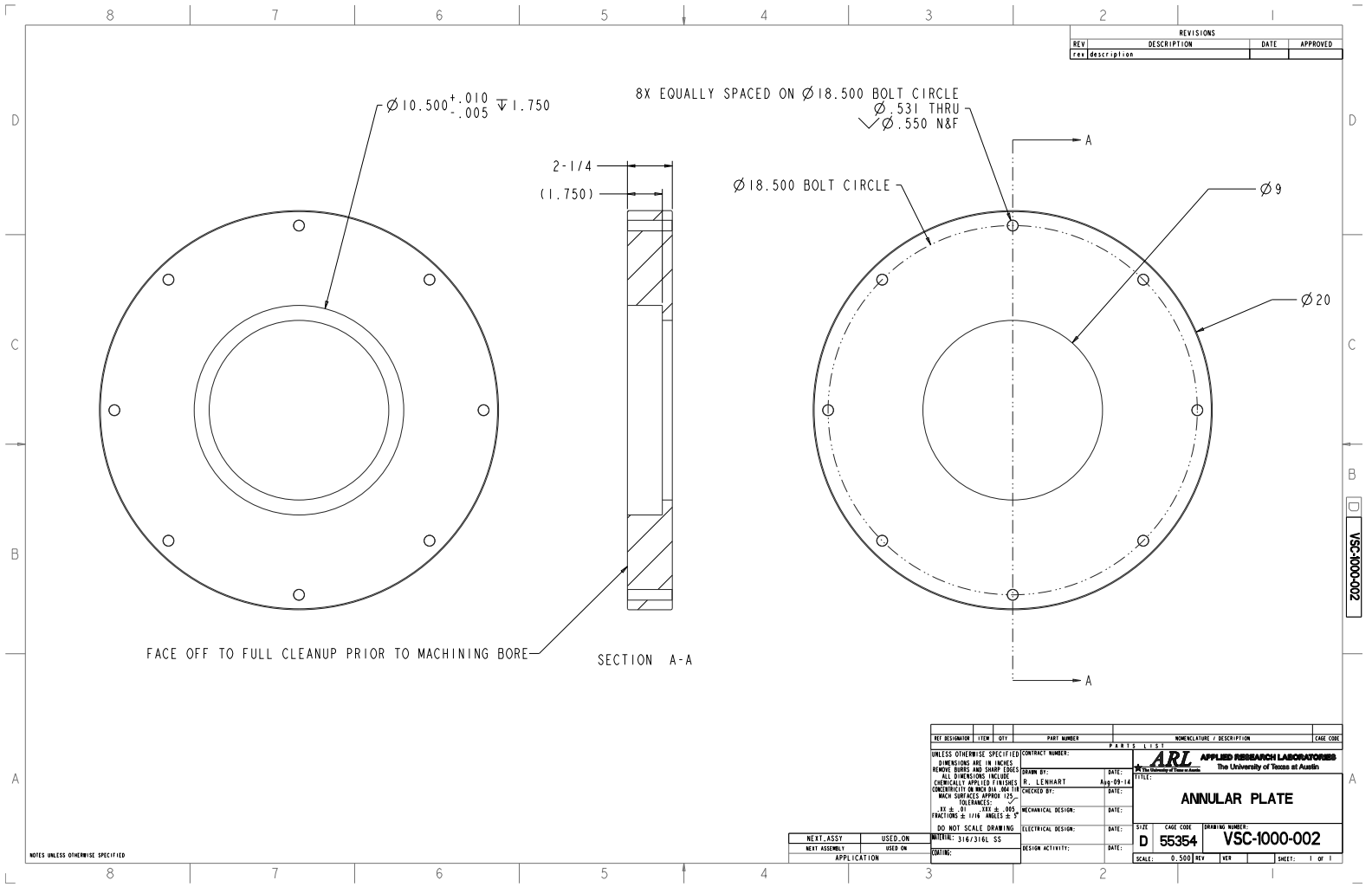
REVISIONS
REV | DESCRIPTION | DATE | APPROVED
rev | description
Ø10.500 +.010 -.005 ↧1.750
8X EQUALLY SPACED ON Ø18.500 BOLT CIRCLE
Ø.531 THRU
Ø.550 N&F
2-1/4
(1.750)
Ø18.500 BOLT CIRCLE
Ø9
Ø20
A
A
FACE OFF TO FULL CLEANUP PRIOR TO MACHINING BORE
SECTION A-A
VSC-1000-002
REF DESIGNATOR | ITEM | QTY | PART NUMBER | NOMENCLATURE / DESCRIPTION | CAGE CODE
PARTS LIST
UNLESS OTHERWISE SPECIFIED
DIMENSIONS ARE IN INCHES
REMOVE BURRS AND SHARP EDGES
ALL DIMENSIONS INCLUDE CHEMICALLY APPLIED FINISHES
CONCENTRICITY ON MACH DIA .004 TIR
MACH SURFACES APPROX 125
TOLERANCES:
.XX ± .01 .XXX ± .005
FRACTIONS ± 1/16 ANGLES ± 5°
DO NOT SCALE DRAWING
CONTRACT NUMBER:
DRAWN BY: R. LENHART DATE: Aug-09-14
CHECKED BY: DATE:
MECHANICAL DESIGN: DATE:
ELECTRICAL DESIGN: DATE:
DESIGN ACTIVITY: DATE:
MATERIAL: 316/316L SS
COATING:
NEXT ASSY | USED ON
NEXT ASSEMBLY | USED ON
APPLICATION
ARL APPLIED RESEARCH LABORATORIES
The University of Texas at Austin
TITLE:
ANNULAR PLATE
SIZE D | CAGE CODE 55354 | DRAWING NUMBER: VSC-1000-002
SCALE: 0.500 | REV | VER | SHEET: 1 OF 1
NOTES UNLESS OTHERWISE SPECIFIED

REVISIONS			
REV	DESCRIPTION	DATE	APPROVED
rev	description		

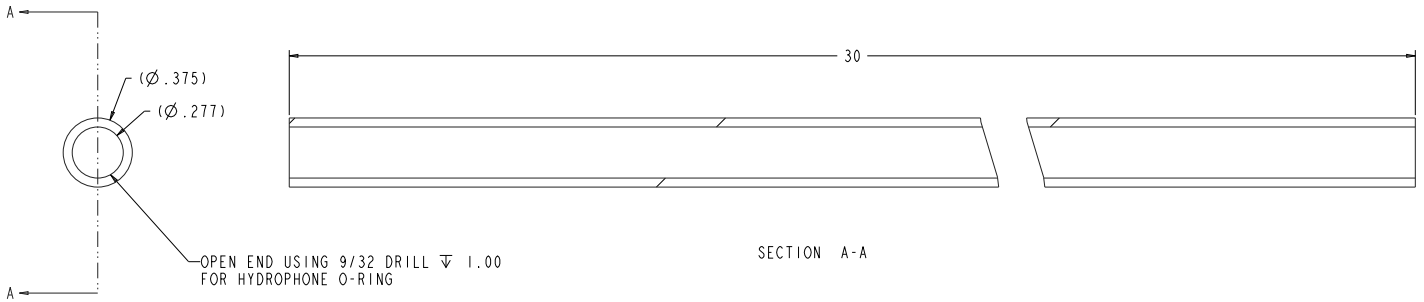

REF DESIGNATOR	ITEM	QTY	PART NUMBER	NOMENCLATURE / DESCRIPTION	CAGE CODE

PARTS LIST

UNLESS OTHERWISE SPECIFIED
DIMENSIONS ARE IN INCHES
REMOVE BURRS AND SHARP EDGES
ALL DIMENSIONS INCLUDE CHEMICALLY APPLIED FINISHES
CONCENTRICITY ON MACH DIA .004 TIR
MACH SURFACES APPROX 125
TOLERANCES:
.XX ± .01 .XXX ± .005
FRACTIONS ± 1/16 ANGLES ± 5°
DO NOT SCALE DRAWING

MATERIAL: 316/316 SS
COATING:

NEXT ASSY	USED ON
NEXT ASSEMBLY	USED ON
APPLICATION	

CONTRACT NUMBER:

	DATE:
DRAWN BY: R. LENHART	Aug-09-14
CHECKED BY:	
MECHANICAL DESIGN:	
ELECTRICAL DESIGN:	
DESIGN ACTIVITY:	

ARL APPLIED RESEARCH LABORATORIES
The University of Texas at Austin

TITLE: HYDROPHONE SHEATH

SIZE	CAGE CODE	DRAWING NUMBER
D	55354	VSC-1000-003

SCALE: 4.000 | REV | VER | SHEET: 1 OF 1

NOTES UNLESS OTHERWISE SPECIFIED

VSC-1000-003

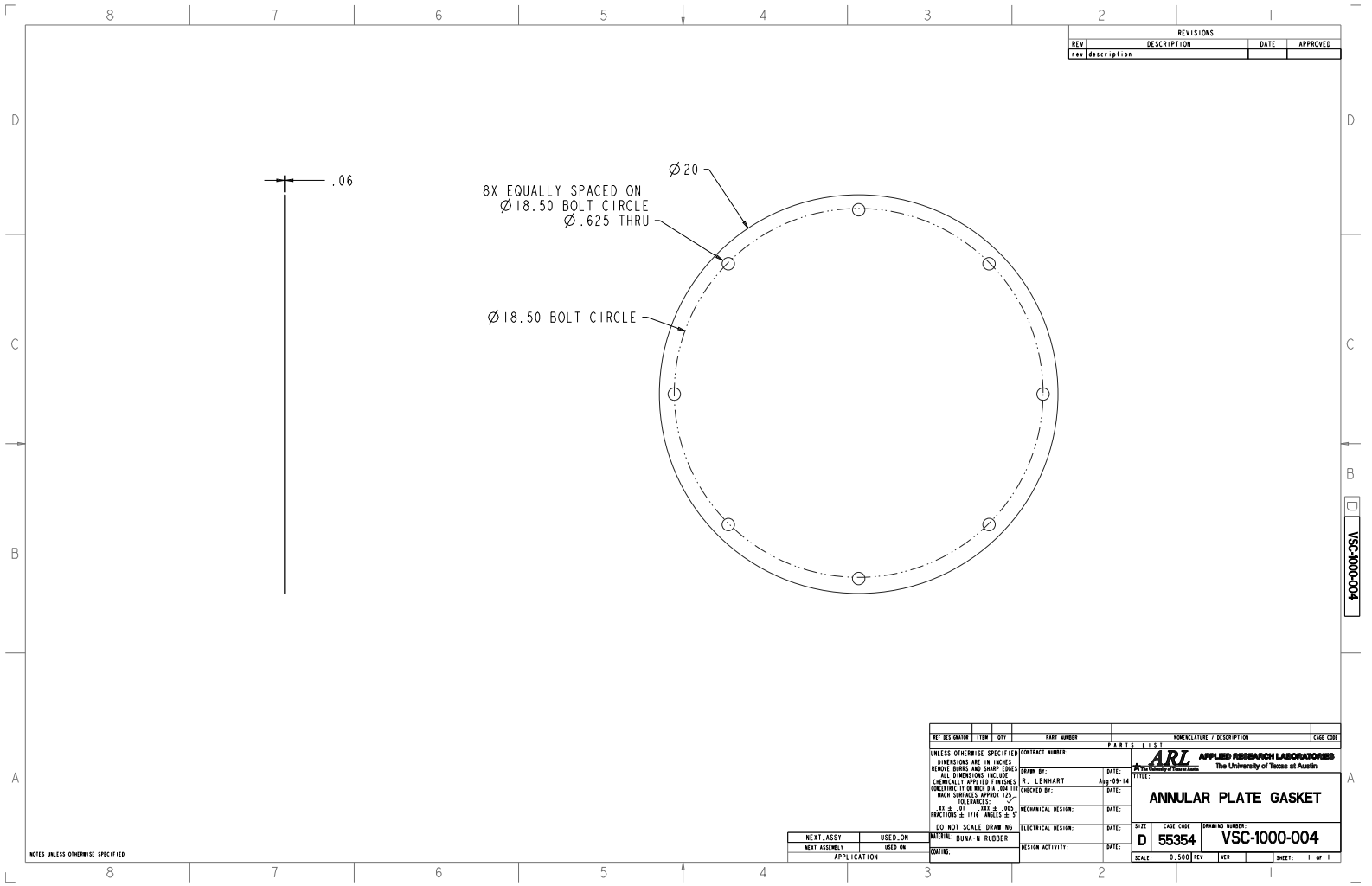

REVISIONS			
REV	DESCRIPTION	DATE	APPROVED
rev	description		

REF DESIGNATOR	ITEM	QTY	PART NUMBER	NOMENCLATURE / DESCRIPTION	CAGE CODE

PARTS LIST

UNLESS OTHERWISE SPECIFIED
DIMENSIONS ARE IN INCHES
REMOVE BURRS AND SHARP EDGES
ALL DIMENSIONS INCLUDE CHEMICALLY APPLIED FINISHES
CONCENTRICITY ON MACH DIA .004 TIR
MACH SURFACES APPROX 125
TOLERANCES:
.XX ± .01 .XXX ± .005
FRACTIONS ± 1/16 ANGLES ± 5°
DO NOT SCALE DRAWING

CONTRACT NUMBER:
DRAWN BY: R. LENHART DATE: Aug-09-14
CHECKED BY: DATE:
MECHANICAL DESIGN: DATE:
ELECTRICAL DESIGN: DATE:
DESIGN ACTIVITY: DATE:

MATERIAL: BUNA-N RUBBER
COATING:

NEXT ASSY | USED ON
NEXT ASSEMBLY | USED ON
APPLICATION

ARL APPLIED RESEARCH LABORATORIES
The University of Texas at Austin

TITLE: ANNULAR PLATE GASKET

SIZE	CAGE CODE	DRAWING NUMBER
D	55354	VSC-1000-004

SCALE: 0.500 | REV | VER | SHEET: 1 OF 1

NOTES UNLESS OTHERWISE SPECIFIED

VSC-1000-004

D.2 Waveguide Assembly

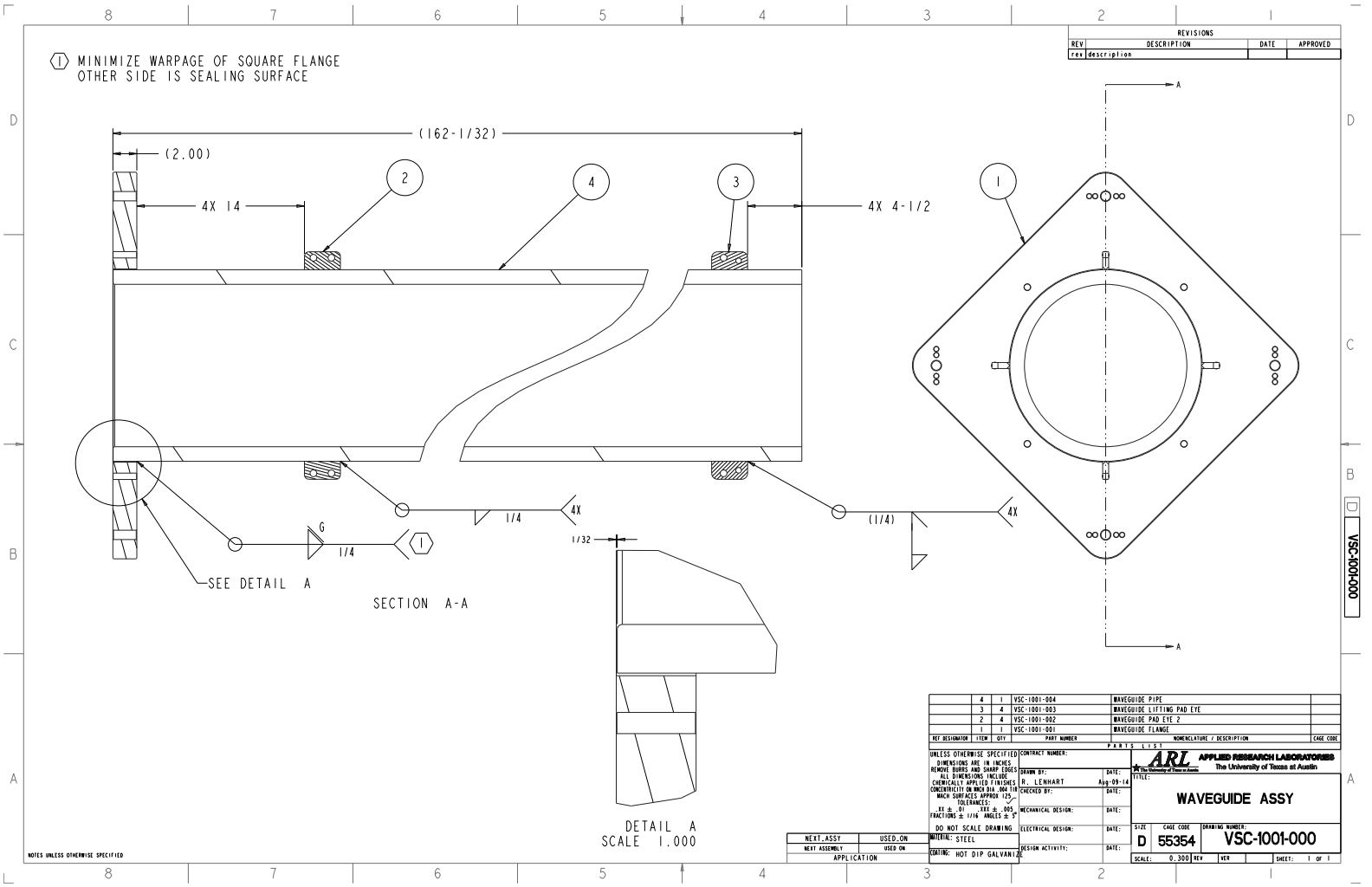

REF DESIGNATOR	ITEM	QTY	PART NUMBER	NOMENCLATURE / DESCRIPTION	CAGE CODE
	4	1	VSC-1001-004	WAVEGUIDE PIPE	
	3	4	VSC-1001-003	WAVEGUIDE LIFTING PAD EYE	
	2	4	VSC-1001-002	WAVEGUIDE PAD EYE 2	
	1	1	VSC-1001-001	WAVEGUIDE FLANGE	

PARTS LIST

NEXT ASSY	USED ON
NEXT ASSEMBLY	USED ON
APPLICATION	

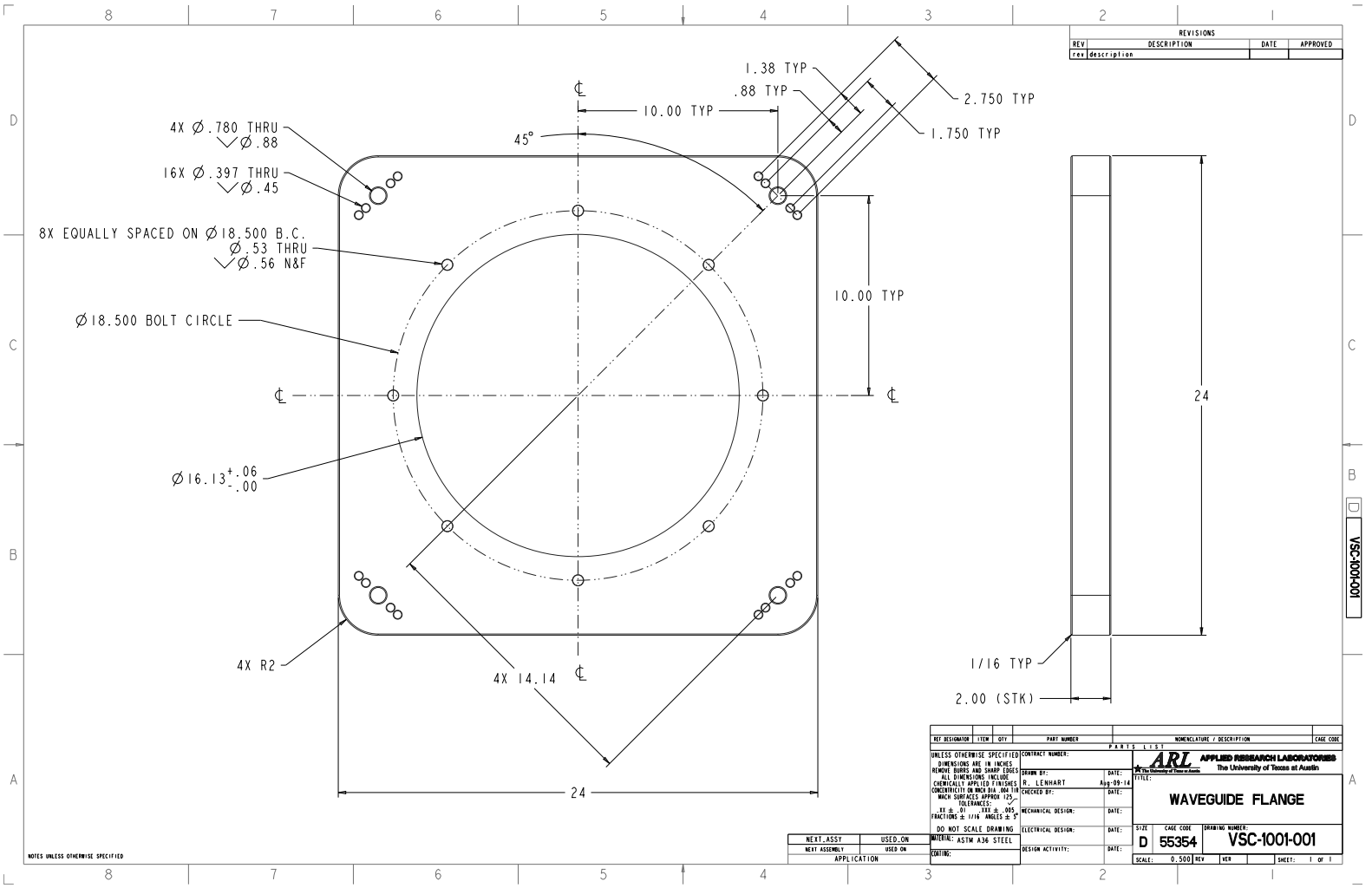
REVISIONS
REV | DESCRIPTION | DATE | APPROVED
rev | description
1.38 TYP
.88 TYP
2.750 TYP
1.750 TYP
10.00 TYP
45°
4X Ø.780 THRU
Ø.88
16X Ø.397 THRU
Ø.45
8X EQUALLY SPACED ON Ø18.500 B.C.
Ø.53 THRU
Ø.56 N&F
Ø18.500 BOLT CIRCLE
10.00 TYP
Ø16.13 +.06 -.00
4X R2
4X 14.14
24
24
1/16 TYP
2.00 (STK)
VSC-1001-001
REF DESIGNATOR | ITEM | QTY | PART NUMBER | NOMENCLATURE / DESCRIPTION | CAGE CODE
PARTS LIST
UNLESS OTHERWISE SPECIFIED
DIMENSIONS ARE IN INCHES
REMOVE BURRS AND SHARP EDGES
ALL DIMENSIONS INCLUDE CHEMICALLY APPLIED FINISHES
CONCENTRICITY ON INDICATED DIA. .004 TIR
MACH SURFACES APPROX 125
TOLERANCES:
.XX ± .01 .XXX ± .005
FRACTIONS ± 1/16' ANGLES ± 5°
DO NOT SCALE DRAWING
CONTRACT NUMBER:
DRAWN BY: R. LENHART DATE: Aug-09-14
CHECKED BY: DATE:
MECHANICAL DESIGN: DATE:
ELECTRICAL DESIGN: DATE:
DESIGN ACTIVITY: DATE:
MATERIAL: ASTM A36 STEEL
COATING:
NEXT ASSY | USED ON
NEXT ASSEMBLY | USED ON
APPLICATION
ARL APPLIED RESEARCH LABORATORIES
The University of Texas at Austin
TITLE:
WAVEGUIDE FLANGE
SIZE D | CAGE CODE 55354 | DRAWING NUMBER: VSC-1001-001
SCALE: 0.500 | REV | VER | SHEET: 1 OF 1
NOTES UNLESS OTHERWISE SPECIFIED

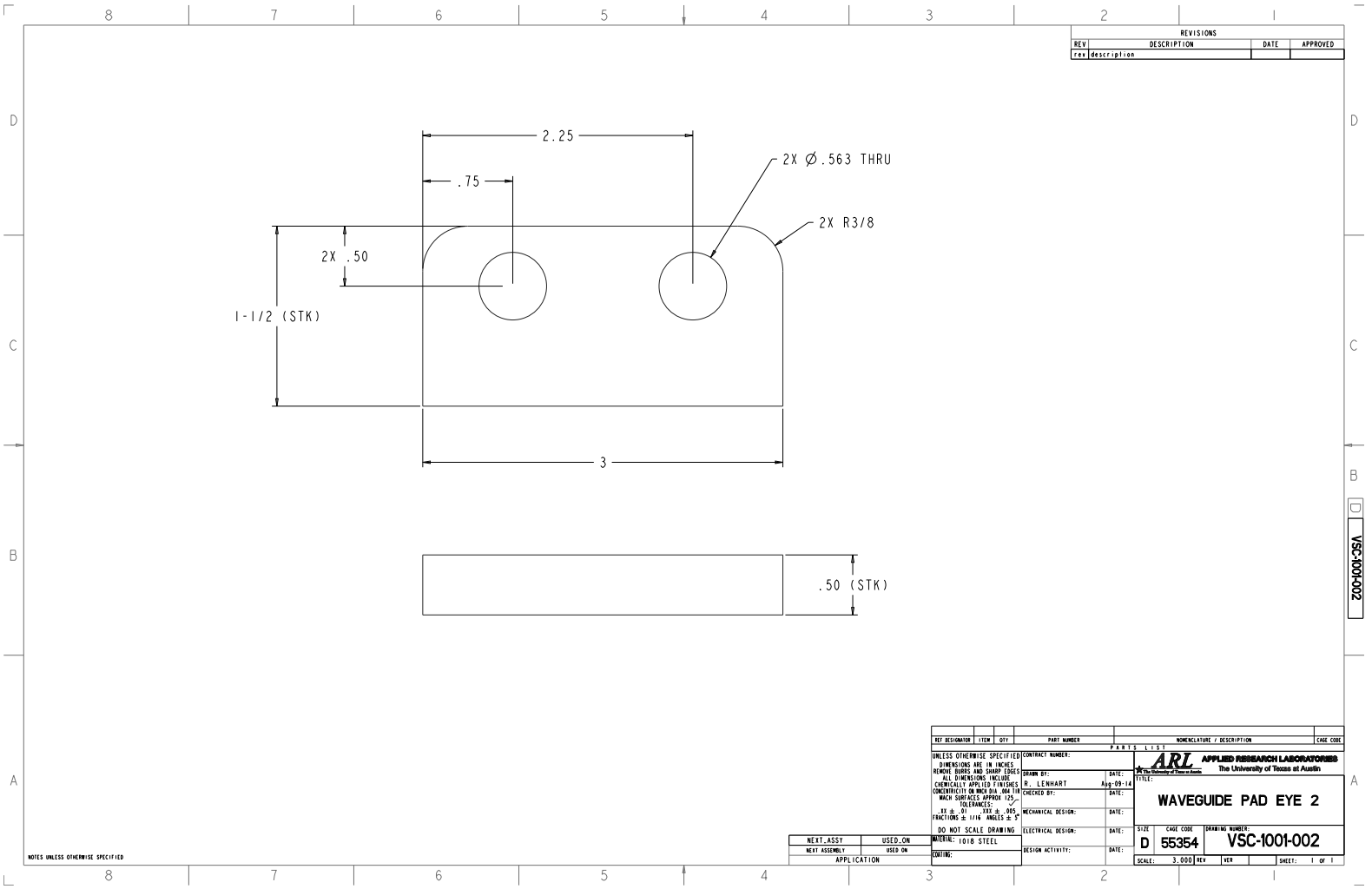
REVISIONS
REV
DESCRIPTION
DATE
APPROVED
rev
description
2.25
.75
2X Ø.563 THRU
2X R3/8
2X .50
1-1/2 (STK)
3
.50 (STK)
VSC-1001-002
REF DESIGNATOR
ITEM
QTY
PART NUMBER
NOMENCLATURE / DESCRIPTION
CAGE CODE
PARTS LIST
UNLESS OTHERWISE SPECIFIED
DIMENSIONS ARE IN INCHES
REMOVE BURRS AND SHARP EDGES
ALL DIMENSIONS INCLUDE CHEMICALLY APPLIED FINISHES
CONCENTRICITY ON INNER DIA .004 TIR
MACH SURFACES APPROX 125
TOLERANCES:
.XX ± .01 .XXX ± .005
FRACTIONS ± 1/16 ANGLES ± 5°
DO NOT SCALE DRAWING
CONTRACT NUMBER:
DRAWN BY:
R. LENHART
DATE:
Aug-09-14
CHECKED BY:
MECHANICAL DESIGN:
ELECTRICAL DESIGN:
DESIGN ACTIVITY:
ARL
APPLIED RESEARCH LABORATORIES
The University of Texas at Austin
TITLE:
WAVEGUIDE PAD EYE 2
SIZE
D
CAGE CODE
55354
DRAWING NUMBER:
VSC-1001-002
SCALE: 3.000
REV
VER
SHEET: 1 OF 1
NEXT ASSY
USED ON
NEXT ASSEMBLY
USED ON
APPLICATION
MATERIAL: 1018 STEEL
COATING:
NOTES UNLESS OTHERWISE SPECIFIED

MINIMUM MATERIAL YIELD STRENGTH: 54000 PSI

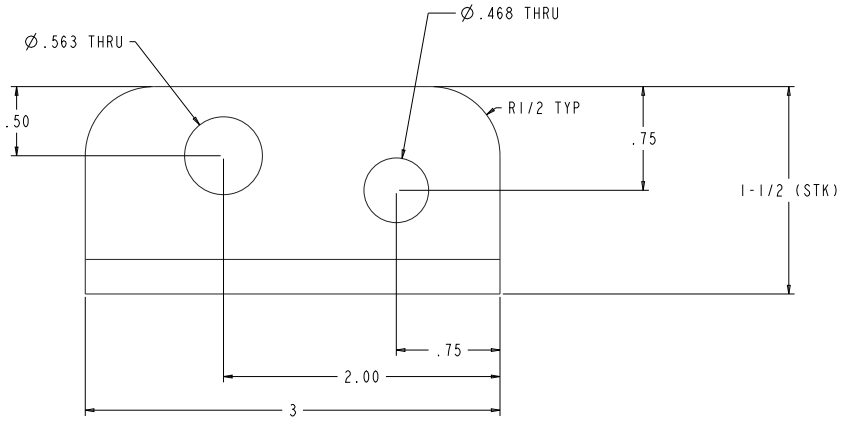

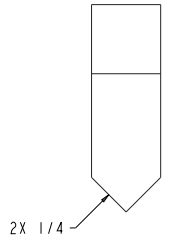

REVISIONS			
REV	DESCRIPTION	DATE	APPROVED
rev	description		

REF DESIGNATOR	ITEM	QTY	PART NUMBER	NOMENCLATURE / DESCRIPTION	CAGE CODE

PARTS LIST

UNLESS OTHERWISE SPECIFIED
DIMENSIONS ARE IN INCHES
REMOVE BURRS AND SHARP EDGES
ALL DIMENSIONS INCLUDE CHEMICALLY APPLIED FINISHES
CONCENTRICITY ON INDICATED DIA. .004 TIR
MACH SURFACES APPROX 125
TOLERANCES:
.XX ± .01 .XXX ± .005
FRACTIONS ± 1/16 ANGLES ± 5°
DO NOT SCALE DRAWING

CONTRACT NUMBER:
DRAWN BY: R. LENHART DATE: Aug-09-14
CHECKED BY: DATE:
MECHANICAL DESIGN: DATE:
ELECTRICAL DESIGN: DATE:
DESIGN ACTIVITY: DATE:

MATERIAL: AISI 1018 STEEL
COATING:

NEXT ASSY | USED ON
NEXT ASSEMBLY | USED ON
APPLICATION

ARL APPLIED RESEARCH LABORATORIES
The University of Texas at Austin

TITLE: WAVEGUIDE LIFTING PAD EYE

SIZE: D | CAGE CODE: 55354 | DRAWING NUMBER: VSC-1001-003

SCALE: 3.000 | REV | VER | SHEET: 1 OF 1

NOTES UNLESS OTHERWISE SPECIFIED

VSC-1001-003

REVISIONS			
REV	DESCRIPTION	DATE	APPROVED
rev	description		

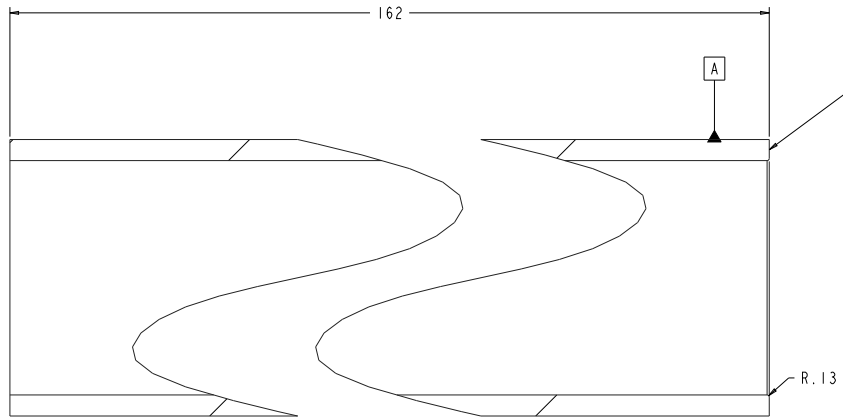

SECTION A-A

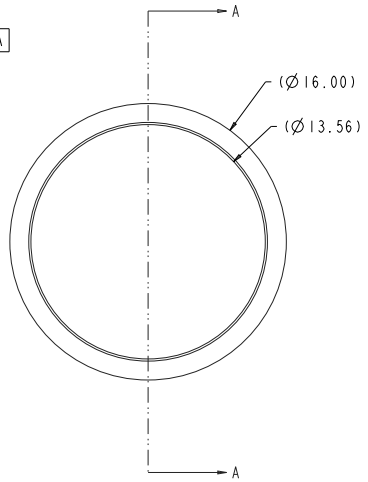

16" SCHEDULE 120 PIPE

VSC-1001-004

REF DESIGNATOR	ITEM	QTY	PART NUMBER	NOMENCLATURE / DESCRIPTION	CAGE CODE

PARTS LIST

UNLESS OTHERWISE SPECIFIED
DIMENSIONS ARE IN INCHES
REMOVE BURRS AND SHARP EDGES
ALL DIMENSIONS INCLUDE CHEMICALLY APPLIED FINISHES
CONCENTRICITY ON INDICATED DIA. .004 TIR
MACH SURFACES APPROX 125
TOLERANCES:
.XX ± .01 .XXX ± .005
FRACTIONS ± 1/16 ANGLES ± 5°
DO NOT SCALE DRAWING

CONTRACT NUMBER:
DRAWN BY: R. LENHART DATE: Aug-09-14
CHECKED BY: DATE:
MECHANICAL DESIGN: DATE:
ELECTRICAL DESIGN: DATE:
DESIGN ACTIVITY: DATE:

MATERIAL: ASTM A106
COATING:

NEXT ASSY	USED ON
NEXT ASSEMBLY	USED ON
APPLICATION	

ARL APPLIED RESEARCH LABORATORIES
The University of Texas at Austin

TITLE: WAVEGUIDE PIPE

SIZE	CAGE CODE	DRAWING NUMBER
D	55354	VSC-1001-004

SCALE: 0.375 REV VER SHEET: 1 OF 1

NOTES UNLESS OTHERWISE SPECIFIED

D.3 Waveguide Frame Assembly

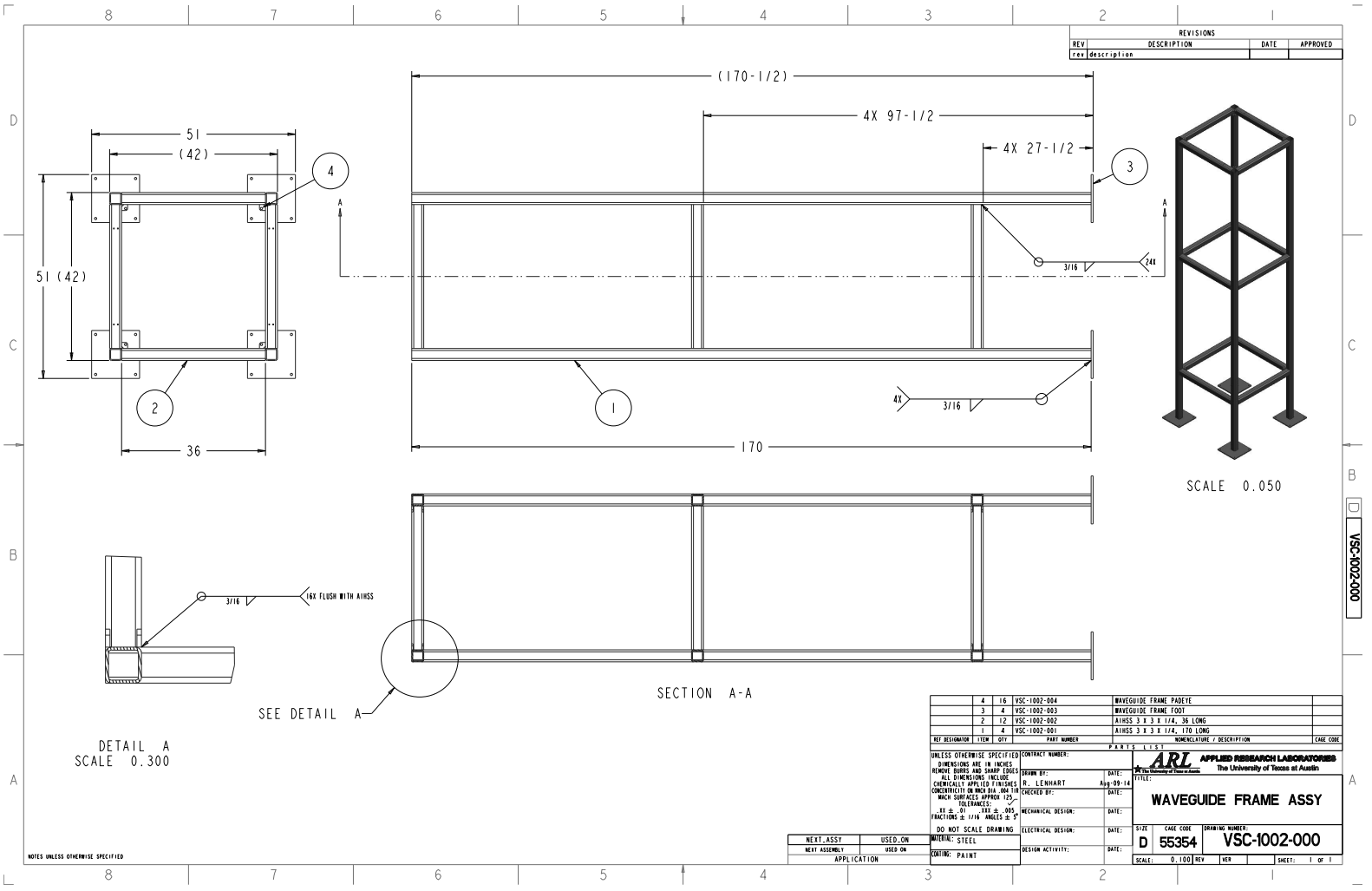
REVISIONS
REV DESCRIPTION DATE APPROVED
rev description
(170-1/2)
4X 97-1/2
4X 27-1/2
51
(42)
51 (42)
36
170
3/16
24X
4X
3/16
SCALE 0.050
3/16
16X FLUSH WITH AIHSS
DETAIL A
SCALE 0.300
SEE DETAIL A
SECTION A-A
4 16 VSC-1002-004 WAVEGUIDE FRAME PADEYE
3 4 VSC-1002-003 WAVEGUIDE FRAME FOOT
2 12 VSC-1002-002 AIHSS 3 X 3 X 1/4, 36 LONG
1 4 VSC-1002-001 AIHSS 3 X 3 X 1/4, 170 LONG
REF DESIGNATOR ITEM QTY PART NUMBER NOMENCLATURE / DESCRIPTION CAGE CODE
PARTS LIST
UNLESS OTHERWISE SPECIFIED
DIMENSIONS ARE IN INCHES
REMOVE BURRS AND SHARP EDGES
ALL DIMENSIONS INCLUDE CHEMICALLY APPLIED FINISHES
CONCENTRICITY ON MACH DIA .004 TIR
MACH SURFACES APPROX 125
TOLERANCES:
.XX ± .01 .XXX ± .005
FRACTIONS ± 1/16 ANGLES ± 5°
DO NOT SCALE DRAWING
CONTRACT NUMBER:
DRAWN BY: R. LENHART DATE: Aug-09-14
CHECKED BY: DATE:
MECHANICAL DESIGN: DATE:
ELECTRICAL DESIGN: DATE:
DESIGN ACTIVITY: DATE:
MATERIAL: STEEL
COATING: PAINT
NEXT_ASSY USED_ON
NEXT ASSEMBLY USED ON
APPLICATION
ARL APPLIED RESEARCH LABORATORIES
The University of Texas at Austin
TITLE:
WAVEGUIDE FRAME ASSY
SIZE D
CAGE CODE 55354
DRAWING NUMBER: VSC-1002-000
SCALE: 0.100 REV VER SHEET: 1 OF 1
NOTES UNLESS OTHERWISE SPECIFIED
VSC-1002-000

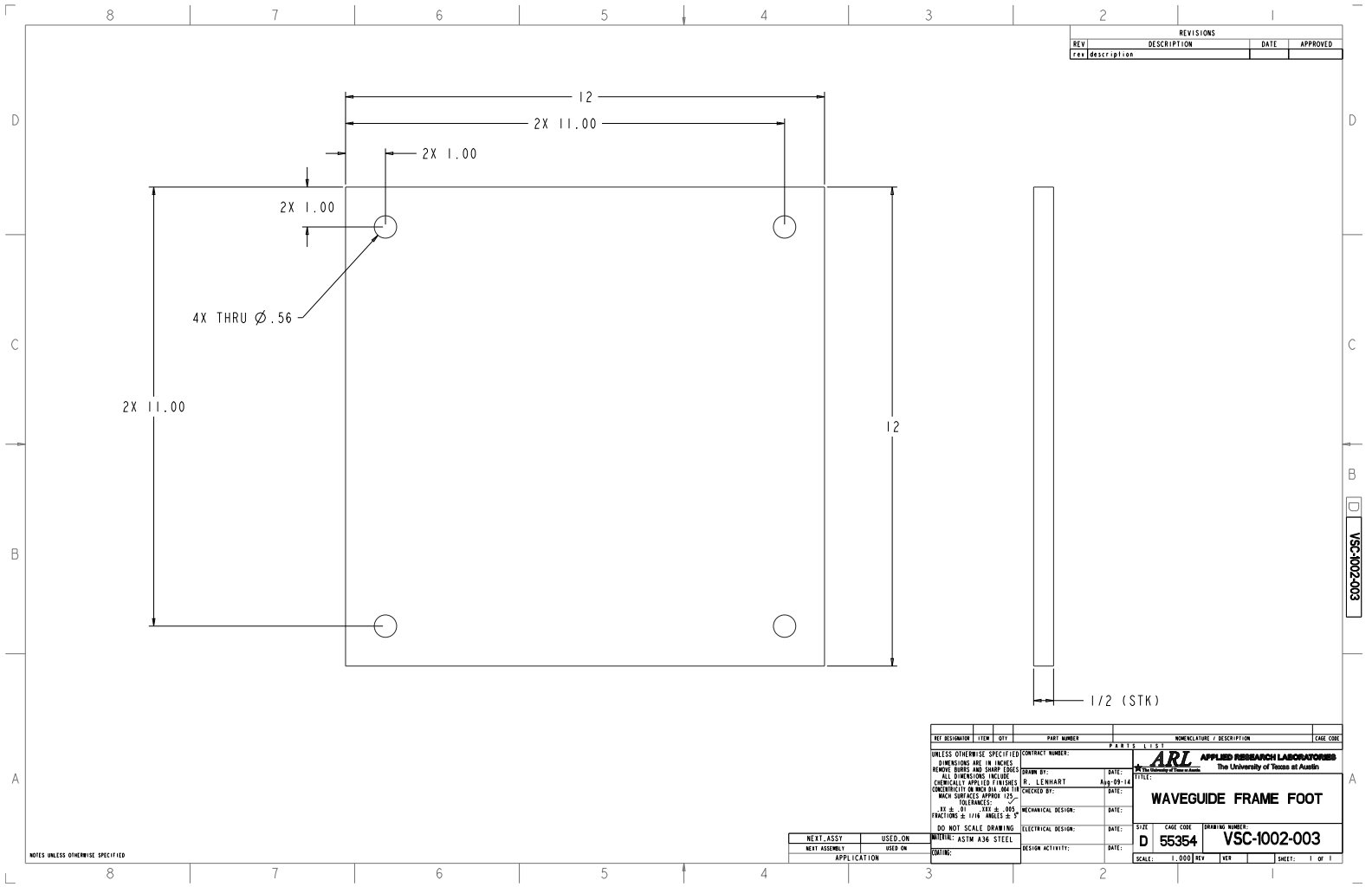
REVISIONS
REV | DESCRIPTION | DATE | APPROVED
rev | description
12
2X 11.00
2X 1.00
2X 1.00
4X THRU Ø.56
2X 11.00
12
1/2 (STK)
VSC-1002-003
REF DESIGNATOR | ITEM | QTY | PART NUMBER | NOMENCLATURE / DESCRIPTION | CAGE CODE
PARTS LIST
UNLESS OTHERWISE SPECIFIED
DIMENSIONS ARE IN INCHES
REMOVE BURRS AND SHARP EDGES
ALL DIMENSIONS INCLUDE CHEMICALLY APPLIED FINISHES
CONCENTRICITY ON INDICATED DIA. .004 TIR
MACH SURFACES APPROX 125
TOLERANCES:
.XX ± .01 XXX ± .005
FRACTIONS ± 1/16 ANGLES ± 5°
DO NOT SCALE DRAWING
CONTRACT NUMBER:
DRAWN BY: R. LENHART
DATE: Aug-09-14
CHECKED BY:
MECHANICAL DESIGN:
ELECTRICAL DESIGN:
DESIGN ACTIVITY:
MATERIAL: ASTM A36 STEEL
COATING:
NEXT ASSY | USED ON
NEXT ASSEMBLY | USED ON
APPLICATION
ARL APPLIED RESEARCH LABORATORIES
The University of Texas at Austin
TITLE:
WAVEGUIDE FRAME FOOT
SIZE D | CAGE CODE 55354 | DRAWING NUMBER: VSC-1002-003
SCALE: 1.000 | REV | VER | SHEET: 1 OF 1
NOTES UNLESS OTHERWISE SPECIFIED

REVISIONS			
REV	DESCRIPTION	DATE	APPROVED
rev	description		

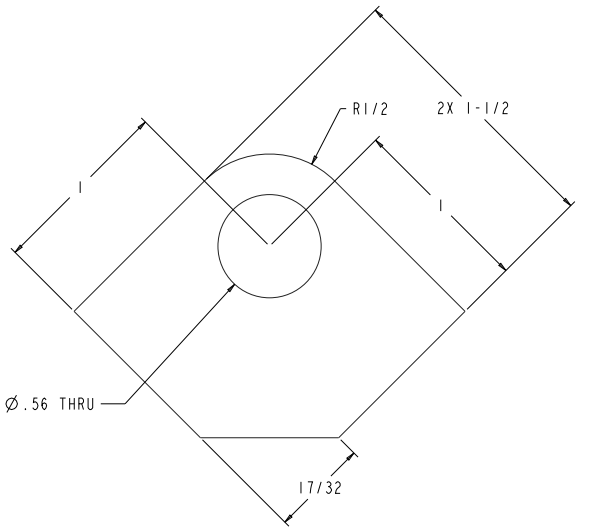

REF DESIGNATOR	ITEM	QTY	PART NUMBER	NOMENCLATURE / DESCRIPTION	CAGE CODE

PARTS LIST

UNLESS OTHERWISE SPECIFIED
DIMENSIONS ARE IN INCHES
REMOVE BURRS AND SHARP EDGES
ALL DIMENSIONS INCLUDE CHEMICALLY APPLIED FINISHES
CONCENTRICITY ON INNER DIA .004 TIR
MACH SURFACES APPROX 125
TOLERANCES:
.XX ± .01 .XXX ± .005
FRACTIONS ± 1/16 ANGLES ± 5°
DO NOT SCALE DRAWING

CONTRACT NUMBER:

DRAWN BY: R. LENHART DATE: Aug-09-14
CHECKED BY: DATE:
MECHANICAL DESIGN: DATE:
ELECTRICAL DESIGN: DATE:
DESIGN ACTIVITY: DATE:

MATERIAL: ASTM A36 STEEL
COATING:

ARL APPLIED RESEARCH LABORATORIES
The University of Texas at Austin

TITLE: WAVEGUIDE FRAME PAD EYE

SIZE	CAGE CODE	DRAWING NUMBER:
D	55354	VSC-1002-004

SCALE: 4.000 REV VER SHEET: 1 OF 1

NEXT_ASSY	USED_ON
NEXT ASSEMBLY	USED ON
APPLICATION	

NOTES UNLESS OTHERWISE SPECIFIED

VSC-1002-004

D.4 Waveguide Support Frame Assembly

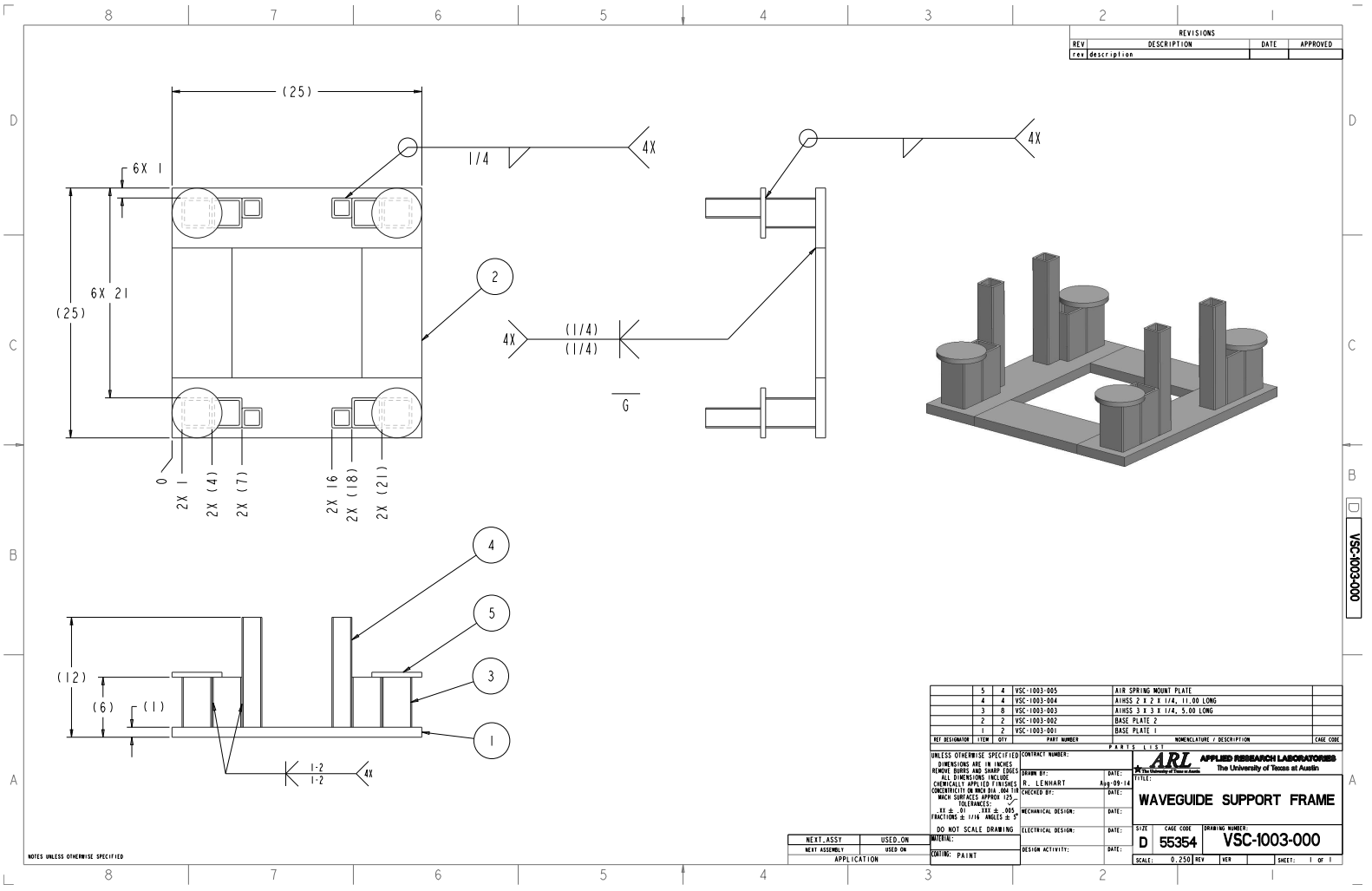
REVISIONS
REV | DESCRIPTION | DATE | APPROVED
rev | description
(25)
6X 1
6X 21
(25)
1/4
4X
2
(1/4)
(1/4)
G
0
2X 1
2X (4)
2X (7)
2X 16
2X (18)
2X (21)
4
5
3
1
(12)
(6)
(1)
1-2
1-2
4X
5 | 4 | VSC-1003-005 | AIR SPRING MOUNT PLATE
4 | 4 | VSC-1003-004 | AIHSS 2 X 2 X 1/4, 11.00 LONG
3 | 8 | VSC-1003-003 | AIHSS 3 X 3 X 1/4, 5.00 LONG
2 | 2 | VSC-1003-002 | BASE PLATE 2
1 | 2 | VSC-1003-001 | BASE PLATE 1
REF DESIGNATOR | ITEM | QTY | PART NUMBER | NOMENCLATURE / DESCRIPTION | CAGE CODE
PARTS LIST
UNLESS OTHERWISE SPECIFIED
DIMENSIONS ARE IN INCHES
REMOVE BURRS AND SHARP EDGES
ALL DIMENSIONS INCLUDE CHEMICALLY APPLIED FINISHES
CONCENTRICITY ON MACH DIA .004 TIR
MACH SURFACES APPROX 125
TOLERANCES:
.XX ± .01 XXX ± .005
FRACTIONS ± 1/16 ANGLES ± 5°
DO NOT SCALE DRAWING
CONTRACT NUMBER:
DRAWN BY: R. LENHART
DATE: Aug-09-14
CHECKED BY:
DATE:
MECHANICAL DESIGN:
DATE:
ELECTRICAL DESIGN:
DATE:
DESIGN ACTIVITY:
DATE:
MATERIAL:
COATING: PAINT
NEXT_ASSY | USED_ON
NEXT ASSEMBLY | USED ON
APPLICATION
ARL
APPLIED RESEARCH LABORATORIES
The University of Texas at Austin
TITLE:
WAVEGUIDE SUPPORT FRAME
SIZE: D
CAGE CODE: 55354
DRAWING NUMBER: VSC-1003-000
SCALE: 0.250
REV
VER
SHEET: 1 OF 1
NOTES UNLESS OTHERWISE SPECIFIED
VSC-1003-000

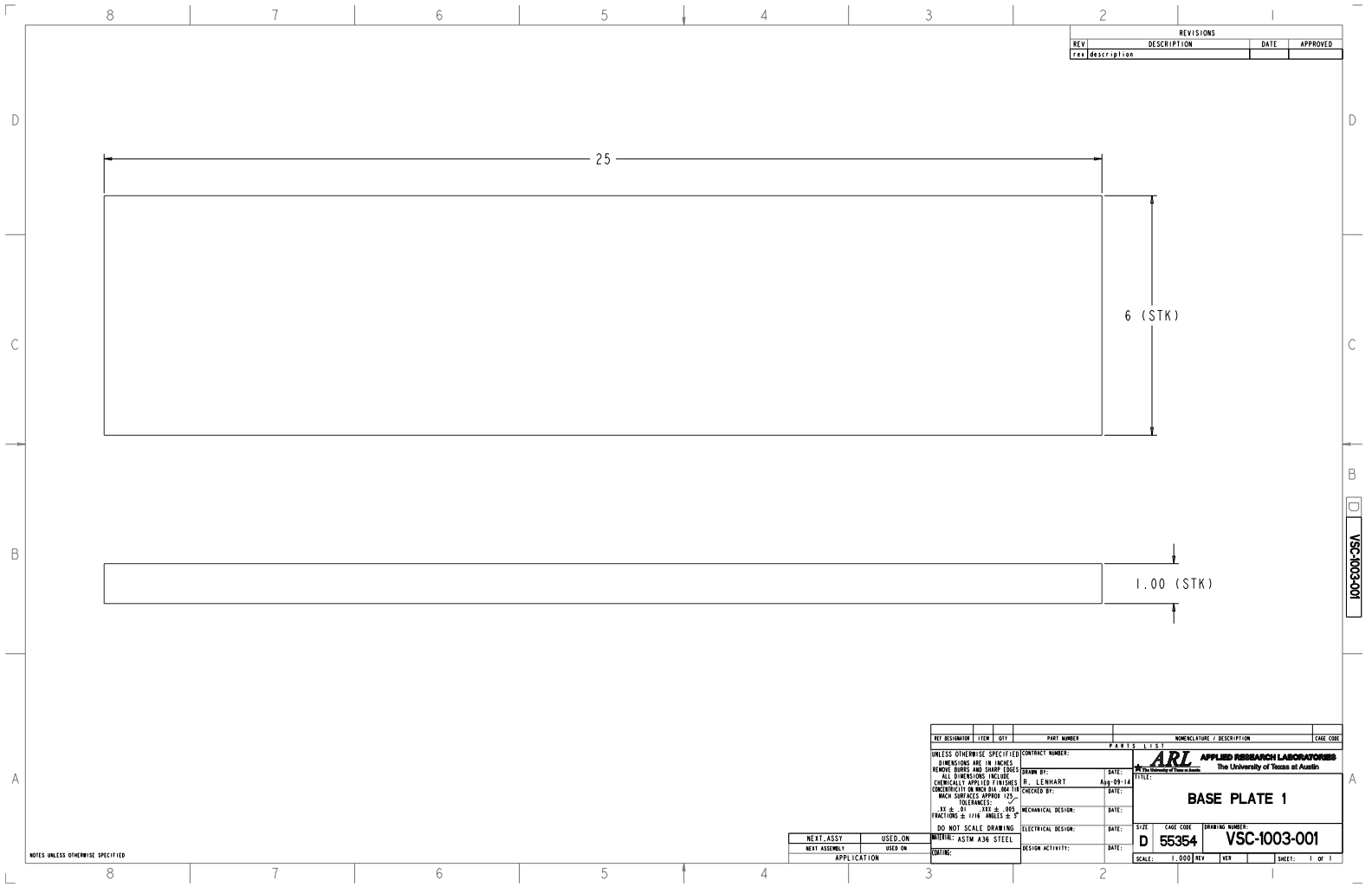
REVISIONS
REV
DESCRIPTION
DATE
APPROVED
rev
description
25
6 (STK)
1.00 (STK)
VSC-1003-001
REF DESIGNATOR
ITEM
QTY
PART NUMBER
NOMENCLATURE / DESCRIPTION
CAGE CODE
PARTS LIST
UNLESS OTHERWISE SPECIFIED
DIMENSIONS ARE IN INCHES
REMOVE BURRS AND SHARP EDGES
ALL DIMENSIONS INCLUDE CHEMICALLY APPLIED FINISHES
CONCENTRICITY ON INNER DIA .004 TIR
MACH SURFACES APPROX 125
TOLERANCES:
.XX ± .01 .XXX ± .005
FRACTIONS ± 1/16 ANGLES ± 5°
DO NOT SCALE DRAWING
MATERIAL: ASTM A36 STEEL
COATING:
CONTRACT NUMBER:
DRAWN BY:
DATE:
R. LENHART
Aug-09-14
CHECKED BY:
DATE:
MECHANICAL DESIGN:
DATE:
ELECTRICAL DESIGN:
DATE:
DESIGN ACTIVITY:
DATE:
ARL
APPLIED RESEARCH LABORATORIES
The University of Texas at Austin
TITLE:
BASE PLATE 1
SIZE
CAGE CODE
DRAWING NUMBER:
D
55354
VSC-1003-001
SCALE: 1.000
REV
VER
SHEET: 1 OF 1
NEXT_ASSY
USED_ON
NEXT ASSEMBLY
USED ON
APPLICATION
NOTES UNLESS OTHERWISE SPECIFIED

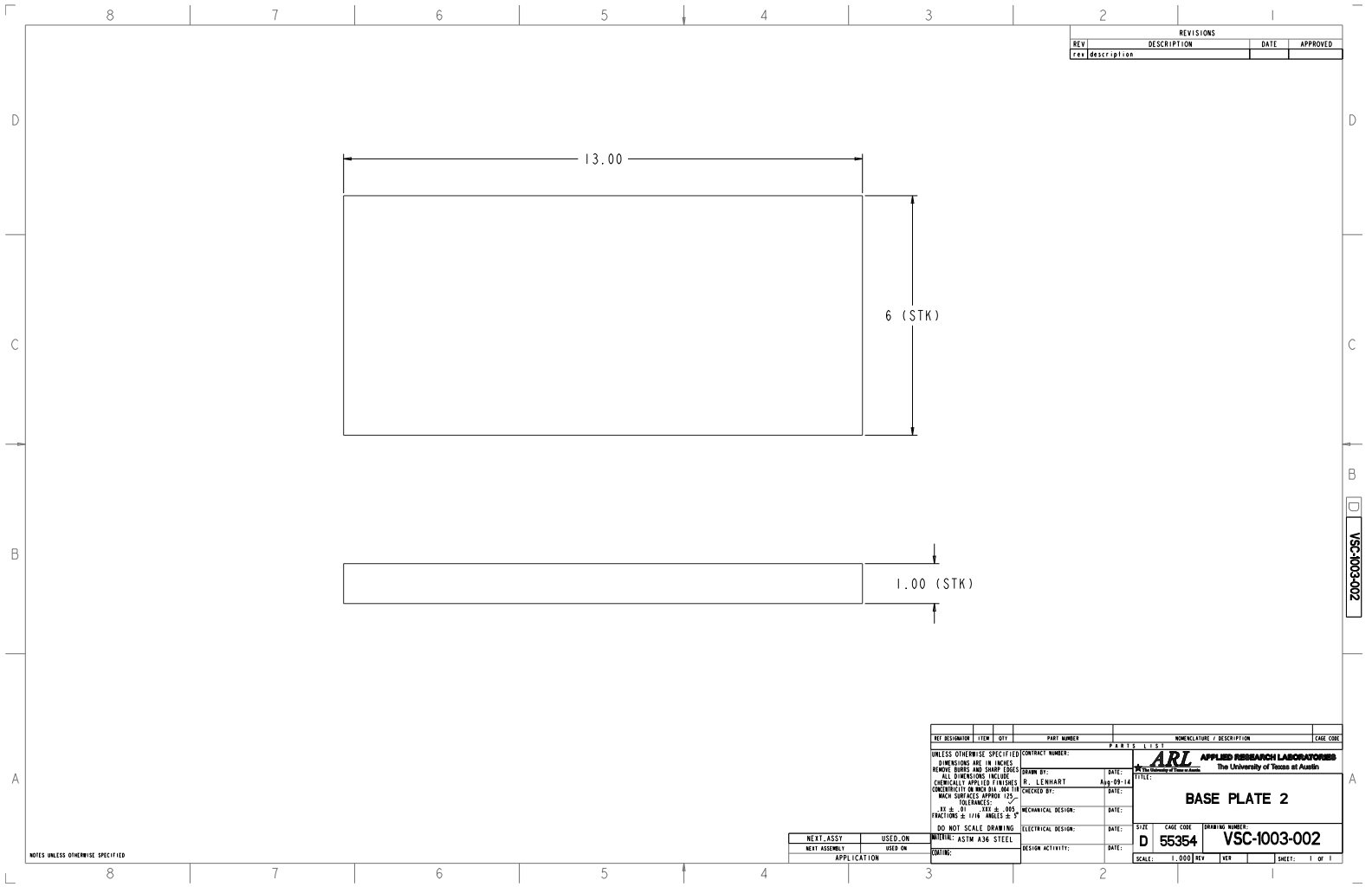

REVISIONS

REV	DESCRIPTION	DATE	APPROVED
rev	description		

PARTS LIST

REF DESIGNATOR	ITEM	QTY	PART NUMBER	NOMENCLATURE / DESCRIPTION	CAGE CODE

UNLESS OTHERWISE SPECIFIED
DIMENSIONS ARE IN INCHES
REMOVE BURRS AND SHARP EDGES
ALL DIMENSIONS INCLUDE CHEMICALLY APPLIED FINISHES
CONCENTRICITY ON MACH DIA .004 TIR
MACH SURFACES APPROX 125
TOLERANCES:
.XX ± .01 .XXX ± .005
FRACTIONS ± 1/16 ANGLES ± 5°
DO NOT SCALE DRAWING

CONTRACT NUMBER:
DRAWN BY: R. LENHART DATE: Aug-09-14
CHECKED BY: DATE:
MECHANICAL DESIGN: DATE:
ELECTRICAL DESIGN: DATE:
DESIGN ACTIVITY: DATE:

MATERIAL: ASTM A36 STEEL
COATING:

NEXT ASSY | USED ON
NEXT ASSEMBLY | USED ON
APPLICATION

NOTES UNLESS OTHERWISE SPECIFIED

ARL APPLIED RESEARCH LABORATORIES
The University of Texas at Austin

TITLE: BASE PLATE 2

SIZE: D | CAGE CODE: 55354 | DRAWING NUMBER: VSC-1003-002

SCALE: 1.000 | REV | VER | SHEET: 1 OF 1

VSC-1003-002

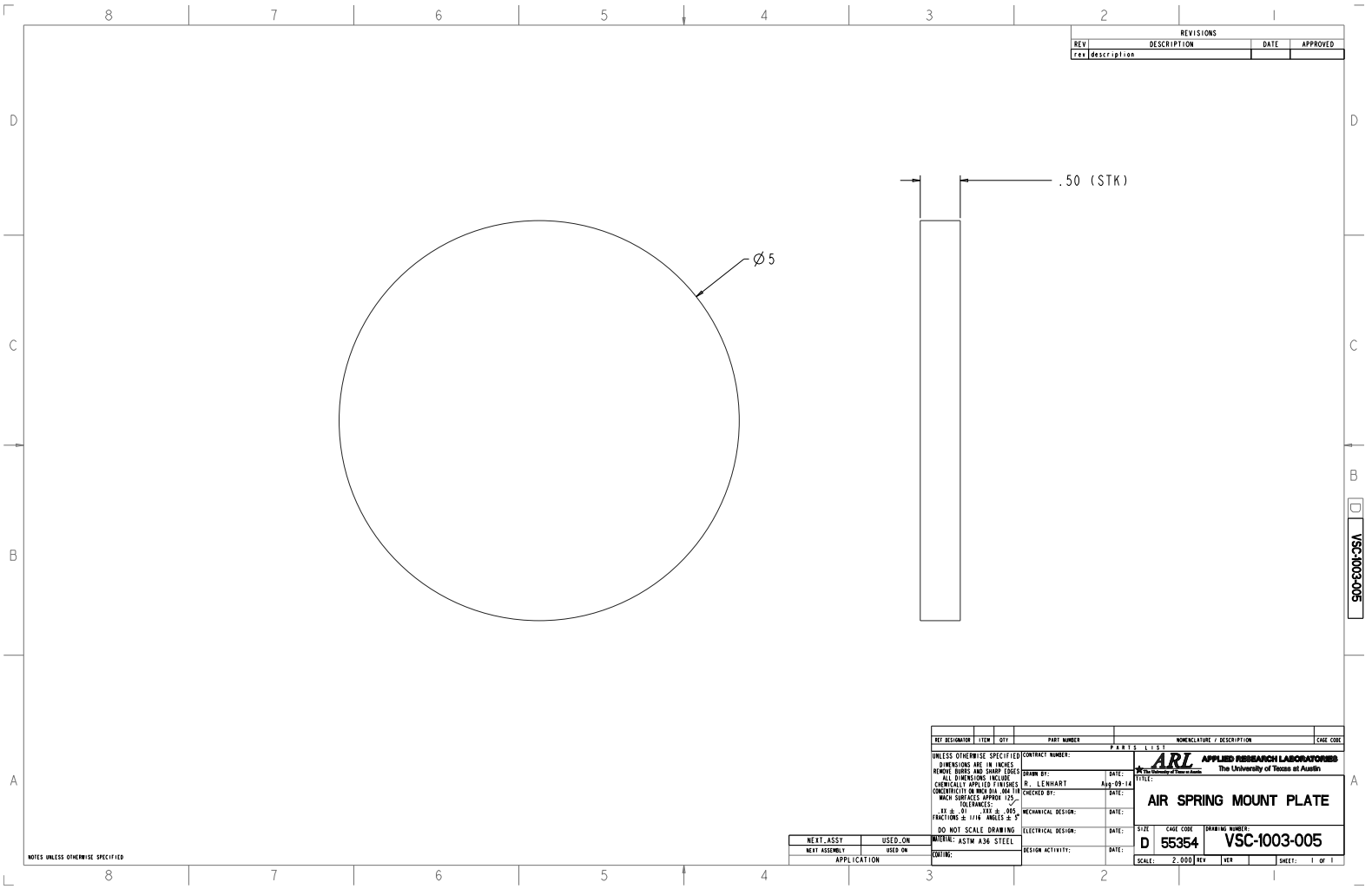
REVISIONS
REV
DESCRIPTION
DATE
APPROVED
rev
description
.50 (STK)
Ø5
VSC-1003-005
REF DESIGNATOR
ITEM
QTY
PART NUMBER
NOMENCLATURE / DESCRIPTION
CAGE CODE
PARTS LIST
UNLESS OTHERWISE SPECIFIED
DIMENSIONS ARE IN INCHES
REMOVE BURRS AND SHARP EDGES
ALL DIMENSIONS INCLUDE
CHEMICALLY APPLIED FINISHES
CONCENTRICITY ON INDICATED DIA. .004 TIR
MACH SURFACES APPROX 125
TOLERANCES:
.XX ± .01 .XXX ± .005
FRACTIONS ± 1/16 ANGLES ± 5°
DO NOT SCALE DRAWING
MATERIAL: ASTM A36 STEEL
COATING:
CONTRACT NUMBER:
DRAWN BY:
R. LENHART
DATE:
Aug-09-14
CHECKED BY:
MECHANICAL DESIGN:
ELECTRICAL DESIGN:
DESIGN ACTIVITY:
APPLIED RESEARCH LABORATORIES
The University of Texas at Austin
TITLE:
AIR SPRING MOUNT PLATE
SIZE
D
CAGE CODE
55354
DRAWING NUMBER:
VSC-1003-005
SCALE: 2.000
REV
VER
SHEET: 1 OF 1
NEXT ASSY
USED ON
NEXT ASSEMBLY
APPLICATION
NOTES UNLESS OTHERWISE SPECIFIED

D.5 Sensor Isolation System

REVISIONS			
REV	DESCRIPTION	DATE	APPROVED
rev	description		

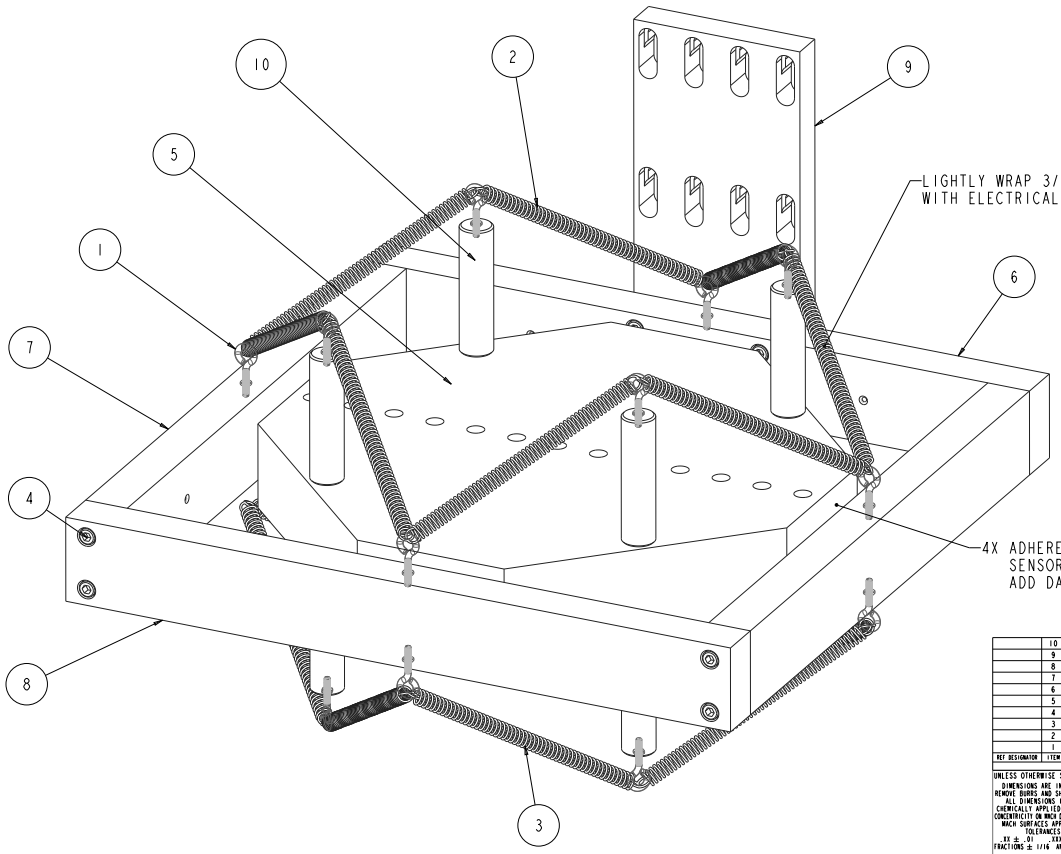

REF DESIGNATOR	ITEM	QTY	PART NUMBER	NOMENCLATURE / DESCRIPTION	CAGE CODE
	10	8	VSC-1004-006	SENS ISO SPRING STANDOFF	
	9	1	VSC-1004-005	SENS ISO FRAME MOUNT	
	8	1	VSC-1004-004	SENS ISO FRAME 3	
	7	2	VSC-1004-003	SENS ISO FRAME 2	
	6	1	VSC-1004-002	SENS ISO FRAME 1	
	5	1	VSC-1004-001	SENSOR ISOLATION MASS	
	4	12	MS16995-53	SCREW, CAP, SOCH, .250-20UNC X 1.25 LG, CRES	96906
	3	8	LEE SPRING LEM 1200 11 S	EXTENSION SPRING	
	2	8	LEE SPRING LE 045E 12 S	EXTENSION SPRING	
	1	16	94891542	6-32 EYEBOLT	

PARTS LIST

UNLESS OTHERWISE SPECIFIED
DIMENSIONS ARE IN INCHES
REMOVE BURRS AND SHARP EDGES
ALL DIMENSIONS INCLUDE CHEMICALLY APPLIED FINISHES
CONCENTRICITY ON MACH DIA .004 TIR
MACH SURFACES APPROX 125
TOLERANCES:
.XX ± .01 .XXX ± .005
FRACTIONS ± 1/16 ANGLES ± 5°
DO NOT SCALE DRAWING

CONTRACT NUMBER:
DRAWN BY: R. LENHART DATE: Aug-09-14
CHECKED BY: DATE:
MECHANICAL DESIGN: DATE:
ELECTRICAL DESIGN: DATE:
DESIGN ACTIVITY: DATE:

ARL The University of Texas at Austin
APPLIED RESEARCH LABORATORIES
The University of Texas at Austin

TITLE: SENSOR ISOLATION SYSTEM

SIZE	CAGE CODE	DRAWING NUMBER
D	55354	VSC-1004-000

SCALE: 0.500 REV VER SHEET: 1 OF 1

NEXT_ASSY	USED_ON
NEXT ASSEMBLY	USED ON
APPLICATION	

MATERIAL:
COATING:

NOTES UNLESS OTHERWISE SPECIFIED

VSC-1004-000

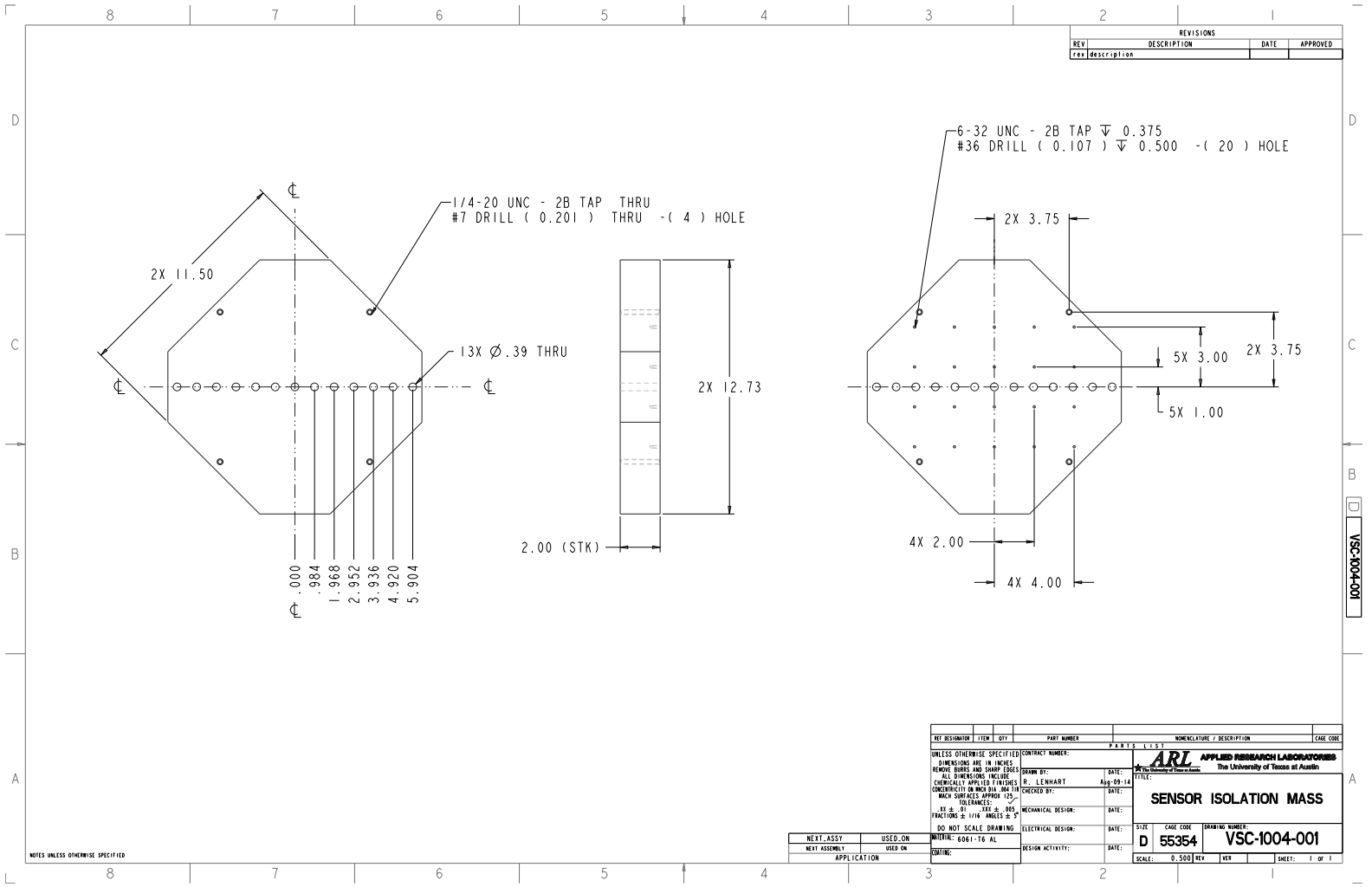
REVISIONS
REV | DESCRIPTION | DATE | APPROVED
rev | description
2X 11.50
1/4-20 UNC - 2B TAP THRU
#7 DRILL (0.201) THRU -(4) HOLE
13X Ø.39 THRU
2X 12.73
2.00 (STK)
.000
.984
1.968
2.952
3.936
4.920
5.904
6-32 UNC - 2B TAP ↧ 0.375
#36 DRILL (0.107) ↧ 0.500 -(20) HOLE
2X 3.75
5X 3.00
2X 3.75
5X 1.00
4X 2.00
4X 4.00
VSC-1004-001
REF DESIGNATOR | ITEM | QTY | PART NUMBER | NOMENCLATURE / DESCRIPTION | CAGE CODE
PARTS LIST
UNLESS OTHERWISE SPECIFIED
DIMENSIONS ARE IN INCHES
REMOVE BURRS AND SHARP EDGES
ALL DIMENSIONS INCLUDE
CHEMICALLY APPLIED FINISHES
CONCENTRICITY ON MACH DIA .004 TIR
MACH SURFACES APPROX 125
TOLERANCES:
.XX ± .01 .XXX ± .005
FRACTIONS ± 1/16 ANGLES ± 5°
DO NOT SCALE DRAWING
CONTRACT NUMBER:
DRAWN BY: R. LENHART DATE: Aug-09-14
CHECKED BY: DATE:
MECHANICAL DESIGN: DATE:
ELECTRICAL DESIGN: DATE:
DESIGN ACTIVITY: DATE:
MATERIAL: 6061-T6 AL
COATING:
NEXT ASSY | USED ON
NEXT ASSEMBLY | USED ON
APPLICATION
ARL APPLIED RESEARCH LABORATORIES
The University of Texas at Austin
TITLE:
SENSOR ISOLATION MASS
SIZE D | CAGE CODE 55354 | DRAWING NUMBER: VSC-1004-001
SCALE: 0.500 | REV | VER | SHEET: 1 OF 1
NOTES UNLESS OTHERWISE SPECIFIED

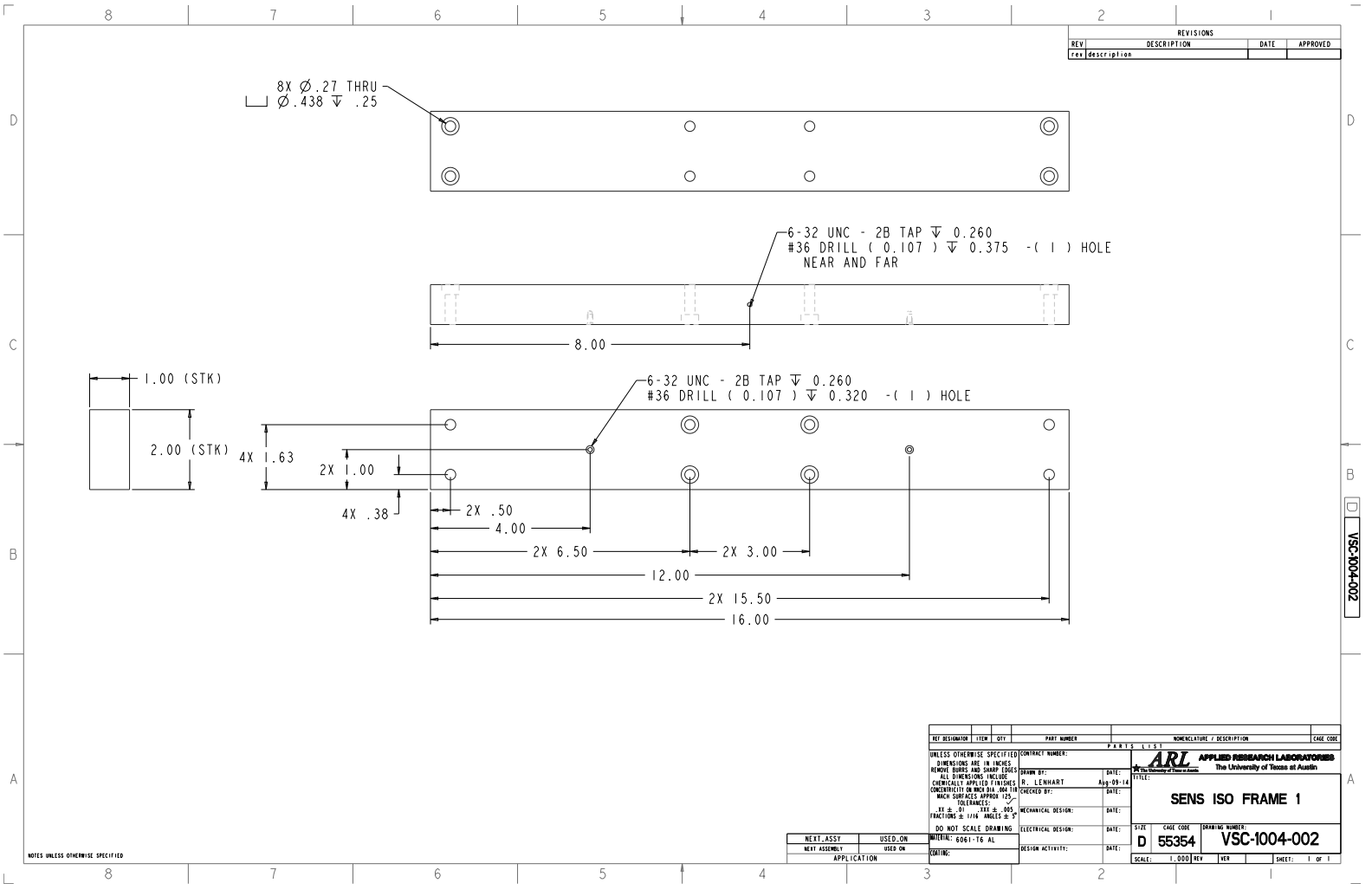
REVISIONS
REV | DESCRIPTION | DATE | APPROVED
rev | description
8X Ø.27 THRU
Ø.438 ↧ .25
6-32 UNC - 2B TAP ↧ 0.260
#36 DRILL (0.107) ↧ 0.375 -(I) HOLE
NEAR AND FAR
8.00
1.00 (STK)
2.00 (STK)
4X 1.63
2X 1.00
4X .38
6-32 UNC - 2B TAP ↧ 0.260
#36 DRILL (0.107) ↧ 0.320 -(I) HOLE
2X .50
4.00
2X 6.50
2X 3.00
12.00
2X 15.50
16.00
REF DESIGNATOR | ITEM | QTY | PART NUMBER | NOMENCLATURE / DESCRIPTION | CAGE CODE
PARTS LIST
UNLESS OTHERWISE SPECIFIED
DIMENSIONS ARE IN INCHES
REMOVE BURRS AND SHARP EDGES
ALL DIMENSIONS INCLUDE
CHEMICALLY APPLIED FINISHES
CONCENTRICITY ON INNER DIA .004 TIR
MACH SURFACES APPROX 125
TOLERANCES:
.XX ± .01 .XXX ± .005
FRACTIONS ± 1/16 ANGLES ± 5°
DO NOT SCALE DRAWING
MATERIAL: 6061-T6 AL
COATING:
CONTRACT NUMBER:
DRAWN BY: R. LENHART DATE: Aug-09-14
CHECKED BY: DATE:
MECHANICAL DESIGN: DATE:
ELECTRICAL DESIGN: DATE:
DESIGN ACTIVITY: DATE:
APPLIED RESEARCH LABORATORIES
The University of Texas at Austin
TITLE:
SENS ISO FRAME 1
SIZE D
CAGE CODE 55354
DRAWING NUMBER: VSC-1004-002
SCALE: 1.000 REV VER SHEET: 1 OF 1
NEXT ASSY | USED ON
NEXT ASSEMBLY | USED ON
APPLICATION
NOTES UNLESS OTHERWISE SPECIFIED
VSC-1004-002

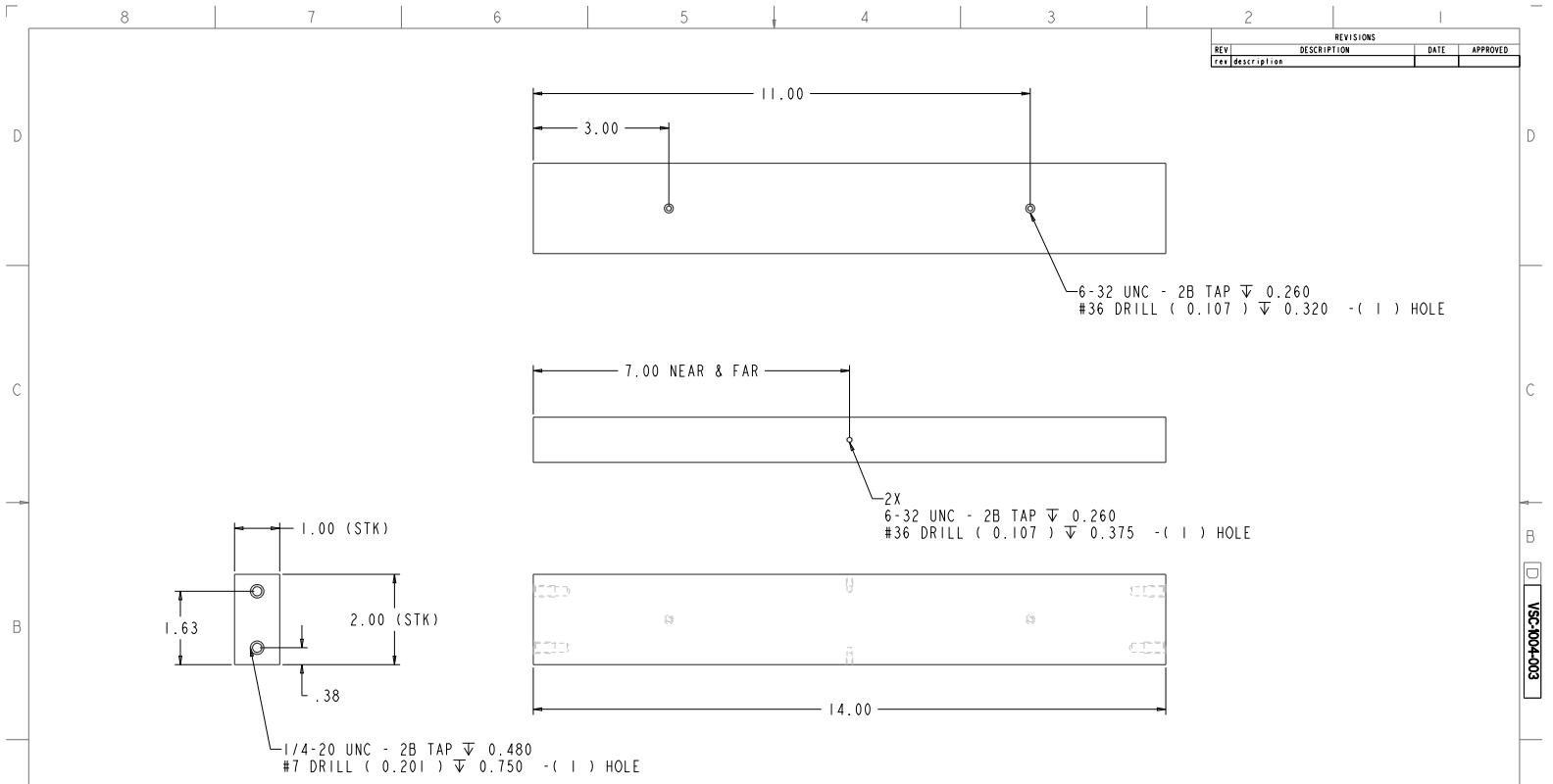

REVISIONS

REV	DESCRIPTION	DATE	APPROVED
rev	description		

PARTS LIST

REF DESIGNATOR	ITEM	QTY	PART NUMBER	NOMENCLATURE / DESCRIPTION	CAGE CODE

UNLESS OTHERWISE SPECIFIED
DIMENSIONS ARE IN INCHES
REMOVE BURRS AND SHARP EDGES
ALL DIMENSIONS INCLUDE CHEMICALLY APPLIED FINISHES
CONCENTRICITY ON MACH DIA .004 TIR
MACH SURFACES APPROX 125
TOLERANCES:
.XX ± .01 .XXX ± .005
FRACTIONS ± 1/16 ANGLES ± 5°
DO NOT SCALE DRAWING

MATERIAL: 6061-T6 AL
COATING:

CONTRACT NUMBER:
DRAWN BY: R. LENHART — DATE: Aug-09-14
CHECKED BY: — DATE:
MECHANICAL DESIGN: — DATE:
ELECTRICAL DESIGN: — DATE:
DESIGN ACTIVITY: — DATE:

NEXT ASSY | USED ON
NEXT ASSEMBLY | USED ON
APPLICATION

ARL APPLIED RESEARCH LABORATORIES
The University of Texas at Austin

TITLE: SENS ISO FRAME 2

SIZE: D | CAGE CODE: 55354 | DRAWING NUMBER: VSC-1004-003

SCALE: 1.000 | REV | VER | SHEET: 1 OF 1

NOTES UNLESS OTHERWISE SPECIFIED

VSC-1004-003

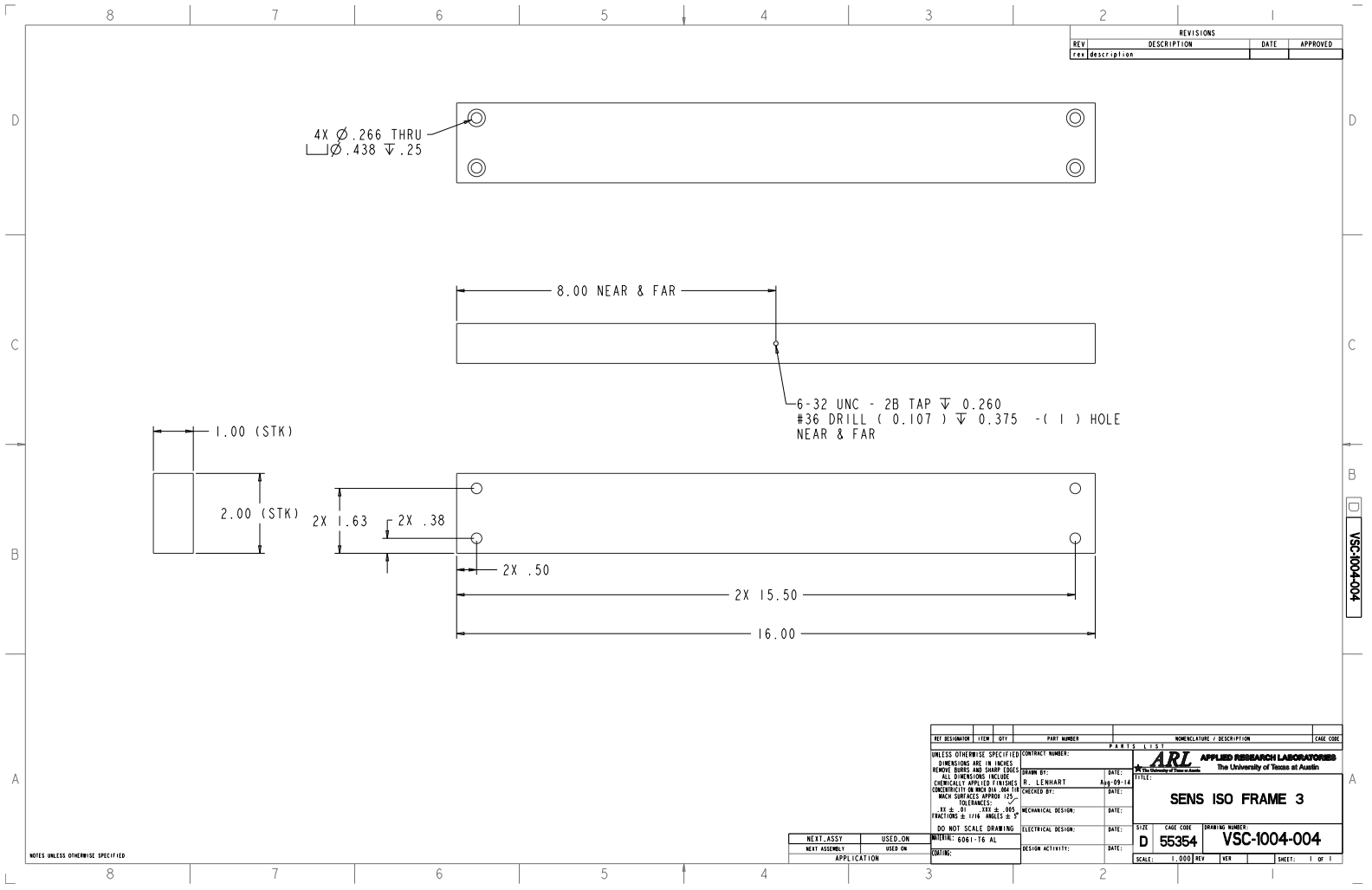
REVISIONS
REV | DESCRIPTION | DATE | APPROVED
rev | description
4X Ø.266 THRU
⌴Ø.438 ↧.25
8.00 NEAR & FAR
6-32 UNC - 2B TAP ↧ 0.260
#36 DRILL (0.107) ↧ 0.375 -(I) HOLE
NEAR & FAR
1.00 (STK)
2.00 (STK)
2X 1.63
2X .38
2X .50
2X 15.50
16.00
VSC-1004-004
PARTS LIST
REF DESIGNATOR | ITEM | QTY | PART NUMBER | NOMENCLATURE / DESCRIPTION | CAGE CODE
UNLESS OTHERWISE SPECIFIED
DIMENSIONS ARE IN INCHES
REMOVE BURRS AND SHARP EDGES
ALL DIMENSIONS INCLUDE
CHEMICALLY APPLIED FINISHES
CONCENTRICITY ON MACH DIA .004 TIR
MACH SURFACES APPROX 125
TOLERANCES:
.XX ± .01 .XXX ± .005
FRACTIONS ± 1/16 ANGLES ± 5°
DO NOT SCALE DRAWING
CONTRACT NUMBER:
DRAWN BY: R. LENHART
DATE: Aug-09-14
CHECKED BY:
MECHANICAL DESIGN:
ELECTRICAL DESIGN:
DESIGN ACTIVITY:
MATERIAL: 6061-T6 AL
COATING:
NEXT ASSY | USED ON
NEXT ASSEMBLY | USED ON
APPLICATION
ARL APPLIED RESEARCH LABORATORIES
The University of Texas at Austin
TITLE:
SENS ISO FRAME 3
SIZE D | CAGE CODE 55354 | DRAWING NUMBER: VSC-1004-004
SCALE: 1.000 | REV | VER | SHEET: 1 OF 1
NOTES UNLESS OTHERWISE SPECIFIED

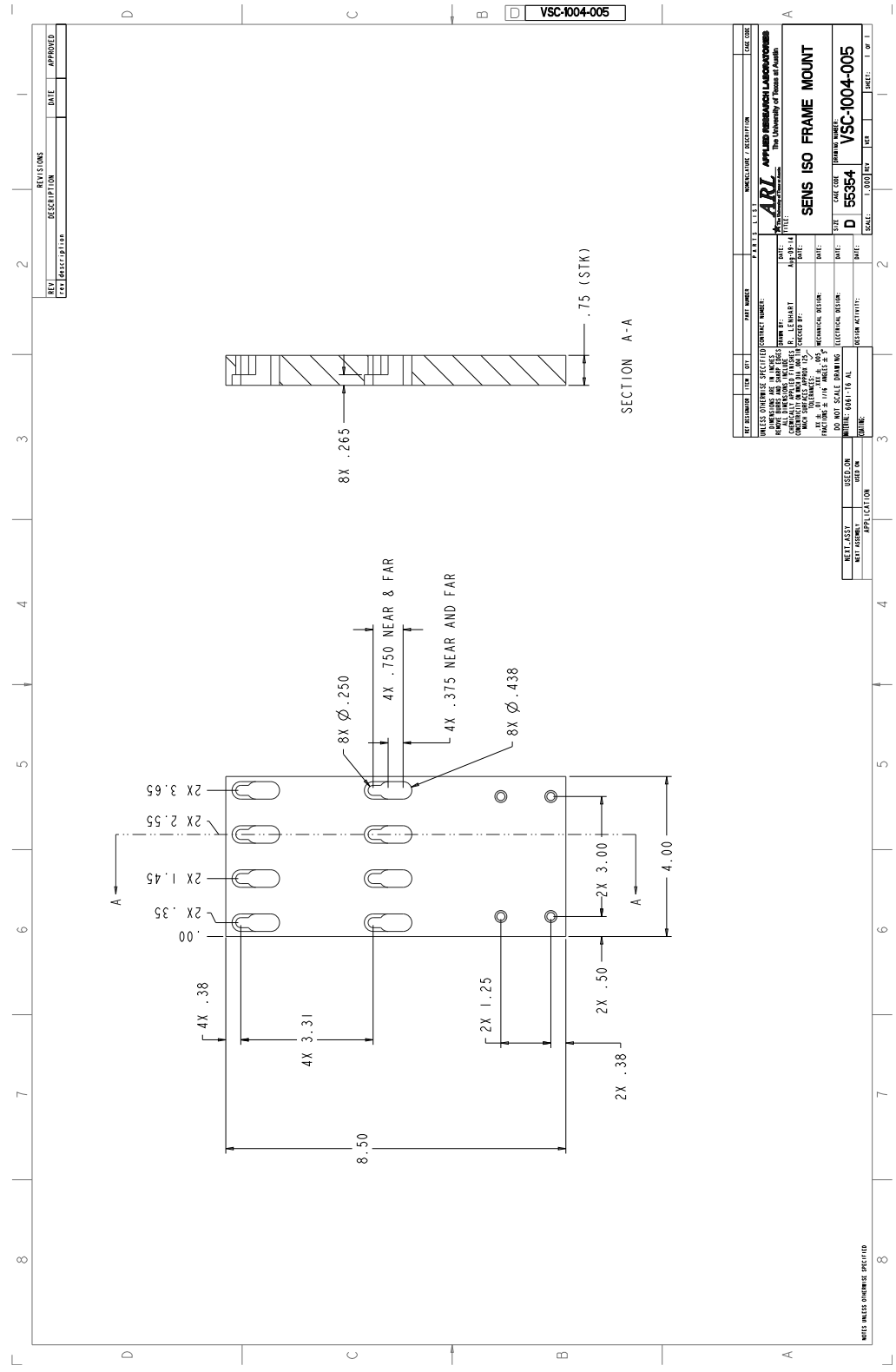
VSC-1004-005
REVISIONS
REV
DESCRIPTION
DATE
APPROVED
rev description
.75 (STK)
8X .265
SECTION A-A
8X Ø.250
4X .750 NEAR & FAR
4X .375 NEAR AND FAR
8X Ø.438
2X 3.65
2X 2.55
2X 1.45
2X .35
.00
4X .38
4X 3.31
2X 1.25
2X 3.00
2X .50
2X .38
4.00
8.50
NEXT ASSY
USED ON
APPLICATION
DO NOT SCALE DRAWING
MATERIAL: 6061-T6 AL
FINISH:
DESIGN ACTIVITY:
APPLIED RESEARCH LABORATORIES
The University of Texas at Austin
SENS ISO FRAME MOUNT
SIZE
D
CAGE CODE
55354
DRAWING NUMBER
VSC-1004-005
SCALE: 1.000
REV
SHEET 1 OF 1

REVISIONS			
REV	DESCRIPTION	DATE	APPROVED
rev	description		

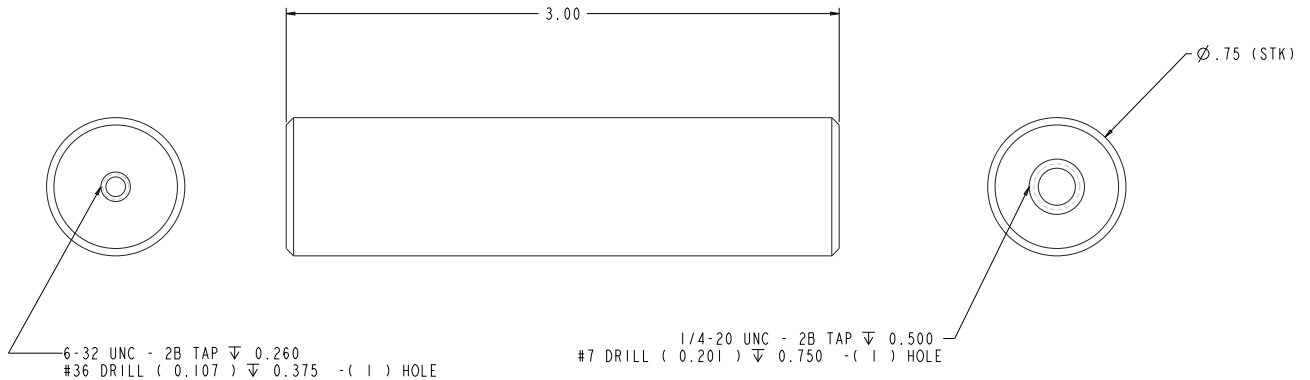

VSC-1004-006

REF DESIGNATOR	ITEM	QTY	PART NUMBER	NOMENCLATURE / DESCRIPTION	CAGE CODE

PARTS LIST

UNLESS OTHERWISE SPECIFIED
DIMENSIONS ARE IN INCHES
REMOVE BURRS AND SHARP EDGES
ALL DIMENSIONS INCLUDE CHEMICALLY APPLIED FINISHES
CONCENTRICITY ON MACH DIA .004 TIR
MACH SURFACES APPROX 125
TOLERANCES:
.XX ± .01 .XXX ± .005
FRACTIONS ± 1/16 ANGLES ± 5°
DO NOT SCALE DRAWING

CONTRACT NUMBER:
DRAWN BY: R. LENHART DATE: Aug-09-14
CHECKED BY: DATE:
MECHANICAL DESIGN: DATE:
ELECTRICAL DESIGN: DATE:
DESIGN ACTIVITY: DATE:

MATERIAL: 6061-T6 AL
COATING:

NEXT ASSY	USED ON
NEXT ASSEMBLY	USED ON
APPLICATION	

ARL APPLIED RESEARCH LABORATORIES
The University of Texas at Austin

TITLE: SENS ISO SPRING STANDOFF

SIZE	CAGE CODE	DRAWING NUMBER
D	55354	VSC-1004-006

SCALE: 4.000 REV VER SHEET: 1 OF 1

NOTES UNLESS OTHERWISE SPECIFIED

D.6 Linear Actuator Frame Assembly

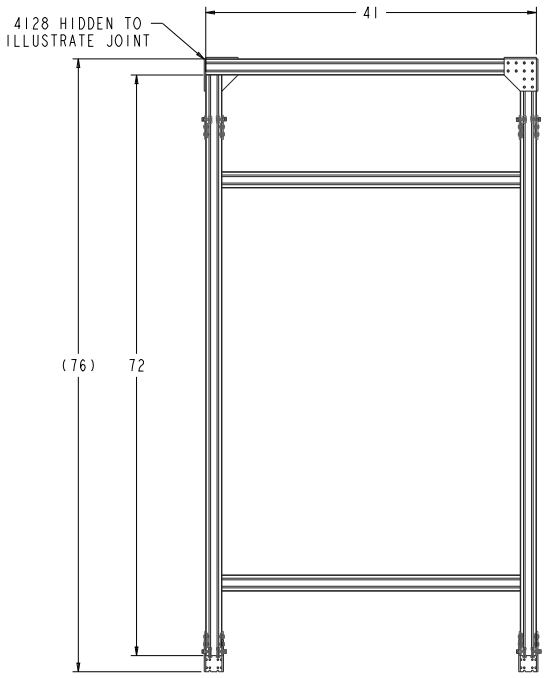

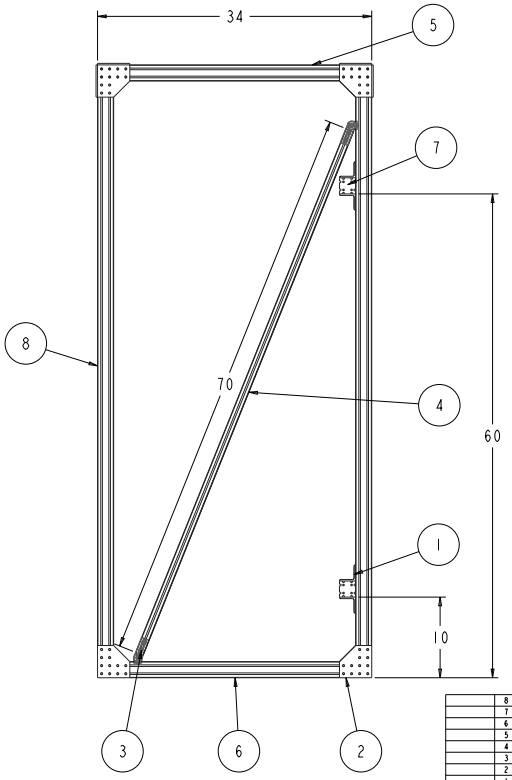

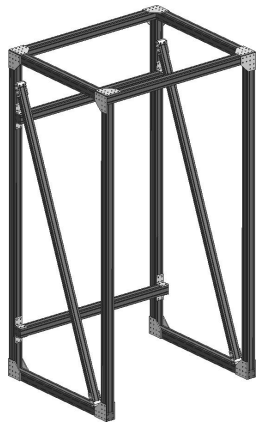

SCALE 0.100

REVISIONS			
REV	DESCRIPTION	DATE	APPROVED
rev	description		

REF DESIGNATOR	ITEM	QTY	PART NUMBER	NOMENCLATURE / DESCRIPTION	CAGE CODE
	8	4	80/20, INC. 2020, 72 LONG	10 SERIES FRACTIONAL T-SLOT FRAMING	
	7	4	80/20, INC. 2020, 41 LONG	10 SERIES FRACTIONAL T-SLOT FRAMING	
	6	2	80/20, INC. 2020, 34 LONG	10 SERIES FRACTIONAL T-SLOT FRAMING	
	5	2	80/20, INC. 2020, 30 LONG	10 SERIES FRACTIONAL T-SLOT FRAMING	
	4	2	80/20, INC. 1020, 70 LONG	10 SERIES FRACTIONAL T-SLOT FRAMING	
	3	4	80/20, INC. 4178	10 SERIES LIVING HINGE ASSY	
	2	20	80/20, INC. 4128	12 HOLE 90° JOINING PLATE	
	1	8	80/20, INC. 4114	8 HOLE INSIDE CORNER BRACKET	

PARTS LIST

FRAME CONSTRUCTED FROM 80/20, INC.
10 SERIES FRACTIONAL T-SLOT FRAMING
FASTENERS ARE NOT SHOWN

NOTES UNLESS OTHERWISE SPECIFIED

UNLESS OTHERWISE SPECIFIED
DIMENSIONS ARE IN INCHES
REMOVE BURRS AND SHARP EDGES
ALL DIMENSIONS INCLUDE CHEMICALLY APPLIED FINISHES
CONCENTRICITY ON MACH DIA .004 TIR
MACH SURFACES APPROX 125
TOLERANCES:
.XX ± .01 .XXX ± .005
FRACTIONS ± 1/16 ANGLES ± 5°
DO NOT SCALE DRAWING

CONTRACT NUMBER:
DRAWN BY: R. LENHART DATE: Aug-09-14
CHECKED BY: DATE:
MECHANICAL DESIGN: DATE:
ELECTRICAL DESIGN: DATE:
DESIGN ACTIVITY: DATE:

MATERIAL:
COATING:

NEXT ASSY | USED ON
NEXT ASSEMBLY | USED ON
APPLICATION

ARL APPLIED RESEARCH LABORATORIES
The University of Texas at Austin

TITLE: ACTUATOR FRAME ASSY

SIZE: D | CAGE CODE: 55354 | DRAWING NUMBER: VSC-1005-000

SCALE: 0.175 | REV | VER | SHEET: 1 OF 1

VSC-1005-000

D.7 Schematic of Degassing Hardware

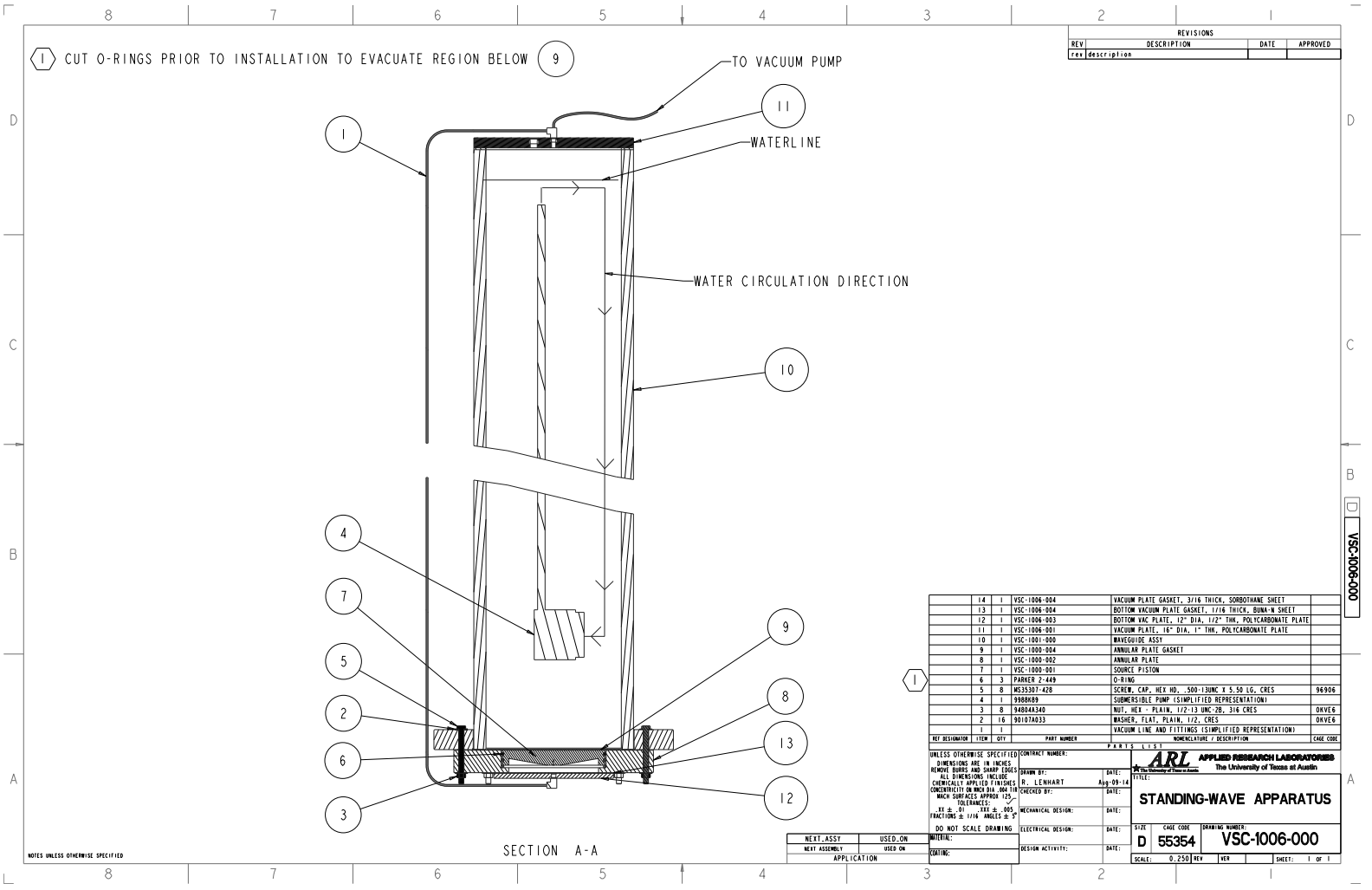

REVISIONS			
REV	DESCRIPTION	DATE	APPROVED
rev	description		

	ITEM	QTY	PART NUMBER	NOMENCLATURE / DESCRIPTION	CAGE CODE
	14	1	VSC-1006-004	VACUUM PLATE GASKET, 3/16 THICK, SORBOTHANE SHEET	
	13	1	VSC-1006-004	BOTTOM VACUUM PLATE GASKET, 1/16 THICK, BUNA-N SHEET	
	12	1	VSC-1006-003	BOTTOM VAC PLATE, 12" DIA, 1/2" THK, POLYCARBONATE PLATE	
	11	1	VSC-1006-001	VACUUM PLATE, 16" DIA, 1" THK, POLYCARBONATE PLATE	
	10	1	VSC-1001-000	WAVEGUIDE ASSY	
	9	1	VSC-1000-004	ANNULAR PLATE GASKET	
	8	1	VSC-1000-002	ANNULAR PLATE	
	7	1	VSC-1000-001	SOURCE PISTON	
1	6	3	PARKER 2-449	O-RING	
	5	8	MS35307-428	SCREW, CAP, HEX HD, .500-13UNC X 5.50 LG, CRES	96906
	4	1	9980K89	SUBMERSIBLE PUMP (SIMPLIFIED REPRESENTATION)	
	3	8	94804A340	NUT, HEX - PLAIN, 1/2-13 UNC-2B, 316 CRES	0KVE6
	2	16	90107A033	WASHER, FLAT, PLAIN, 1/2, CRES	0KVE6
	1	1		VACUUM LINE AND FITTINGS (SIMPLIFIED REPRESENTATION)	

PARTS LIST

UNLESS OTHERWISE SPECIFIED
DIMENSIONS ARE IN INCHES
REMOVE BURRS AND SHARP EDGES
ALL DIMENSIONS INCLUDE CHEMICALLY APPLIED FINISHES
CONCENTRICITY ON INDICATED DIA .004 TIR
MACH SURFACES APPROX 125
TOLERANCES:
.XX ± .01 .XXX ± .005
FRACTIONS ± 1/16 ANGLES ± 5°
DO NOT SCALE DRAWING

CONTRACT NUMBER:
DRAWN BY: R. LENHART DATE: Aug-09-14
CHECKED BY: DATE:
MECHANICAL DESIGN: DATE:
ELECTRICAL DESIGN: DATE:
DESIGN ACTIVITY: DATE:

ARL APPLIED RESEARCH LABORATORIES
The University of Texas at Austin

TITLE: STANDING-WAVE APPARATUS

SIZE: D | CAGE CODE: 55354 | DRAWING NUMBER: VSC-1006-000
SCALE: 0.250 | REV | VER | SHEET: 1 OF 1

NEXT ASSY	USED ON
NEXT ASSEMBLY	USED ON
APPLICATION	

MATERIAL:
COATING:

NOTES UNLESS OTHERWISE SPECIFIED

VSC-1006-000

Bibliography

[1] H. Li, Z. D. Deng, and T. J. Carlson, "Piezoelectric materials used in underwater acoustic transducers," Sensor Letters **10**, 679–697 (2012).

[2] X. Lurton, *An Introduction to Underwater Acoustics: Principles and Applications* (Springer, Berlin - Heidelberg, 2010), 2nd edition.

[3] R. P. Hodges, *Underwater Acoustics: Analysis, Design and Performance of Sonar* (Wiley, Singapore, 2011).

[4] L. Ziomek, *Fundamentals of Acoustic Field Theory and Space-Time Signal Processing* (Taylor & Francis, Boca Raton, FL, 1994).

[5] G. L. D'Spain, J. C. Luby, G. R. Wilson, and R. A. Gramann, "Vector sensors and vector sensor line arrays: Comments on optimal array gain and detection," J. Acoust. Soc. Am. **120**, 171–185 (2006).

[6] K. T. Wong and M. D. Zoltowski, "Extended-aperture underwater acoustic multisource azimuth/elevation direction-finding using uniformly but sparsely spaced vector hydrophones," IEEE J. Oceanic Eng. **22**, 659–672 (1997).

[7] K. Kim, T. B. Gabrielson, and G. C. Lauchle, "Development of an accelerometer-based underwater acoustic intensity sensor," J. Acoust. Soc. Am. **116**, 3384–3392 (2004).

[8] J. A. McConnell and G. C. Lauchle, "Calibration of a neutrally buoyant p-u intensity probe," J. Acoust. Soc. Am. **103**, 2755–2756 (1998).

[9] D. Desrochers, *High Resolution Beamforming Techniques Applied to a DIFAR Sonobuoy*, Master's thesis, Royal Military College of Canada (1999).

[10] J. C. Shipps and B. M. Abraham, "The use of vector sensors for underwater port and waterway security," in *Sensors for Industry Conference, 2004. Proceedings the ISA/IEEE* (2004), pp. 41–44.

[11] A. Thode, J. Skinner, P. Scott, J. Roswell, J. Straley, and K. Folkert, "Tracking sperm whales with a towed acoustic vector sensor," J. Acoust. Soc. Am. **128**, 2681–2694 (2010).

[12] J. A. McConnell, "Directional acoustic receivers for anti-submarine warfare and torpedo defense," Tech. rep., Applied Physical Sciences, 475 Bridge Street, Groton, CT 06340. URL `http://www.virtualacquisitionshowcase.com/document/427/briefing`.

[13] R. J. Bobber, *Underwater Electroacoustic Measurements* (Naval Research Laboratory, Washington D.C., 1970).

[14] Teledyne RESON, Fabriksvangen 13, DK-3550 Slangerup, Denmark, *Hydrophone TC4013: Miniature Reference Hydrophone*. URL `http://www.teledyne-reson.com/download/hydrophone_data_sheets__/TC4013.pdf`.

[15] J. A. McConnell, *Development and Application of Inertial Type Underwater Acoustic Intensity Probes*, Ph.D. thesis, The Pennsylvania State University (2004).

[16] The Mathworks, Inc., 24 Prime Park Way, Natick, MA 01760.

[17] D. T. Blackstock, *Fundamentals of Physical Acoustics* (Wiley, New York, 2000).

[18] R. D. Fay, R. L. Brown, and O. V. Fortier, "Measurement of acoustic impedances of surfaces in water," J. Acoust. Soc. Am. **19**, 850–856 (1947).

[19] W. J. Jacobi, "Propagation of sound waves along liquid cylinders," J. Acoust. Soc. Am. **21**, 120–127 (1949).

[20] T. C. Lin and G. W. Morgan, "Wave propagation through fluid contained in a cylindrical, elastic shell," J. Acoust. Soc. Am. **28**, 1165–1176 (1956).

[21] V. A. Del Grosso, "Analysis of multimode acoustic propagation in liquid cylinders with realistic boundary conditions; application to sound speed and absorption measurements," Acustica **24**, 299–311 (1971).

[22] L. D. Lafleur and F. D. Shields, "Low-frequency propagation modes in a liquid-filled elastic tube waveguide," J. Acoust. Soc. Am. **97**, 1435–1445 (1995).

[23] P. S. Wilson, R. A. Roy, and W. M. Carey, "An improved water-filled impedance tube," J. Acoust. Soc. Am. **113**, 3245–3252 (2003).

[24] V. A. Gordienko, E. L. Gordienko, A. V. Dryndin, and S. M. Likhachev, "Absolute pressure calibration of acoustic receivers in a vibrating column of liquid," Acoust. Phy. **40**, 219–222 (1994).

[25] ASTM Standard B429/B429M-10, 2010, "Specification for aluminum-alloy extruded structural pipe and tube," ASTM International, 100 Bar Harbor Dr., West Conshohocken, PA 19428.

[26] ASME Standard B36.10M, 2004, "Welded and seamless wrought steel pipe," American Society of Mechanical Engineers, Three Park Ave., NY, NY 10016.

[27] ASTM Standard A106/A106M-11, 2011, "Standard specification for aluminum-alloy extruded structural pipe and tube," ASTM International, 100 Bar Harbor Dr., West Conshohocken, PA 19428.

[28] "ASTM steel, bar," URL `http://www.matweb.com/search/DataSheet.aspx?MatGUID=d1844977c5c8440cb9a3a967f8909c3a&ckck=1`.

[29] L. E. Kinsler, A. R. Frey, A. B. Coppens, and J. V. Sanders, *Fundamentals of Acoustics* (John Wiley & Sons, New York, 2000), 4th edition.

[30] *Properties of Wrought Aluminum and Aluminum Alloys, Properties and Selection: Nonferrous Alloys and Special-Purpose Materials*, Vol. 2 of *ASM Handbook* (ASM International, Materials Park, OH, 1990).

[31] S. D. Washko and G. Aggen, *Wrought Stainless Steels, Properties and Selection: Irons, Steels, and High-Performance Alloys*, Vol. 1 of *ASM Handbook* (ASM International, Materials Park, OH, 1990).

[32] S. Lampman, *Wrought Titanium and Titanium Alloys, Properties and Selection: Nonferrous Alloys and Special-Purpose Materials*, Vol. 2 of *ASM Handbook* (ASM International, Materials Park, OH, 1990).

[33] ANSYS, Inc., Southpointe 275 Technology Dr., Canonsburg, PA 15317.

[34] W. H. Duan, C. M. Wang, and C. Y. Wang, "Modification of fundamental vibration modes of circular plates with free edges," Journal of Sound and Vibration **317**, 709–715 (2008).

[35] Parker Hannifin Corporation O-ring Divison, 2360 Palumbo Drive Lexington, KY 40509, *Parker O-ring Handbook* (2007).

[36] I. Green and C. English, "Analysis of elastomeric o-ring seals in compression using the finite element method," Tribology Transactions **35**, 83–88 (1992).

[37] J. Kunz and M. Studer, "Determining the modulus of elasticity in compression via the Shore A hardness," Kunststoffe International **6**, 92–94 (2006).

[38] Labworks Inc., 2950 Airway Ave., A-16 Costa Mesa, Ca 92626, *FG-142 Force Generator*. URL `http://www.labworks-inc.com/downloads/FG142_datasheet.pdf`.

[39] L. Beranek, *Acoustics* (McGraw-Hill, Woodbury, NY, 1954).

[40] PTC, Inc., 140 Kendrick Street, Needham, MA 02494.

[41] Firestone Industrial Products, Firestone Industrial Products 250 W. 96th St. Indianapolis, IN 46260, *Airstroke^{TM} and Airmount ^{TM} Engineering Manual and Design Guide* (2007). URL `http://www.ferret.com.au/ODIN/PDF/Showcases/101465.pdf`.

[42] National Instruments Corp., 11500 N Mopac Expwy, Austin, TX 78759.

[43] Agilent Technologies, Inc., 5301 Stevens Creek Blvd., Santa Clara, CA 95051.

[44] Teledyne RESON, Fabriksvangen 13, DK-3550 Slangerup, Denmark, *EC6067 - CCA 1000 Conditioning Charge Amplifier*. URL `http://www.teledyne-reson.com/wp-content/uploads/2010/12/EC6067.pdf`.

[45] K. M. Lee, K. T. Hinojosa, M. S. Wochner, T. F. Argo, P. S. Wilson, and R. S. Mercier, "Sound propagation in water containing large tethered spherical encapsulated gas bubbles with resonance frequencies in the 50 Hz to 100 Hz range," J. Acoust. Soc. Am. **130**, 3325–3332 (2011).

[46] Naval Undersea Warfare Center - Underwater Sound Reference Division, 1176 Howell Street, NUWC Division Newport, Newport, RI 02841, *Type H52 Hydrophone*. URL `http://www.navsea.navy.mil/nuwc/newport/usrdiv/transducers/H52.pdf`.

[47] Parker Hannifin Corporation - Actuator Division, Wadsworth, Ohio, *ERV Series Rodless Actuator*. URL `http://www.parkermotion.com/actuator/18942ERV.pdf`.

[48] SISU Devices, LLC, 1520 Royston Lane, Round Rock, TX 78664.

[49] Inertia Dynamics, 31 Industrial Park Road, New Hartford, CT, *Double C-Face Power-Off Brakes MPC*. URL `http://www.electromate.com/db_support/downloads/TypeMPC.pdf`.

[50] "Understanding dynamic signal analysis," Application note 1405-2, Agilent Technologies, Inc., 5301 Stevens Creek Blvd. Santa Clara, CA 95051.

[51] Tektronix, Inc., 14150 SW Karl Braun Drive, Beaverton, OR 97077.

[52] Polytec, Inc., 16400 Bake Parkway, Irvine, CA 92618.

[53] Vibco Vibrators, 75 Stilson Road, Wyoming, RI 02898.

[54] M. D. Rao and C. Van Karsen, "Mechanical vibrations," Tech. rep., Michigan Technological University (2003). URL http://www.me.mtu.edu/courses/meem3700/lecture_7.pdf.

[55] Wilcoxon Research, 20511 Seneca Meadows Pkwy, Germantown, MD 20876.

[56] Dytran Instruments, Inc., 21592 Marilla Street, Chatsworth, CA 91311.

[57] P. Avitabile, "MODAL SPACE: What is the difference between all the mode indicator functions? What do they all do?" Experimental Techniques **31**, 15–16 (2007).

[58] Applied Research Laboratories: The University of Texas at Austin 10000 Burnet Rd. Austin, TX 78758.

Vita

Richard David Lenhart was born in Phoenix, AZ and grew up in Ponca City, OK. In May of 1997, he graduated from Ponca City Senior High School, Ponca City, OK. In May 2005, he graduated with a Bachelor of Science degree in mechanical engineering from The University of Texas at Austin. He worked at the Center for Electromechanics as a mechanical engineer from 2004 until 2007. In June 2007, he took a position at Applied Research Laboratories (ARL). In August 2011 he began his graduate studies at the University of Texas at Austin in mechanical engineering while maintaining his position at ARL.

Permanent address: 1504 Devon Circle
Austin, TX 78723

This thesis was typeset by the author.